Cellulose Nanocrystals: Particle Size Distribution and Dispersion in Polymer Composites

Tianyang Leng

Supervisor: Linda J. Johnston

Thesis submitted to the

Faculty of Graduate and Postdoctoral Studies

In partial fulfillment of the requirement for the

MSc degree in Chemistry

Department of Chemistry

Faculty of Science

University of Ottawa

Abstract

This thesis describes the characterization of the particle size distribution of cellulose nanocrystals (CNC), the synthesis and characterization of fluorescent CNCs, and the development of a fluorescence microscopy method to probe the distribution of fluorescent CNCs in polymer composites.

In this thesis, several methods are used to characterize the size of CNC particles. Size distribution measurements by single particle counting methods (Transmission electron microscopy, Atomic force microscopy) are compared to an ensemble method, Dynamic lighting scattering (DLS) and differences between the various methods will be discussed. The effect of sonication on the CNC size distributions measured by AFM and DLS is examined. Furthermore, a reliable and reproducible method for re-dispersing dry CNC powder will be explored in this chapter since CNC is often stored in a dry environment due to its stability.

Rhodamine B isothiocyanate (RBITC) and 5-(4,6-dichlorotriazinyl) amino fluorescein (DTAF) were selected for labelling CNCs. These dyes have the advantage of being cheap and readily available and compatible with relatively simple synthetic chemistry. The photophysical properties of all dye labeled CNCs were studied in more detail than in previous studies. The focus is on understanding the most appropriate labeling efficiency to maximize the ability to detect individual CNCs while minimizing the amount of dye used to avoid modifying the CNC properties. The characterization methods include ensemble methods such as UV-Vis absorption and scattering measurements, fluorescence spectroscopy and single molecule methods such as Total internal reflection fluorescence microscopy (TIRFM), Atomic force microscopy (AFM) and correlated TIRFM/AFM

measurements. All of these methods have their advantages and disadvantages. After characterization, the most suitable dye labeled CNC sample was selected for development of a fluorescence microscopy method to characterize CNC distribution in CNC/polymer composites.

The dye labeled CNC has been incorporated into polyvinyl alcohol (PVA) films and studied by fluorescence microscopy. These experiments demonstrated that the level of CNC agglomeration varies significantly for different film preparation methods, indicating that fluorescence microscopy is a useful and easily accessible method for optimizing film preparation. The self-quenching of the dye in the film was also measured and discussed and is an important consideration for choice of the dye loading and CNC content in the films.

Acknowledgement

First of all, I want to thank my supervisor Dr. Linda Johnston, in the past two years, her deep understanding of the experiment, remarkable leadership, as my research has opened the way. She took me to the academic conferences, which expand my horizons and social net. In my thesis writing stage, she patiently helped me modify grammar and language, and even let me have a sense of guilt for wasted her lots of time. I'm grateful she chose two years ago in the summer. As an international student, the opportunity to work in the most beautiful and oldest building of National Research Council Canada, has been unforgivable experience in my life.

I want to thank every member in nanoscale measurement group. Zygmunt, you teach me in physics and dedicated a lot of time, sometimes, I cannot necessarily be able to fully understand. You also let me know the reason of MIT as a top university. Maohui, you guide me AFM techniques. Under your guidance, I quickly mastered the use the JPK AFM. You also made a lot of experienced and effective experiment methods for me. Also, I want to Thank Shan, Zhengfang, Dusan, Vinod, and all the summer students such as Robin, Paula. All of them did their best support for me, and make my graduate school life more colorful.

Also, I want to thank my friends in St.FX and University of Ottawa, and thank my honor project supervisor Truis Smith-Palmer.

Finally, I want to thank my dearest parents and my dearest girlfriend. With their support, I have been complete this work.

Table of Content

List of Abbreviations

AFM	Atomic Force Microscopy
APS	Ammonium persulfate
CCD	Charge coupled device
CNC	Cellulose nanocrystals
CNF	Cellulose nanofibers
CRI	Crystallinity index
CTE	Coefficients of thermal expansion
Cy3	Cyanine 3
DLS	Dynamic Lighting Scattering
DTAF	5-(4,6-dichlorotriazinyl) amino fluorescein
EM	Electron microscopes
EVA	Ethylene-vinyl acetate
FITC	Fluorescein isothiocyanate
K-S test	Kolmogorov–Smirnov test
LFM	Light field microscopy
NCC	NanoCrystalline Cellulose
NA	Numerical aperture
NIR	Near infrared
NRC	National Research Council Canada
PCL	Polycaprolactone
PEO	Polyethylene oxide

PE	Polyethylene
PLA	Polylactic acid
PVA	Polyvinyl alcohol
PVAc	Polyvinyl acetate
PP	Polypropylene
PLL	Poly-L-lysine
PVDF	Polyvinylidene fluoride
PS	Polystyrene
RBITC	Rhodamine B isothiocyanate
SANS	Small angle neutron scattering
S/N	Signal noise ratio
SEM	Scanning electron microscope
SPM	Scanning probe microscope
TEMPO	2,2,6,6-Tetramethylpiperidinyloxy
THF	Tetrahydrofuran
TGA	Thermogravimetric analysis
TEM	Transmission electron microscope
TIRFM	Total internal reflection fluorescence microscopy
TIRF	Total internal reflection fluorescence
UV-Vis	Ultraviolet and Visible
ε	Extinction coefficient
Φ	Quantum yield

τ	Lifetime
λ	Wavelength

List of Figures

fluorescence intensity curves of film set 2 4000 rpm (solid red line) and 2000 rpm (solid black line) are shown with the left y axis.

List of Tables

Chapter 1

Introduction

1.1 Cellulose Nanocrystals: A Renewable Nanomaterial

1.1.1 Cellulose

As one of the most plentiful and popular polymers in the world, cellulose is currently widely used for many industrial application such as biodegradable packaging, ropes, clothing[1], paper, food, construction and so on[2]. Wood, which is approximately 40–50 wt. % cellulose (half in monocrystalline form and half in amorphous form), is the main source of cellulose [2]. The structure of plants spans many length scales, maximizing strength while minimizing the amount of material as shown in Figure 1-1, which provides an illustration of the hierarchical structure of wood which starts with the assembly of cellulose polymer chains and fibers. Cellulose is also found in plants such as hemp, flax, Sisal, cotton and Ramie[3,4,5]. In addition, cellulose is produced by marine organisms (e.g., tunicates such as Microcosms furcates)[6] and bacteria (such as the gram-negative Acetobacter xylinum and also Gluconacetobacter xylinus) that forms a perfect network of fibers under special growth conditions[7].

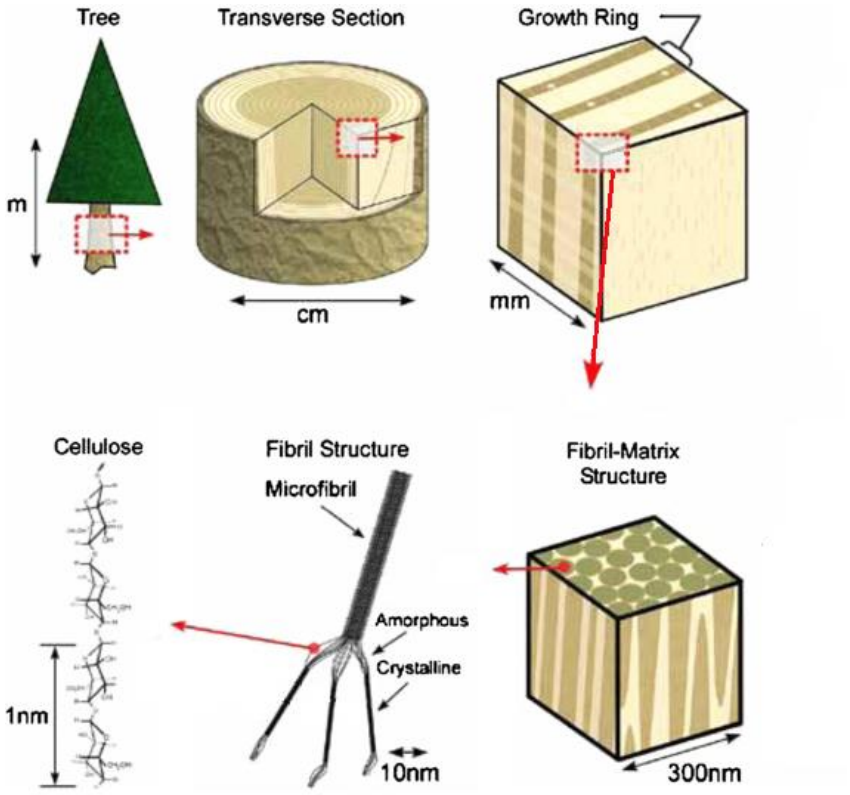

Figure 1-1: Wood hierarchical structure: from tree to cellulose. Adapted from reference [8]

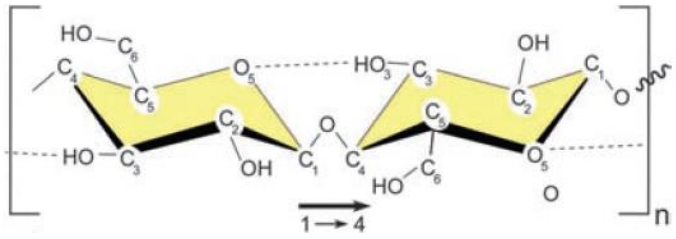

Figure1-2: Structure of cellulose polymer. Adapted from reference [9]

Cellulose is a polysaccharide composed of linear chains of glucose arranged in a flat ribbon-like conformation (Figure 1-2). Two hydroglucose rings are linked by an oxygen atom bonded to C1 of one glucose ring and C4 of the second glucose (referred to as a β 1-4 glucosidic bond). Cellulose has a molecular mass ranging from 10 000 to 15 000 for the repeat unit $(C_6H_{10}O_5)_n$ and the value of n varies with the cellulose source. The cellulose chain's linear configuration results

from the intrachain hydrogen bonding, which also stabilizes the structure. During biosynthesis, individual cellulose chains assemble by intermolecular hydrogen bonding and van de Waals interactions between the oxygen and hydroxyl group to form elementary fibrils, which then aggregate to produce larger microfibrils (the fibrils are 5 -50 nm in diameter and some microns in length)[9]. In summary, the stability and high axial stiffness of the polymer is largely due to the inter- and intra-chain hydrogen bond network, as discussed in more detail below.

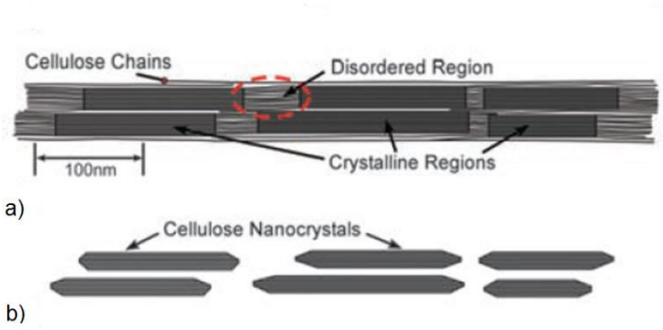

Figure 1-3: Schematic of cellulose microfiber structure (a) and the cellulose nanocrystal (b). Adapted from reference[9]

As shown in Figure 1-3 (a), two types of structures are formed in cellulose fibrils: one type is a highly ordered crystalline structure; the other is a disordered or amorphous structure, which links crystalline regions together to give larger fibrils. The cellulose nanocrystals (CNCs) shown in Figure 1-3 (b) can be extracted from the cellulose microfibrils.

Crystalline cellulose exists in several polymorphs (I, II, III, IV), which all have been extensively studied. Cellulose I, sometimes referred to as the "natural" cellulose, is produced by algae, bacteria, tunicates and trees and has thermodynamically metastable properties. Cellulose I can be transformed into either cellulose II or cellulose III; Cellulose II is the most thermodynamically stable structure of cellulose [10]. It can be formed from Cellulose I with aqueous sodium hydroxide

treatment. Cellulose III can be produced from both Cellulose I and II through liquid ammonia treatment. Then, Cellulose III can form cellulose IV by subsequent thermal treatment[9].

Cellulose I can exist as either a triclinic (Iα) or a monoclinic structure (Iβ); the proportions of the two structures vary with the cellulose source. It has been shown that the Iα structure predominates for most algae and bacteria, while tunicate and higher plant cellulose have the Iβ structure. However, both Iα and Iβ are found together in most native celluloses[10]. Of course, the Iα structure can be converted to Iβ by high temperature hydrothermal treatment (260 ℃) in alkaline solutions. The schematics of the unit cells for cellulose Iα and Iβ are shown in Figure 1-4.

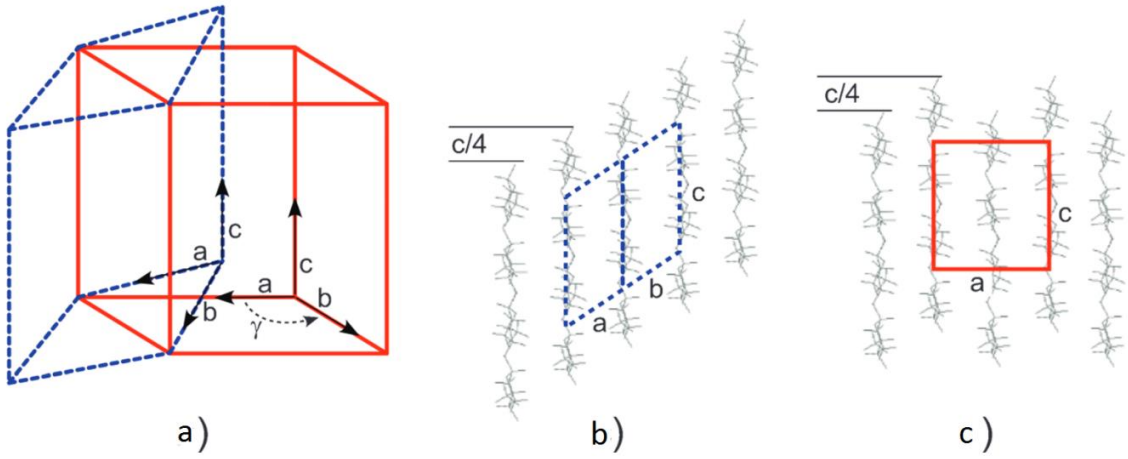

Figure 1-4: Schematic of the unit cells for cellulose Iα (triclinic, dashed line) and Iβ (monoclinic, solid line), and the displacement of the hydrogen bonding sheets for Iα of +c/4 (b), and for Iβ alternating +c/4 and c/4 (c). Adapted from reference [11]

The intra- and inter-chain hydrogen bonding is most prevalent within the (110)t and (200)m planes, and thus the name ‘‘hydrogen-bonded’’ plane. Two coexisting hydrogen bonding networks (network A and B) were described by Y. Nishiyama, et al [12], and the schematics are shown in Figure 1-5. The intramolecular hydrogen bond between the glycosidic linkage of the O (3)-H hydroxyl and the O (5) ring oxygen of the next unit, as well as the O (2)-H hydroxyl to the O (6) hydroxyl of the next residue stabilize the cellulose [13]. The planes $(100)_t$, $(110)_m$ and $(010)_t$ have substantially lower inter-chain hydrogen bonding, which results in the cohesion of the cellulose chains being controlled by the attractive van der Waals forces. It is believed that the inter-chain hydrogen bonds for Iα are weaker than for Iβ, leading to a higher stability for Iβ. Thus in the cellulose particle the strong intermolecular hydrogen bonding system leads to a high young’s modulus.

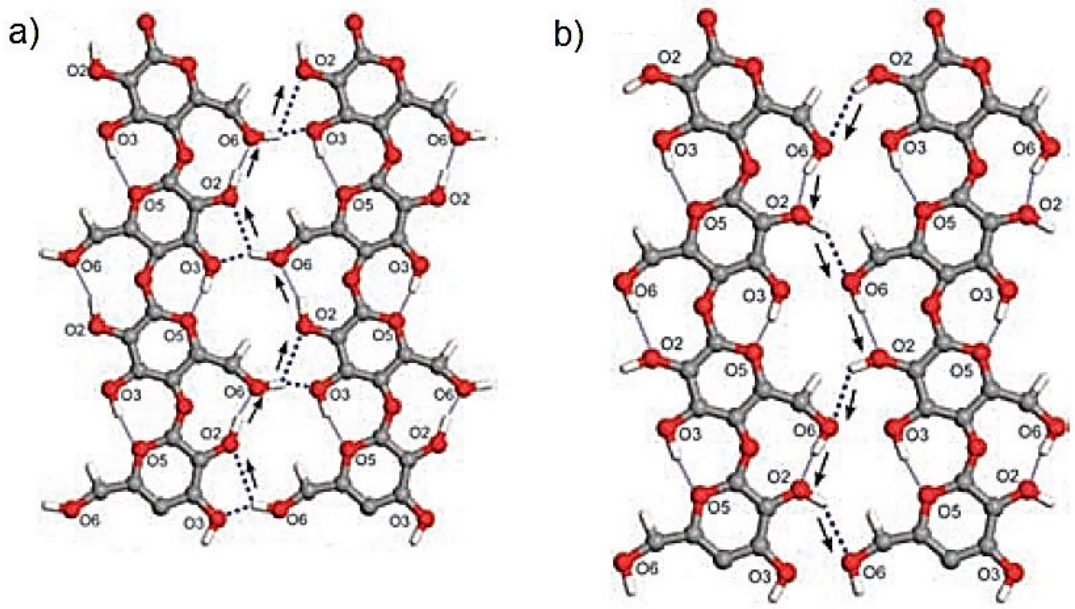

Figure 1-5: Schematics of two suggested hydrogen bonding cooperative networks A (a), and B (b), within the hydrogen-bonded planes, (110)t and (200)m. Thin dotted lines highlight the

intrachain hydrogen bonding, while the thick dotted line shows the inter-chain hydrogen bonding. Arrows show the donor-acceptor directions. Copy from reference[12].

1.1.2 Cellulose Nanomaterials

The terms used to describe cellulose nanomaterials have not been standardized and because of this there is an inconsistent use of terms in the literature to describe various cellulose particles [9]. Normally, people tend to divide cellulose nanomaterials into two types, cellulose nanocrystals (CNC) and cellulose nanofibers (CNF). These two types of cellulose nanomaterials differ from each other based on size distribution and crystalline faction. The CNF has longer length (more than 10 μm)[14], larger diameter (5-60 nm)[15] and lower crystalline fraction[16] and may contain non-cellulose components. Cellulose biomass can be treated in several ways to yield either CNC or CNF. A recent paper[16], presents the results of four different methods to prepare wood cellulose nanomaterials. The methods include enzymatic hydrolysis by endoglucanase Novozyme 476 enzyme, mechanical treatment, sulfuric acid hydrolysis, and TEMPO (2,2,6,6-Tetramethylpiperidinyloxy) mediated oxidation[17]. It is evident from this study that the method of preparation can alter the size, shape, crystalline faction, and surface chemistry of the cellulose nanomaterial, even when using the same starting material (Table 1-1 and Figure 1-6). As shown in Figure 1-6, the CNC produced by acid hydrolysis is much smaller than the CNF produced by any of the other 3 methods, because the larger CNF retains disordered cellulose regions that link the small cellulose nanocrystals.

Table 1-1: Different preparation methods lead to different particle types with varying crystalline fractions and different surface functional groups. Adapted from reference [16]

Cellulose source/method	Particle type	Crystalline Faction	Surface Chemistry
Wood-enzymatic	CNF	0.30	Hydroxyl (neutral)
Wood-mechanically refined	CNF	0.55	Hydroxyl (neutral)
Wood-Sulfuric acid hydrolysis	CNC	0.60	Sulfate /Hydroxyl (negative)
Wood-TEMPO mediated oxidation	CNF	0.05	Carboxylate /Hydroxyl (negative)

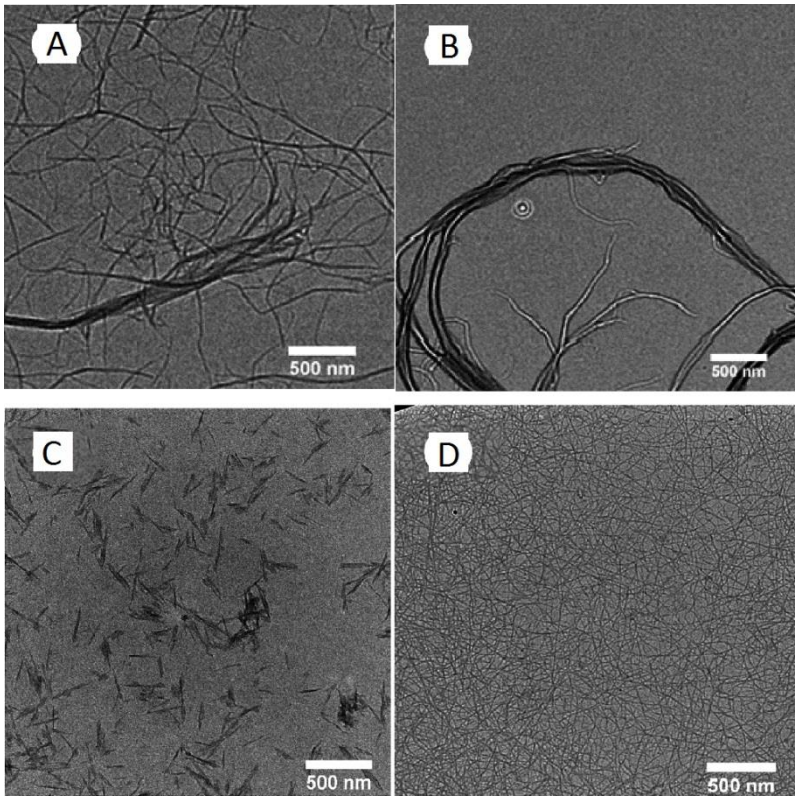

Figure1-6: TEM images of cellulose nanomaterials: (a) CNF from enzyme treatment, (b) CNF from mechanical refining, (c) CNC from sulfuric acid hydrolysis, and (d) CNF from TEMPO oxidation. Adapted from reference [16].

1.1.3 Cellulose Nanocrystals (CNC)

These nanoparticles are generally called cellulose nanocrystals (CNC) although their nomenclature in the literature is ill-defined and they have also been called "cellulose nanowhiskers"[18] and "NanoCrystalline Cellulose (NCC)"[19].

There are several ways to prepare the CNC with acid hydrolysis using sulfuric acid being the most commonly used method. The treatment of cellulosic microfibers by acid hydrolysis results in the dissolution of their amorphous domains. The glyosidic bonds of the cellulose chains are cut longitudinally to form the microfibers and rod-like near perfect cellulose nanocrystals [2]. Hydrolysis using sulfuric acid grafts sulfate groups onto the surface hydroxyl groups through esterification. The presence of these negatively charged groups promotes the dispersion of CNC in water by increasing unfavorable electrostatic repulsions and leads to stable colloidal suspensions. Hydrolysis with hydrochloric acid gives only hydroxyl groups on the surface, leading to neutral CNCs that aggregate and are difficult to disperse. Phosphoric acid [20], hypochlorite acid, Ammonium persulfate (APS) oxidation[21] and nitric acids [3] have also been employed for the preparation of CNC with different surface groups. All methods except for hydrochloric acid hydrolysis give mixtures of surface functional groups. Some of the original hydroxyl groups always remain on the CNC surface[21]. Some examples of CNC surface chemistry using different preparation methods are shown in Figure 1-7.

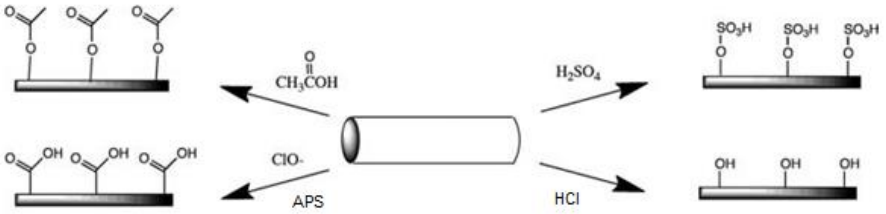

Figure 1-7: CNC surface chemistries by different methods: sulfuric acid hydrolysis provides sulfate esters (top right), hydrochloric acid hydrolysis provides hydroxyl (bottom right), acetic acid hydrolysis gives acetyl (top left), and Ammonium persulfate (APS) oxidation or hypochlorite hydrolysis provides carboxylic acid (bottom left). Adapted from reference [9].

For CNC produced by sulfuric acid hydrolysis with 63.5 wt. % acid for approximately 2 h, the length of CNC is typically between 100 and 400 nm, its width is less than 10 nm and its yield is 30% based on initial weight of the cellulose source [22]. The effects of varying the acid-to-pulp ratio and reaction time on the nanocrystals produced by sulfuric acid hydrolysis of bleached softwood pulp was studied by Beck-Candanedo et al [22]. Shorter nanoparticles with a narrow polydispersity were generated when longer hydrolysis times were used. A method to control the size distribution has been discussed by Elazzouzi-Hafraoui et al [23]. Results in that paper shows that acid hydrolysis of cotton in 65% sulfuric acid for about 30 min at temperatures of 45 to 72 ℃ can produce CNCs with different size distributions. Shorter crystals were obtained when the temperature increased, although it's still unclear whether temperature influences the width of the crystal.

When the method of CNC preparation is kept constant, the size, yield and crystallinity index of the nanoparticles are determined by the cellulose source. Leung et al [21], measured size, yield and

crystallinity index (CRI) for CNCs obtained from various cellulose sources (Table 1-2) by APS oxidation. In this study, solid-state NMR, X-ray diffraction and IR spectroscopy were used to characterize the CNCs. The average crystallite sizes were determined by the Debye–Scherer formula.[21] The TEM images (Figure 1-8) show CNC from different biomasses which have different shapes.

Table 1-2: The yield, crystallinity index (CRI), and dimensions of CNCs produced from various cellulosic sources. X-ray diffraction with the integral method for assessing the contributions from amorphous and crystalline cellulose was used for CRI estimation. Adapted from reference[21].

CNC Source	Yield (%)	CNC CRI (%)	Length (nm)	Diameter (nm)
Flax	28	75	144±5	3.8±0.1
Flax shives	22	64	296±16	5.1±0.1
Hemp	36	73	148±3	5.8±0.1
Tunicate	31	73	1160±5	4.2±0.1
Whatman™ paper	81	91	121±3	6.7±0.3
Wood pulp	36	81	124±6	6.0±0.2
Bacterial	14	70	88±5	6.5±0.2

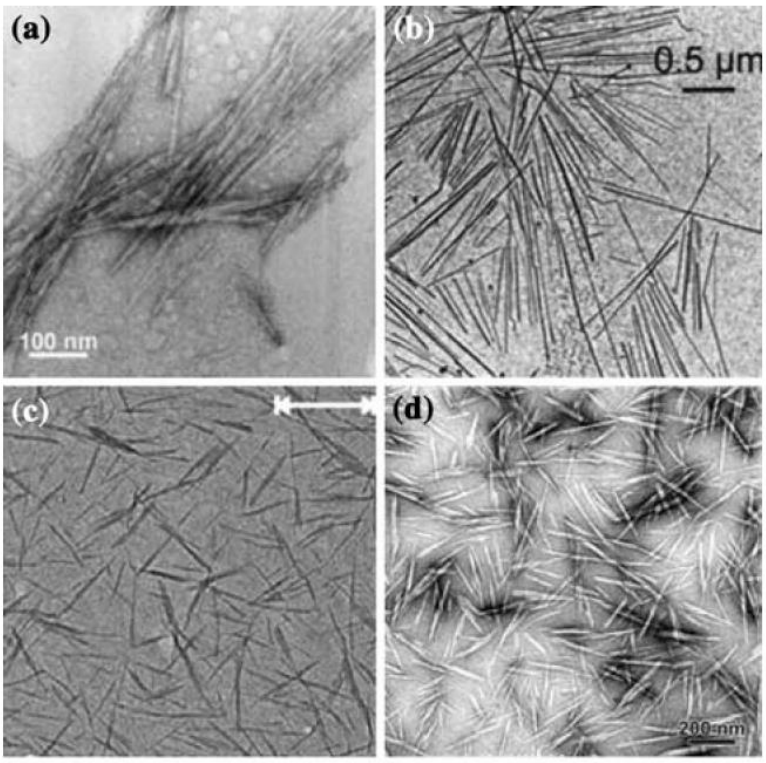

Figure 1-8: Transmission electron microscopy images of cellulose nanocrystals, obtained from acid hydrolysis of wood cellulose (a), tunicate (b), cotton (c), ramie (d). Adapted from reference [7]

1.1.4 CNC properties

CNC has been a focus in nanomaterial research because it is a renewable biomaterial, which has low toxicity, high aspect ratio, and low density (1.6 g cm^{-3}), and forms stable colloidal suspensions. CNC also has a large surface area with reactive functional groups, allowing different species to be grafted onto its surface. Surface functionalization diversifies particle surface chemistry and can facilitate self-assembly, thereby controlling dispersion within a wide range of polymer matrices. Some CNC composites produced are transparent, have tensile

strengths greater than cast iron, and have very low coefficients of thermal expansion (CTE). Potential applications include, but are not limited to, food, paints, thin film, paper, rheology modifiers and drug delivery systems.

The mechanical properties of CNC are important for development of composites. CNC has a high modulus which was first predicted in 1936 using a theoretical model based on spectroscopic measurements by Meyer and Lotmar [7]. Their calculated value was 120 GPa; however, different modulus values have been reported. The measured CNC moduli range from 80- 200 GPa[7]. For comparison, Table 1-3 presents the moduli of some commonly used materials in engineering. Based on its properties, CNC is a great nano material for increasing the mechanical strength of polymer composites. For example, Shanhong et al[24], used CNC to reinforce waterborne epoxy. A linear relationship between CNC concentration and modulus was observed, as shown in Figure 1-9, which suggests strong adhesion between epoxy and CNC surfaces.

Table 1-3: The comparison of cellulose moduli with moduli for other engineering materials. Adapted from reference [9]

Material	Density ($Mg\ m^{-3}$)	Modulus (GPa)	Specific Modulus ($GPa\ Mg^{-1}\ m^{-3}$)
Kevlar-49	1.4	69	26
Carbon fiber	1.8	200	26
Carbon nanotube	2.2[25]	69	28
CNC	1.6	138	92

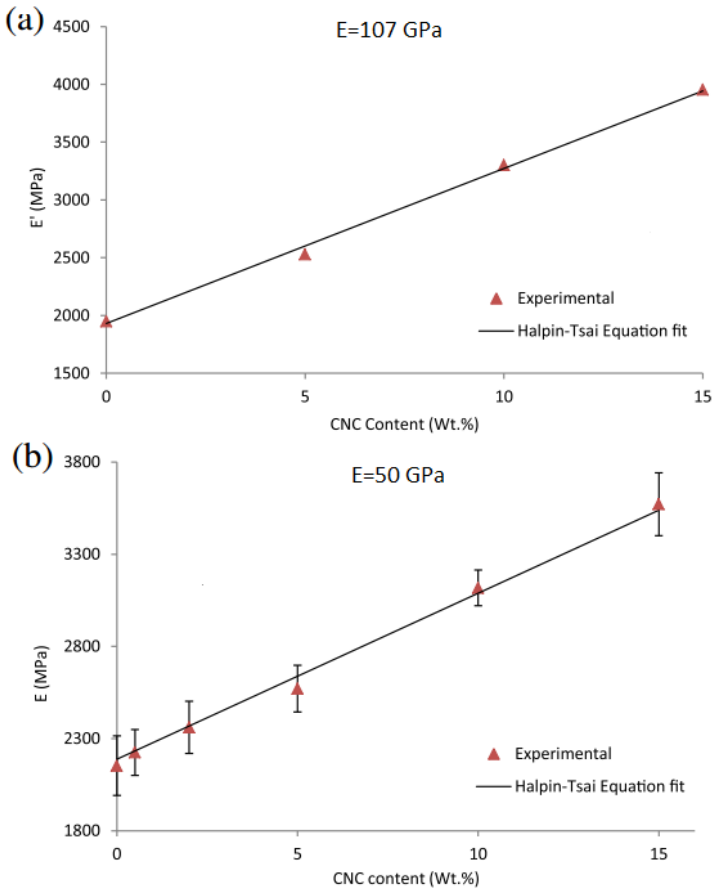

Figure 1-9: Experimental data (symbols) and linear fit (line) of (a) storage modulus at 30 °C and (b) Young's modulus as a function of CNC content in a waterborne epoxy composite. Adapted from reference[24].

Due to CNC's nano-rod shape and small diameter, it possesses a large surface area (400 m^2/g) compared to other high surface area materials such as carbon black (150 m^2/g). The relationship between diameter and surface area of nano-rods is presented in Figure 1-10 [26].

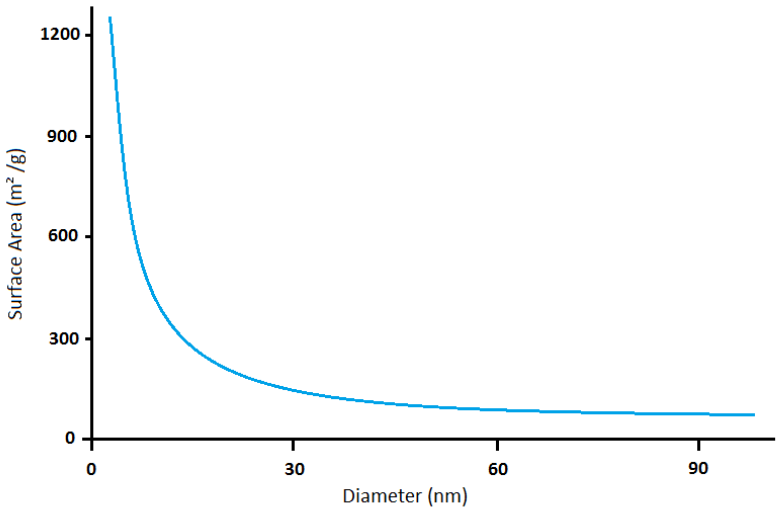

Figure 1-10: The relationship between the surface area and diameter of CNC nano-rods, assuming a CNC density of 1.5g cm^{-3}, adapted from [26].

The homogeneous dispersion of CNC in the polymer composite is crucial to achieving improved mechanical properties. Researchers have attempted to produce homogeneous dispersions by manipulating the CNC surface chemistry. Depending on the treatment of raw material, the CNC surface can contain different functional groups, as introduced in Chapter 1.1.3. The most popular method is treating cellulose with sulfuric acid to form a sulfated surface. Another popular method is hydrolysis by treatment with hydrochloric acid. This method yields hydroxylated surfaces, but the low surface charge impedes CNC dispersion in water relative to the charged sulfated CNCs. In addition to water, other polar solvents, hydrophilic polymers or polar solvent-soluble polymers can be used for creating CNC suspensions. For apolar or low polarity solvents or polymers, the CNC surface must be modified to improve its dispersion. Luckily, the high surface area of CNC allows for extensive surface modification due to solvent-exposed functional groups.

Table 1-4 shows that the dispersion of CNC in various polymer resins can be increased by surface modifications using different grafting agents (e.g. hydrophilic or hydrophobic molecules) to improve the polymer's mechanical properties. Although the surface modification possibilities are extensive, it is important for the coupling reaction to be mild such that it changes only the surface functional groups and does not modify other properties of the nanoparticle. In addition, the functional group added by surface modification must be stable in the solvent used and hard to remove from surface.

Table 1-4: Common surface modifications of CNC and their objective. Adapted from reference [27].

Grafting Agent	Objective
Acetic anhydride and acetic acid	Ultrastructural aspect of acetylation
Iso-octadecenyl succinic anhydride and *n*-tetradecenyl succinic anhydride	Dispersed in solvents under the low polarity
Acetic anhydride	Redispersed in water
Organic acid chloride aliphatic chain	Dispersion in PE
Palmitoyl acid	Hydrophobization
Acetic and butyric acids	Dispersed in ethyl acetate and toluene
Vinyl acetate	Dispersed in THF
Acetic anhydride	Dispersed in chloroform
Succinic anhydride	Adsorption of heavy metal ions
Alkenyl succinic anhydride	Dispersed in PP and PLA
Hexamethyldisilazane	Dispersed in acetone and acetate butyrate
Isopropyl, *n*-butyl, *n*-octyl, and *n*-dodecyldimethylchlorosilane	Dispersed in THF
***n*-dodecyldimethyl-chlorosilane**	Dispersion in THF and chloroform, compatibilization with PLA
Isocyanate propyl triethoxysilane	Hydrophobization
***n*-Octadecylisocyanate**	Dispersed in PCL

In the literature [28], the coefficient of thermal expansion (CTE) and thermal chemical degradation are used to describe the thermal stability of CNC. Normally, thermogravimetric analysis (TGA)

is used to measure the loss of mass under a certain heating rate. For various freeze dried cellulose nanomaterials, the TGA measurements show the onset of thermal chemical degradation to be near 300 ℃ for CNF and near 260 ℃ for CNC. Furthermore, chemical modifications to CNC were shown to alter the onset temperature for degradation. It has been estimated that the crystalline cellulose CTE is near 0.1 ppm K^{-1} in its axial direction, which is about an order of magnitude lower than most ceramics and metals (iron is 11 ppm K^{-1}) [28]. However, this value is similar to other anisotropic fibers such as carbon fibers.

Several studies have investigated the optical properties of CNC-reinforced and modified CNC-reinforced polymers. A schematic plot of transmittance as a function of wavelength illustrates several factors which influence the optical transmittance of films (Figure 1-11). The CNC-based nanocomposite films' optical properties can be measured in a UV–visible spectrophotometer through light transmittance. The wavelength range of 200–1000 nm is used in the measurement. Using the optical properties of CNC composites, the distribution of CNC in the composite, the CNC particle size, and film thickness can be determined [16]. Also because CNC do not usually increase the composite transmittance, they could be very useful for producing transparent nanocomposites.

Usually, in order to avoid the intensity loss from Rayleigh scattering, the nanoparticle diameter is restricted to the upper limit of 40 nm. Considering the refractive index mismatch between cellulose (1.58)[27], and most host matrices (most polymer is near 1.5), the transparency of CNC-based nanocomposites is largely dependent on the width of the nanocrystal, since scattering depends on its effective cross sectional area in the host polymer matrix. Therefore, good CNC dispersion can be indicated by high transmittance values within the nanocomposite film [27].

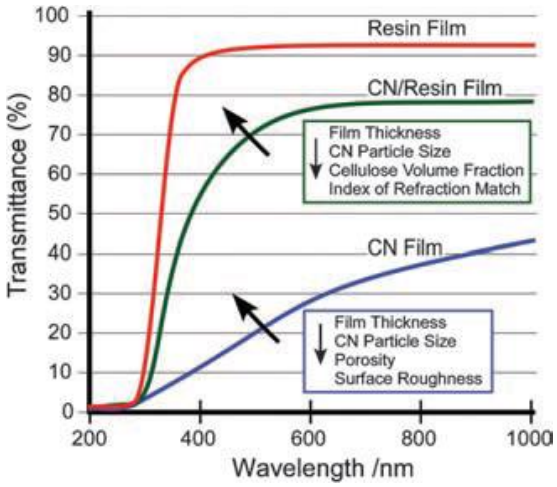

Figure 1-11: Schematic plot showing light transmittance as a function of wavelength for neat polymer and cellulose films and the CNC-polymer composite film. Adapted from reference [9]

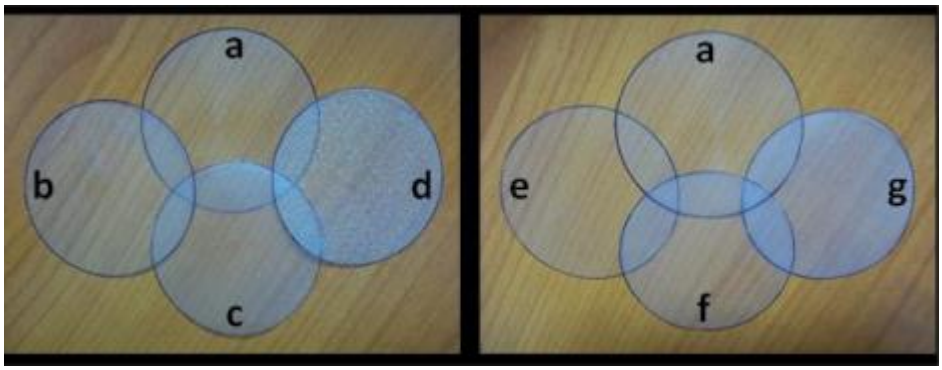

Figure 1-12: Photographs of PLA films and nanocomposites reinforced with (a) 0, (b) 2.5, (c) 7.5, and (d) 15 wt. % unmodified or (e) 2.5, (f) 7.5, and (g) 15 wt. % chemically modified cellulose nanocrystals. Adapted from reference [29]

For example, casting/evaporating mixtures of cellulose nanocrystals and PLA has been studied as illustrated by the photographs of nanocomposite films, shown in Figure 1-12. Both n-octadecylisocyanate-grafted cellulose and unmodified nanocrystals were used as the reinforcing

phase. Visual examination of the films demonstrated that the lowest CNC content (2.5 wt. %) is well-dispersed in the film since its transparency is comparable to that of the pure polymeric matrix. The films reinforced with chemically modified CNC are shown in (Figure1- 12 (a) and Figure 1-12 (b)). A granular structure can be observed from aggregates of the unmodified nanoparticles at higher filler loading in the matrix; however, no aggregates were observed for the modified CNC and the films tended to be opaque [29].

1.2 Introduction to Techniques Used

1.2.1 Atomic Force Microscope (AFM)

The atomic force microscope (AFM) is an important imaging tool in CNC research. It can provide us with CNC images with good contrast and relatively low cost. AFM is a type of scanning probe microscopy (SPM) that is able to measure surface topography, mechanical properties and specific probe-sample interaction, all on the nanometer scale. AFM can be compared to scanning tunneling microscopy (STM) which uses tunneling current between a sharp metal tip and a conductive or semi-conductive surface when a voltage is applied between these two to measure the surface[30]. The atomic force microscope (AFM) measures interaction forces between the sample and a tip attached to a flexible cantilever as the tip is raster scanned across the surface.

The AFM probe consists of a very sharp tip with a typical width of 10 nm which is attached to a cantilever possessing a well-defined spring constant. A laser beam aimed at the back of the cantilever will be reflected and detected by a position-sensitive photodiode detector. As the tip scans over the sample surface, interactions with sample features alter the cantilever deflection.

This information then feeds back to the piezo which adjusts the height of the tip to maintain a constant tip-sample force. As the probe scans the region of interest, these electronic signals are converted into line scans which are compiled into entire images by appropriate image processing software.

As in most SPM, the AFM tip is driven by a piezoelectric scanner. The piezo scanner is made from perovskite crystals consisting of a small tetravalent metal ion, usually titanium or zirconium [31]. This allows the piezo material to be subjected to mechanical stress under an electric potential. The piezo expands and contracts in proportion to an applied voltage (Figure 1-13). As such, the piezo was crucial to the development of AFM since it offers picometer scale control of tip movement by adjusting current. Normally, there are two piezo control systems used in AFM; one for X-Y direction scanning and another for Z direction scanning.

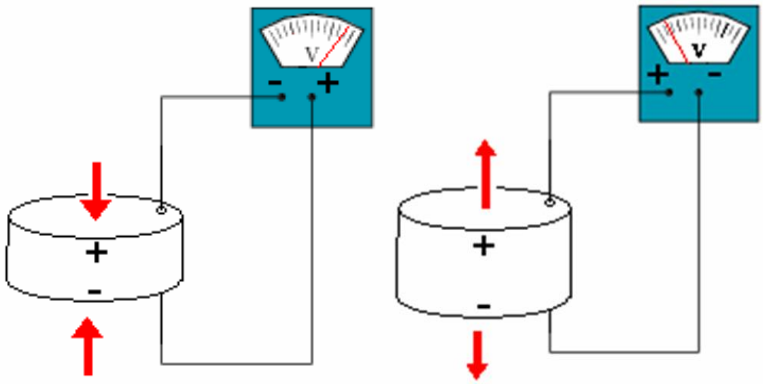

Figure 1-13: Piezo Compression (Left): Decrease in volume in response to a positive applied voltage. Piezo Tension (Right): Increase in in response to a negative voltage. Adapted from Reference [32].

The feedback system used in AFM is laser beam deflection (Figure 1-14). A simple photodiode is used as the photodetector, which produces current upon absorption of photons. The photodiode

is split into four sections for detecting both lateral and vertical deflections of the tip. By comparing the relative intensity of the laser beam in each section of the detector, an approximate quantification of tip displacement can be calculated[33]. The magnitude of displacement is determined by the size of the cantilever; the smaller the cantilever the greater the angular displacement. However, the level of angular displacement is independent of the distance between the cantilever and detector. This is because increasing the distance between cantilever and detector decreases the intensity, lowers the S/N ratio and increases the dispersion of the laser[33]. Using this laser beam deflection system, the smallest theoretical measurable cantilever displacement is approximately 4 x 10^{-5} nm , when the S/N ratio is near 1[33].

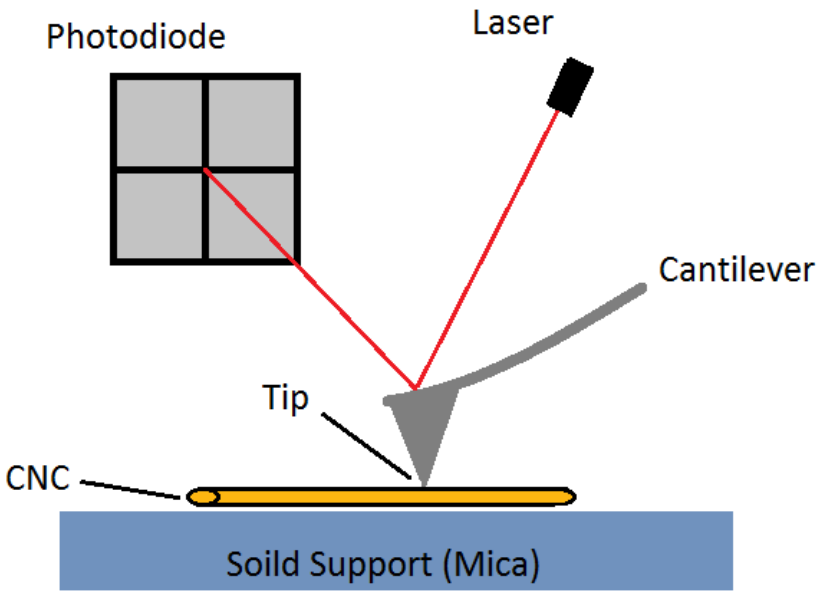

Figure 1-14: Schematic depiction of AFM performed on a CNC absorbed on a mica surface.

As the name "atomic force microscope" suggests, there are several types of forces acting between tip and sample. The most common is the van der Waals force which is present in all

materials. It is possible to characterize both the attractive and repulsive parts of the force-distance relationship between tip and sample. If a particle at the surface of the sample interacts with a particle at the end of the tip, the potential energy can be described as a pair-potential energy function. This function is well-known as the "Mie" pair-potential energy function, or the Leonard-Jones Potential function , Equation 1-1[34]:

$$V^{pair}(r) = 4\varepsilon[(\frac{\sigma}{r})^{12} - (\frac{\sigma}{r})^{6}] \qquad \text{(Equation 1-1)}$$

In Equation 1-1, the terms ε and σ are constants which depend on the material and r is the distance of separation between the two particles. The first part of the equation, $(\sigma/r)^{12}$ describes the repulsive forces between particles while the latter part, $(\sigma/r)^{6}$ denotes attraction. At the equilibrium value for r, V is at its minimum value. The schematic diagram is shown in Figure 1-15.

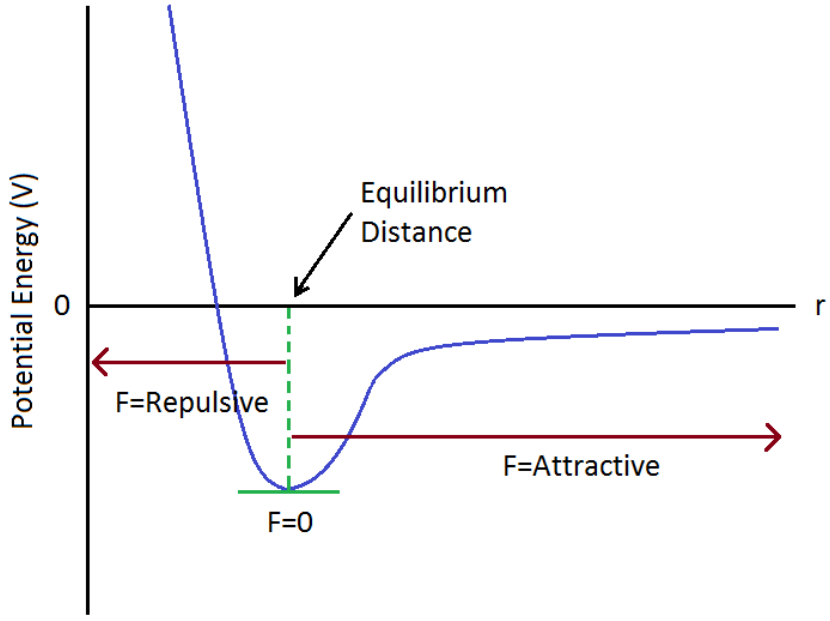

Figure 1-15: Description of both the attraction and repulsion between non-ionic particles using the Lennard-Jones function. Adapted from reference [35].

The pair-potential energy theory can be applied to provide an understanding of the cantilever force-distance curve, as shown in Figure 1-16[34]. When the distance between tip and sample is large, the attractive force is too small to affect the tip. In this position (position 1 in Figure 1-16), there is no apparent deflection. Then, as the tip approaches the sample, attractive van der Waals forces dominate and the cantilever bends towards the sample (position 2 in Figure 1-16). The van der Waals force increases quickly with distance, while the cantilever spring constant is constant. Once the attractive force is larger than the resistance of the cantilever, the tip jumps to contact the surface, as shown by position 3 in Figure 1-16. As the tip is pushed closer, the cantilever deflection has a linear relationship with piezo movement distance (position 6 in Figure 1-16). At the equilibrium position (position 5 in Figure 1-16) the cantilever is approximately straight and the force between the sample and tip is zero. This is the ideal condition for contact mode scanning. As the tip is pushed closer, past the equilibrium position, repulsive van Der Waals forces cause the cantilever to bend away from the sample (position 6 in Figure 1-16).

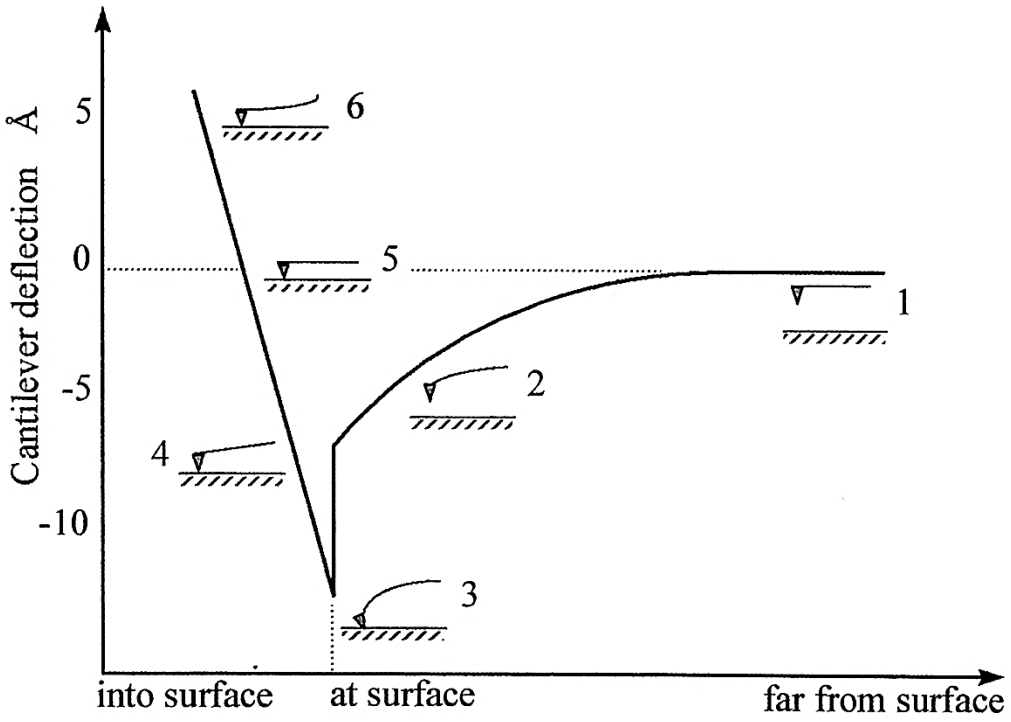

Figure 1-16: Idealized Cantilever deflection against piezo traveling distance. Adapted from reference [33]

In addition to van der Waals forces, there are also electrostatic forces, capillary forces, adhesive forces and double layer forces between the tip and sample. Electrostatic force is the force between charged particles. These charges can be deposited either by contact electrification, or by corona discharge (CD)[30]. At small separation distances, the force can be calculated by the Coulomb force law where ε_0 is the permittivity of free space (Equation 1-2)[34],

$$F = \frac{q_1 q_2}{4\pi\varepsilon_0 r^2} \qquad \text{(Equation 1-2)}$$

As the ions are brought close together the attractive electrostatic force between them increases sharply. The electrostatic force has been used for characterization in a variety of experiments where surface charges are involved[30].

As a consequence of air humidity, there is a layer of water on top of the sample surface. When imaging by AFM, this liquid meniscus pulls down the tip resulting in capillary force. This is not an easily controlled parameter and thus is a major drawback to AFM in ambient conditions. Although, the use of dry (low humidity) air could reduce this effect, it is not convenient for some experiments. Furthermore, the AFM tip 'ages' as it scans. The tip may become blunted or contaminated with small samples; both of them can lead to 'adhesive force', complicating the study of small objects. When adhesion forces appear, the only solution is to replace the tip. Very high patience is required to deal with this problem.

Double layer force is exclusive to imaging in aqueous media. Because mica is negatively charged, the charged surface can attract counter ions from solution. The result is a positively charged layer at the solid-liquid interface which may electrostatically repel the tip. Usually, the greater the ionic strength of the imaging medium, the lower the electrostatic repulsion is. Therefore, usually a small amount of salt (several mM) is added to the scanning media solution to circumvent this problem.

Contact mode, non-contact mode and intermittent contact (tapping) mode are three basic imaging modes commonly applied in AFM. The most basic is contact mode which scans the sample with a constant approach force. Normally, position 5 in Figure 1-16 is the ideal position for contact mode. The piezo adjusts the tip using the laser beam feedback system to keep the force constant. For example, the tip is moved up and down in order to keep the signal from the detector constant

as it scans across uneven surfaces. This mode is suitable for hard, stable and dry samples since delicate samples can be damaged or removed from the imaging surface by the tip.

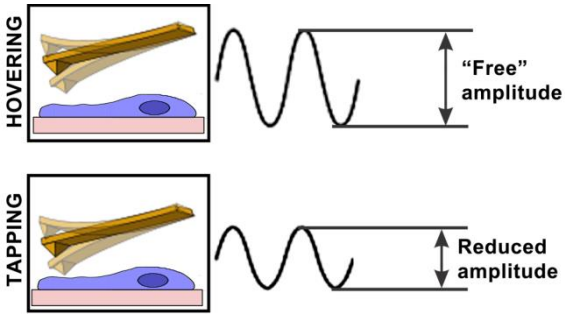

Figure 1-17: Schematic diagram of tapping mode free amplitude (upper) and reduced (approached) amplitude. Adapted from (V. J. Morris, 1999a)

Intermittent contact or tapping mode operates by oscillating the cantilever, where the tip is close enough to tap the sample at bottom of each oscillation. Contact with the sample has the effect of lowering the cantilever's resonance amplitude (as shown in Figure 1-17) which is detected by the photodetector and processed by the imaging software. The tip's lateral position is controlled by the piezo. Thus, the height of the sample surface is detected by the change to the resonance amplitude. In this mode, large oscillation amplitude makes the approach less sensitive to the environment which reduces noise and increases resolution. Moreover, the reduced tip contact can prevent damage and movement of the sample.

The non-contact mode also operates through an oscillating cantilever. In this mode the cantilever is made to oscillate at its resonance frequency. The cantilever is moved close enough to the sample surface for the tip to experience Van-der-Waals and other molecular interactions. These interactions will change its vibration as it scans across the sample. Therefore, position 2 in Figure 1-16 is the ideal position for non-contact mode. This mode is very sensitive to

environmental factors, such as humidity, so low force measurements are prone to noise and poor resolution.

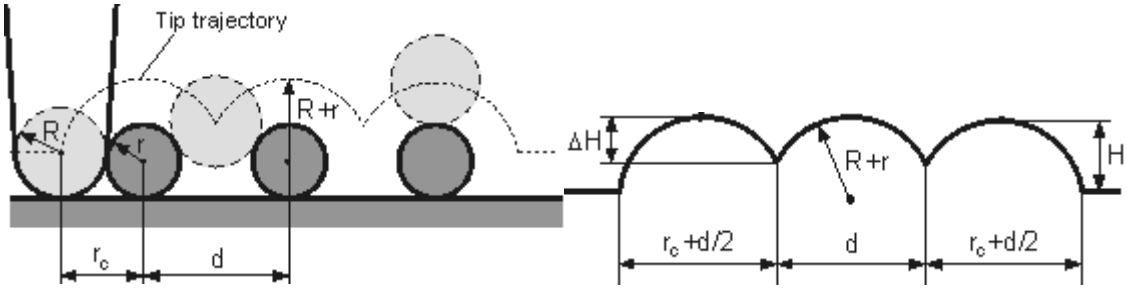

Figure 1-18: The left picture shows a schematic of a spherical object (radius=r) imaged by a conical tip (radius=R) where R≈r. The right picture shows a line scan corresponding to the left picture. Adapted from reference[36]

For small samples (normally less than 100 nm), the tip radius of curvature (also called tip convolution effect) must be considered. The acquired topography image can be distorted by effects of the instrument on the object, resulting in the appearance of artifacts.[36] For the experiments presented here, the tip's typical radius is 8 nm, and the CNC's typical radius is near 2 nm. Since the tip is larger than the sample, the tip convolution effect can be estimated according to the model shown in Figure 1-18[36]. Additionally, the wear of the tip contributes to the error of the CNC width measurement. Thus, only the CNC length and height can accurately be measured.

1.2.2 Dynamic Lighting Scattering (DLS)

Dynamic Lighting Scattering (DLS) is widely used for size measurement of nanoparticles. This is mainly because it is relatively cheap and convenient to use to measure size distributions.[37].

DLS does not measure the particle size directly as does AFM or any other type of microscopy. It measures the Brownian motion of nanoparticles in suspension by measuring the intensity fluctuation of light scattered from particles and relates this to the diffusion coefficient and size of particles. The detector in DLS is set at a fixed angle of incident light (normally 90 °or 173 °). When the incident laser illuminates the sample suspension, a classical speckle pattern of emitted light would be seen [38]. The speckle pattern is determined by both speckle size and position in the homogenous suspension system. The dark patches are due to scattered light which have the reverse phase interfering with each other, and lowering the overall intensity (figure 3A). The bright patches in the speckle pattern are due to light scattered from the particles which has the same phase and interfere constructively to increase the intensity. The DLS working schematic diagram is shown in Figure 1-19.

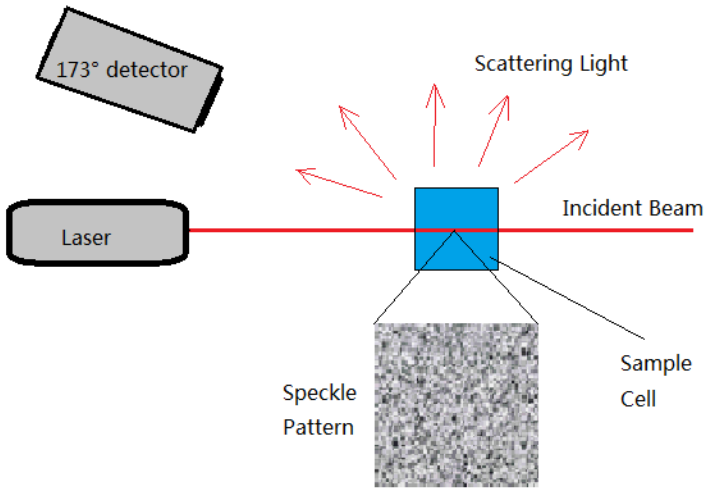

Figure 1-19: Schematic of DLS system and speckle pattern shows in imagery screen. Adapted from reference[38].

When the particles undergo Brownian motion, a speckle pattern is observed with a constant motion because of the phase addition from the moving particles[38]. The fixed detector records the total intensity fluctuation which depends on the size of the particles. The fluctuation intensity changes slowly with a large gap for a dispersion of large particles. It changes rapidly with a small gap for a dispersion of small particles. The typical intensity fluctuation curves for large and small particles are shown in Figure 1-20 right. A digital auto correlator is used for analysis of the intensity fluctuations. This correlator is a basic signal comparator which is designed to distinguish between two similar signals based on the time dependent fluctuation. Figure 1-20 left shows a simple example of how the correlator works. In this Figure, for randomly fluctuating signals, if you measure the initial intensity and the intensity at a much later time there is no correlation. However, if the signal at time t is compared to the intensity at a very small time later ($t+\delta t$) there will be a strong correlation between the two signal intensities. Because the signal comes from Brownian motion, at $t+2\,\delta t$, the signal still has correlation with signal at t, but it is not as high as the comparison between t and $t+\delta t$. Thus, the correlation is reducing with time[38]. If the time goes to infinity, the correlation is zero. For larger particles, the correlation reduces slowly and for the smaller particles, the correlation reduces quickly.

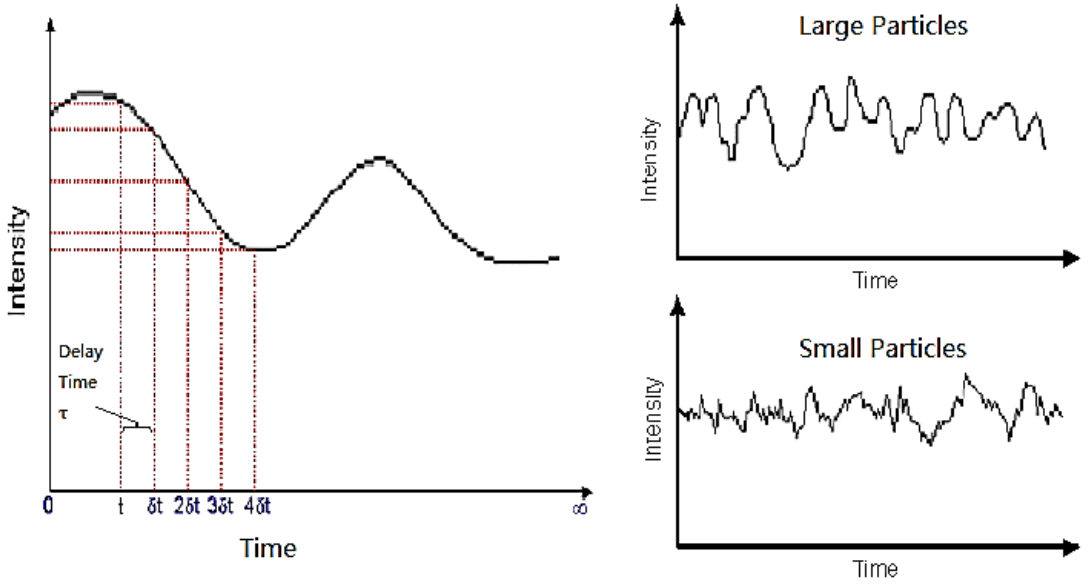

Figure 1-20: A simple example illustrating how a correlator works (Left) and the typical intensity fluctuation curves for large and small particles (Right). Adapted from reference [38]

For DLS, the time correlation function has been used to quantify the signal correlation. The first order correlation function could be written by Laplace transform of the distribution function, G(Γ) .[39 40]

$$g^{(1)}(\tau) = \int_0^\infty G(\Gamma) e^{-\Gamma\tau} d\Gamma \qquad \text{(Equation 1-3)}$$

Because $\Gamma = Dq^2$, where D is the translational diffusion coefficient and q is defined as :

$$q = \left(\frac{4\pi n}{\lambda}\right) \sin\left(\frac{\theta}{2}\right) \qquad \text{(Equation 1-4)}$$

where n is refractive index of dispersant, λ is laser wavelength, and θ is scattering angle. Then, the final correlation function [G (τ)] could be written as:

$$G(\tau) = A[1 + B\, g^{(1)}(\tau)^2] \qquad \text{(Equation 1-5)}$$

Size could be obtained from the correlation function by cumulants analysis which fits the data to a single exponential to obtain the translational diffusion coefficient, D. The size of the particle is then calculated from the Stokes-Einstein equation[41] (Equation 1-6)

$$d = \frac{kT}{3\pi\eta D} \qquad \text{(Equation 1-6)}$$

This approach gives the equivalent hydrodynamic diameter of the particle which is an intensity weighted average value known as the Z-average[42]. The Z-average does not measure size directly for non-spherical particles (such as CNC rods) since it measures the equivalent hydrodynamic diameter, which is the diameter of a sphere that diffuses at the same rate. The polydispersity, PdI, is also obtained from the correlation function and describes the width of the particle size distribution. Normally, PdI values smaller than 0.05 are rarely seen other than with highly monodisperse standards; PdI values greater than 0.7 mean that the sample has a very broad size distribution and is probably not suitable for the dynamic light scattering (DLS) technique[43]. It is important to keep in mind the DLS Z-average is frequently different from the particle diameter measured for a dry sample by microscopy, since DLS measures hydrated particles in a liquid. Microscopy size data are also typically expressed as a number average, which is different from an intensity average. Since the scattering intensity is proportional to d^6 (Rayleigh approximation), scattering from large particles contributes more to the intensity distribution. Intensity distributions can be converted to volume or number distributions for spherical particles, although this approach introduces substantial error.

1.2.3 Transmission Electron Microscopy (TEM)

Two types of electron microscopes (EM) are used to study nanoparticles, transmission electron microscope (TEM) and scanning electron microscope (SEM). If the particle size is small (≤ 5 nm), the SEM cannot provide enough resolution to measure the size of single particles. TEM is typically used to measure CNC size distribution [44] The SEM is used to study larger particles or aggregated nanoparticles.

EM is the microscope work with electron instead of light for optical microscope. Furthermore, compared with optical microscope, the magnetic electric lens and electron source are instead of the optical lens and light source. TEM is a direct imaging technique that use the focused electron beam (100–300k eV)[45] to image samples based on electron scattering and absorption contribution to loss of transmitted electrons. The image contrast is determined primarily by electron density and the electron scattering difference between different atomic number materials[45]. TEM could achieve higher resolution than the optical microscope because the electron has shorter wavelength than visible light. From the de Broglie equation[46], we can approximate the electron wavelength as below, where the E is electron energy in electron volts (eV):

$$\lambda \approx 1.22/\sqrt{E} \qquad \text{(Equation 1-7)}$$

From this approximation, a 100 keV electron has wavelength of 0.004 nm, much shorter than visible light wavelengths (400-800 nm). The resolution for an optical microscope can be approximated as:

$$d = \frac{0.61\lambda}{\mu \sin \beta} \qquad \text{(Equation 1-8)}$$

In this equation, μ is the refractive index and β is semi-angle of collection of magnifying lens. From this equation, the limited resolution would achieve near 200 nm. For the TEM, μ is not a factor and the electron wavelength λ is much smaller. The theoretical resolution d can easily reach 100 pm (0.1 nm). Of course, there are many limitations of TEM, the primary limitation being sample preparation. The contrast of TEM images comes from the different electron transmission between the sample and support (e.g. carbon grid). For samples like CNC, which is composed of carbon and hydrogen, the transmission of the electron beam is high which can lead to very low contrast in the TEM images. Thus, heavy metal solutions such as uranyl acetate are used to stain the CNC. There are other problems in TEM such as sample charge, electron beam damage, and even difficulties in interpreting images.[46]

1.2.4 Fluorescence Techniques

Fluorescence microscopy and spectroscopy are among the most widely used tools in chemical and biological science. Finding a fast, low cost and accurate way to determine the CNC distribution in a composite is the target of our project. Fluorescence techniques have been used in the CNC composite field and may provide an alternative to detection by SPM techniques. Accordingly, an overview of fluorescence and principles of florescence techniques will be given.

1.2.4.1 Introduction to Fluorescence

When a molecule is excited by light, an electron can transition from the ground state to an excited state. From the excited state, the electron can return to the ground state via different pathways. One is a radiative pathway which may go through a singlet state (Fluorescence) or through intersystem crossing into a triplet state that then emits (phosphorescence). Other ways of depopulating the excited state include non-radiative relaxation (which is also called internal conversion) or quenching. The Jablonski diagram shown in Figure 1-21 is used to explain the

various processes that occur after absorption of light. Florescence is the emission arising from a singlet excited state, where the excited state typically has a lifetime several nanoseconds. During this time, the fluorophore undergoes conformational changes and the energy of S1 is partially dissipated by vibrational relaxation. Due to this energy dissipation, the energy of the emitted photon is lower, and therefore occurs at a longer wavelength, than the excitation photon. The difference in energy or wavelength between the absorbed and emitted photon is called the Stokes shift (Figure 1-22). Return of the excited state electron to its ground state is spin allowed and occurs rapidly at a rate of 10^8 s^{-1}. An ideal homogeneous system (fluorophore in uniform solvent) would show a single lifetime, whereas heterogeneous systems (most real systems) typically show multiple lifetimes.[47]

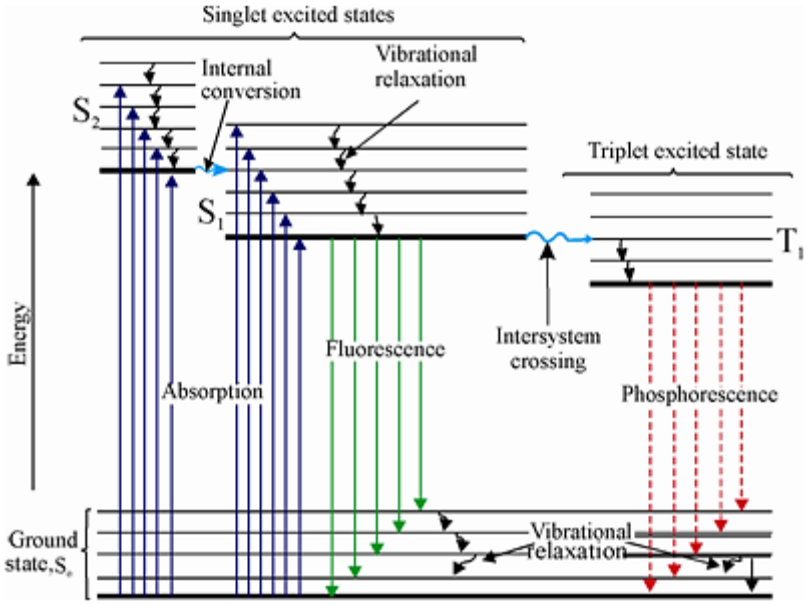

Figure 1-21: Jablonski energy diagram. Adapted from expertsmind.com.[48]

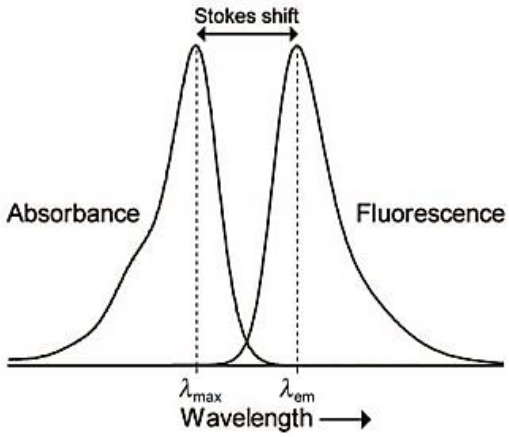

Figure 1-22: Absorption and fluorescence spectra. The Stokes shift results in an emission wavelength that is longer than the excitation wavelength. Adapted from reference [49].

There are two important parameters that need to be introduced: quantum yield (Φ) and extinction coefficient (ε). The fluorescence quantum yield (Φ) is the ratio of photons emitted through fluorescence to photons absorbed. Quantum yields (Φ) vary between 0 (no fluorescence) and 1. In other words the quantum yield gives the probability of the excited state being deactivated by fluorescence rather than by another, non-radiative or phosphorescence mechanism. The extinction coefficient defines how strongly a substance absorbs light at a given wavelength, per mass density or per molar concentration. It is defined by Beer-Lambert's law,

$$\varepsilon = A/c\ L \qquad \text{(Equation 1-9)}$$

where A is the absorption, c is the concentration of fluorophore and L is the path length of light.

In the field of fluorescence, an important phenomenon is quenching. Information about the excited state reactivity can be obtained from a study of emission quenching. In the absence of another molecule with which to react, an electronically excited molecule (M*) undergoes a

unimolecular chemical reaction or relaxes to the ground state radiatively or non-radiatively. The fluorescence emission can be characterized in terms of the total intensity and the time-dependence of its intensity[50]. If there is a reactive molecule, usually called quencher (Q), it can reduce or prevent emission of the fluorophore by collisional quenching, energy transfer, charge transfer reactions or photochemistry[51]. The following Figure 1-23 shows the difference between the emission and the quenching pathways. Collisional quenching occurs when the excited fluorophore contacts an atom or molecule that can induce non-radiative transitions easily to the ground state. Quenching by molecular oxygen is usually the major source of quenching in fluorescence experiments[51].

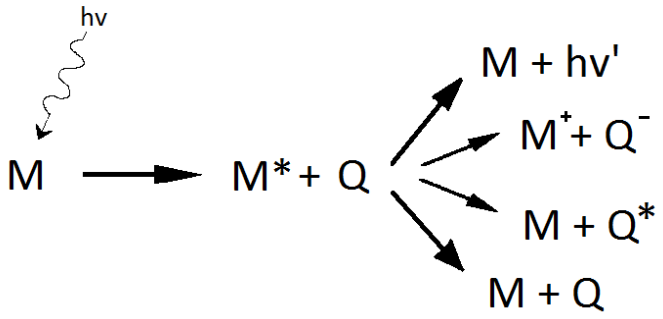

Figure 1-23: Schematic diagram of fluorescence emission and quenching. Q is the quencher.

1.2.4.2 Fluorescence spectroscopy

The first step to characterize a fluorophore's photophysical properties is to measure its excitation and emission spectra. The excitation spectrum is a plot of the efficiency with which different excitation wavelengths excite fluorescence from the molecule, while the emission spectrum is a plot of the relative distribution of energy released in the form of fluorescence measured at a fixed excitation wavelength. There are several types of fluorescence spectrophotometers, one of which is similar to UV-vis spectrophotometers except that the emission detector is positioned at a 90

degree angle from the excitation source and there is a second monochromator for monitoring the emission (shown in Figure 1-24). It is also common to detect fluorescence using a plate reader. In this case, the cuvette is replaced by a micro plate made of plastic or glass with perhaps 24 or more wells on it. Furthermore, both excitation and collection of emission occur from the same direction. This type of instrument is mostly used in biological science measurements.

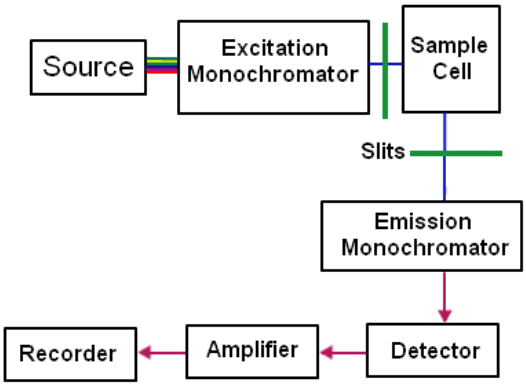

Figure 1-24: Schematic diagram of a fluorescence spectrophotometer. Adapted from reference [52]

1.2.4.3 Lifetime Measurement

Fluorescence lifetimes are ensemble-averaged values of time spent in the excited state, and are expressed as lifetime τ. A single fluorophore can undergo several decay pathways, which could include emission, transient quenching, or fluorescence resonance energy transfer (FRET). The lifetime is determined by fitting the emission intensity vs time data to a mathematical function for single-exponential or multi-exponential decays[53].

In this work, the lifetime is measured by using the time-resolved frequency-domain method (Figure 1-25). In this method, the samples are excited with light which is intensity-modulated at a high frequency that is comparable to the reciprocal of the estimated lifetime. The emission

intensity is modulated at the same frequency but is phase-shifted from the excitation curve. Both modulation frequency (ω) and phase-shift (φ) are determined by the life-time (τ) of the sample emission[53]. The relationship between the lifetime, phase shift and modulation frequency can be written as:

$$tan\varphi = \omega\tau \qquad \text{(Equation 1-10)}$$

Because of the finite lifetime of the excited state, the emission does not directly follow the excitation. The modulated emission is lower than the modulated excitation. The decay of the ratio between the modulated excitation and emission, which is also known as the frequency modulation factor (M), could provide another measurement of lifetime. The equation is:

$$M = (1 + \omega^2\tau^2)^{-1/2} \qquad \text{(Equation 1-11)}$$

Frequency-domain data plots typically show phase angle and modulation as functions of the frequency range for the experiment. The simulated frequency-domain data for a single-exponential decay is shown in Figure 1-26. The phase angle increases and the modulation decreases with increasing modulation frequency.

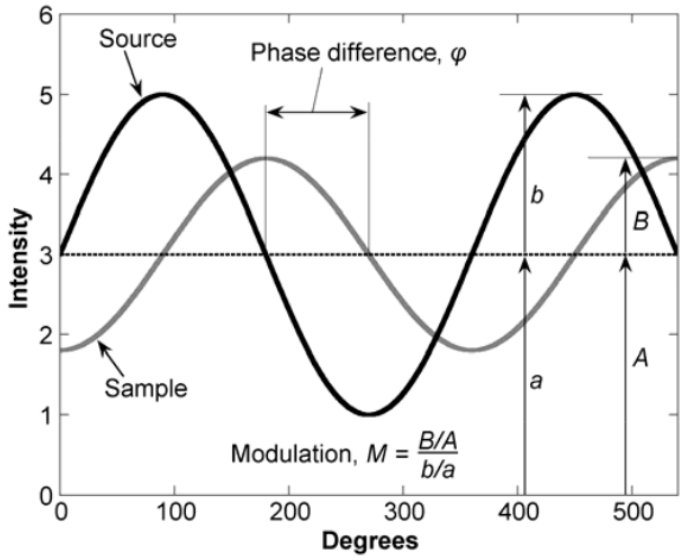

Figure 1-25: Definition of the phase angle and modulation of emission for fluorescence lifetime determination by the frequency-domain method. 'Source' means the excitation and 'Sample' means emission. Adapted from Horiba Inc. [54]

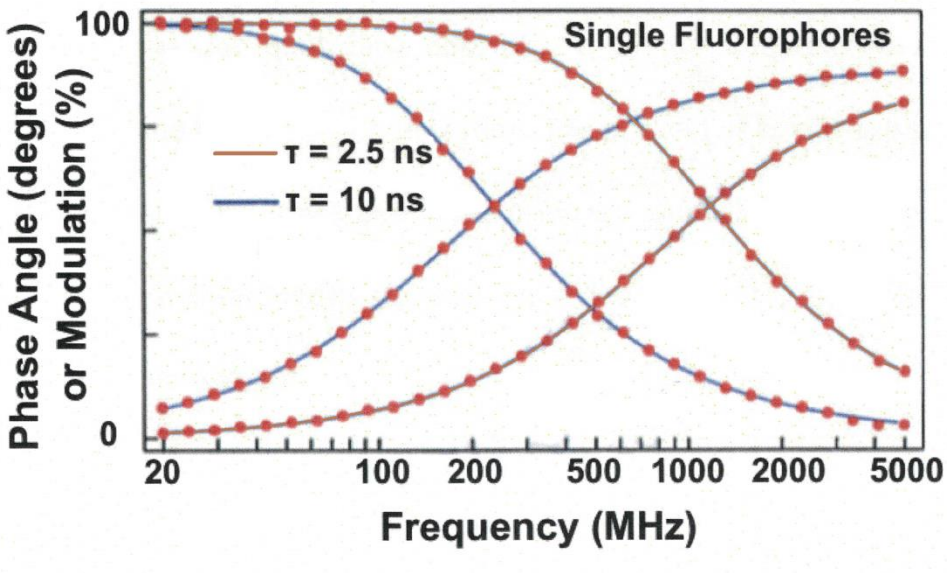

Figure 1-26: Simulated frequency-domain data for a single-exponential decay. The data points show the simulated data and the solid line is the fit for the data. Adapted from reference[49]

1.2.4.4 Fluorescence Anisotropy

Fluorescence anisotropy analysis can provide information about the environment of fluorophores. This method has been used to provide evidence that the dye molecule is attached to the CNC surface, although strong physical absorption also can lead to anisotropy changes.

This method relies on the selective excitation of fluorophores whose absorption transition dipoles are parallel to the electric field vector of polarized light. The polarized light excites only a small population of fluorophores which have their transition dipoles aligned with the polarization direction. The light emitted is also polarized as long as molecular rotation is slow relative to the fluorescence lifetime[55]. When the sample is excited with vertically polarized light, the fluorescence anisotropy is defined by:

$$r = (I_v - I_h)/(I_v + 2I_h) \qquad \text{(Equation 1-12)}$$

where, I_v and I_h are the fluorescence intensities of the vertically and horizontally polarized emissions respectively. Anisotropy can also be defined as

$$r = r_0/[1 + (\frac{\tau}{\theta})] \qquad \text{(Equation 1-13)}$$

In this equation, r_0 is the rotational diffusion anisotropy, and θ is the rotational correlation time for the diffusion process. From this definition, two scenarios can be imagined. In homogeneous solution the ground-state fluorophores are all randomly oriented and have high freedom of motion. The life time (normally in the nanosecond range) is much longer than the rotational correlation time and r tends to be small for free fluorophores. If fluorophores are attached to the CNC surface, the CNC particle rotational correlation time would be considered instead of the

fluorophore's molecular rotational time. This increases r, making it higher than the r value for free dye and indicating that the dye has been attached to the CNC surface.

1.2.4.5 Total Internal Reflection Fluorescence Microscopy (TIRFM)

Total internal reflection fluorescence microscopy (TIRFM) is rooted in its ability to selectively excite fluorophores in a very thin layer. Total internal reflection occurs when the incident excitation laser beam reflects (or bends) at the interface between two media with different refractive indices. The schematic diagram of TIRF is shown in Figure 1-27[56].

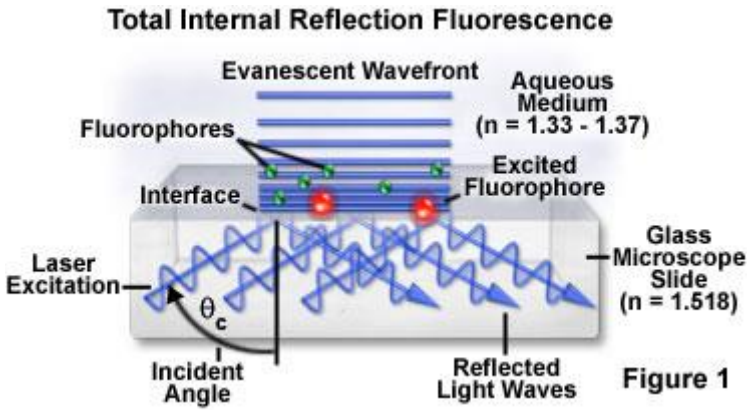

Figure 1-27: Schematic diagram of TIRF, adapt from Nikon Inc.[56]

The laser beam is refracted at the interface between the glass and sample; the refractive index of the sample medium has to be lower than the refractive index of the slide for total internal reflection to occur.

The relationship between the angles of incidence (θ_1) and refraction (θ_2) and the refractive indices of the two media is described by Snell's Law. The factor n is the refractive index of medium.

$$n_1 sin\theta_1 = n_2 sin\theta_2 \quad \text{(Equation 1-14)}$$

The critical angle of incidence (θ_c) is the incident angle at which the light travels along the interface between the two different media. It can be calculated by equation 1-15.

$$Sin\theta_c = n_1/n_2 \quad \text{(Equation 1-15)}$$

For the incident light angles higher than θ_c, the light is reflected entirely back into the first medium. Thus total internal reflection (TIR) is only obtained when incident angle is greater than θ_c.

Although the light does not pass through the second medium under TIR conditions, the reflected light still propagates from the surface to create an electromagnetic field (evanescent field) in the second medium. The evanescent field intensity I(z) decreases exponentially with distance z from the interface between the two media, and depends on both the angle and the polarization of the incident light[56]. The evanescent field intensity I(z) can be described by equation 1-16[57]:

$$I(z) = I_0 \exp(-\tfrac{z}{d}) \quad \text{(Equation 1-16)}$$

The depth of penetration d does not depend on the polarization of light and is defined as the distance at which the intensity of evanescent light is 1/e of the initial intensity I_0. The depth of penetration (d) is given by:

$$d = \frac{\lambda}{4\pi} \frac{1}{\sqrt{n_1^2 sin\theta_1^2 - n_2^2}} \quad \text{(Equation 1-17)}$$

The sensitivity of TIRF is directly related to fluorescence intensity, which is at a maximum at the interface and decreases exponentially with increasing distance from the interface. In actual experiments, the interface may be stratified, which is approximated by a thin multilayer system

rather than an interface between two media[58]. Eliminating fluorescence from outside the focal plane improves the signal/noise ratio and thus provides better contrast and better resolution than the traditional epifluorescence microscope. While the resolution in optical microscopy is diffraction limited, TIRF microscopy allows imaging of cellular structures at the coverslip-cell interface with a higher z-resolution than confocal microscopy in a wide-field approach. The z-resolution of TIRF is normally less than 100 nm, while that of confocal microscopy is 300 nm[57].

Light collection and thus the performance of the lens are very important for the TIRF microscope. The numerical aperture (NA) defines the light collection capability of the lens. NA can be expressed as[59]:

$$NA = n\,sin\alpha \qquad \text{(Equation 1-18)}$$

In this equation, n represents the refractive index of the medium between the objective lens and the specimen, and α is one-half angular aperture of the objective[59]. In TIRF, the critical incident angle (θ_c) should less than or equal to the factor α.

1.3 Objective of Thesis

An overview introducing CNC as a new generation renewable nanomaterial has been presented in this chapter. In the following chapters, the study of CNC size distribution and determination, dye-labeled CNC and CNC composite film would be introduced. A fast, low cost, and accurate way to determine the size of CNC is the first work of this project. Thus, different ways for measuring the CNC size are introduced. The advantages and disadvantages of measuring size of CNC are also showed in comparison of different techniques. Because the new CNC reference

material is dry, the way to redeposit CNC and the sonication effects of dry CNC redisposition are discussed in this thesis. The second part of this project is finding a fast, low cost and easy way to determine the CNC distribution in composite. Using fluorescence microscopy is the way which is discussed in this thesis. Thus, this project was divided to two parts. One is preparation and photo physical properties measurement of dye-labeled CNC and other is fluorescence microscopy measure result of dye-labeled CNC composite film.

1.4 References

1. Greiner, A.; Wendorff, J.; Averdung, J.; Dröscher, M., Hollow fibers are used in separation technology, catalysis, micro-electronics, medical technology, material technology or in the clothing industry. Google Patents: 2003.
2. Dufresne, A., Nanocellulose: a new ageless bionanomaterial. *Materials Today* **2013,** *16* (6), 220-227.
3. Liu, D.; Zhong, T.; Chang, P. R.; Li, K.; Wu, Q., Starch composites reinforced by bamboo cellulosic crystals. *Bioresource Technology* **2010,** *101* (7), 2529-2536.
4. De Rodriguez, N. L. G.; Thielemans, W.; Dufresne, A., Sisal cellulose whiskers reinforced polyvinyl acetate nanocomposites. *Cellulose* **2006,** *13* (3), 261-270.
5. Habibi, Y.; Goffin, A.-L.; Schiltz, N.; Duquesne, E.; Dubois, P.; Dufresne, A., Bionanocomposites based on poly (ε-caprolactone)-grafted cellulose nanocrystals by ring-opening polymerization. *Journal of Materials Chemistry* **2008,** *18* (41), 5002-5010.
6. Šturcová, A.; Davies, G. R.; Eichhorn, S. J., Elastic modulus and stress-transfer properties of tunicate cellulose whiskers. *Biomacromolecules* **2005,** *6* (2), 1055-1061.
7. Eichhorn, S.; Dufresne, A.; Aranguren, M.; Marcovich, N.; Capadona, J.; Rowan, S.; Weder, C.; Thielemans, W.; Roman, M.; Renneckar, S., Review: current international research into cellulose nanofibres and nanocomposites. *Journal of Materials Science* **2010,** *45* (1), 1-33.
8. Moon, R., MacGraw-Hill Year Book of Science and Technology. McGraw Hill, N. York: 2008.
9. Moon, R. J.; Martini, A.; Nairn, J.; Simonsen, J.; Youngblood, J., Cellulose nanomaterials review: structure, properties and nanocomposites. *Chemical Society Reviews* **2011,** *40* (7), 3941-3994.
10. Klemm, D.; Heublein, B.; Fink, H. P.; Bohn, A., Cellulose: fascinating biopolymer and sustainable raw material. *Angewandte Chemie International Edition* **2005,** *44* (22), 3358-3393.
11. Sugiyama, J.; Vuong, R.; Chanzy, H., Electron diffraction study on the two crystalline phases occurring in native cellulose from an algal cell wall. *Macromolecules* **1991,** *24* (14), 4168-4175.
12. Nishiyama, Y.; Johnson, G. P.; French, A. D.; Forsyth, V. T.; Langan, P., Neutron crystallography, molecular dynamics, and quantum mechanics studies of the nature of hydrogen bonding in cellulose Iβ. *Biomacromolecules* **2008,** *9* (11), 3133-3140.

13. Habibi, Y.; Lucia, L. A.; Rojas, O. J., Cellulose nanocrystals: chemistry, self-assembly, and applications. *Chemical reviews* **2010,** *110* (6), 3479-3500.
14. Jonoobi, M.; Harun, J.; Mathew, A. P.; Oksman, K., Mechanical properties of cellulose nanofiber (CNF) reinforced polylactic acid (PLA) prepared by twin screw extrusion. *Composites Science and Technology* **2010,** *70* (12), 1742-1747.
15. Bhatnagar, A.; Sain, M., Processing of cellulose nanofiber-reinforced composites. *Journal of Reinforced Plastics and Composites* **2005,** *24* (12), 1259-1268.
16. Sacui, I. A.; Nieuwendaal, R. C.; Burnett, D. J.; Stranick, S. J.; Jorfi, M.; Weder, C.; Foster, E. J.; Olsson, R. T.; Gilman, J. W., Comparison of the properties of cellulose nanocrystals and cellulose nanofibrils isolated from bacteria, tunicate, and wood processed using acid, enzymatic, mechanical, and oxidative methods. *ACS applied materials & interfaces* **2014,** *6* (9), 6127-6138.
17. Dong, H.; Snyder, J. F.; Williams, K. S.; Andzelm, J. W., Cation-induced hydrogels of cellulose nanofibrils with tunable moduli. *Biomacromolecules* **2013,** *14* (9), 3338-3345.
18. Eichhorn, S. J., Cellulose nanowhiskers: promising materials for advanced applications. *Soft Matter* **2011,** *7* (2), 303-315.
19. (a) Canada, N. r. c., CNC-1 Cellulose Nanocrystal Powder Cerified Reference Material Certificate of Analysis; (b) CelluForce About CelluloForce. http://celluforce.com/en/company_about.php (accessed July 30th).
20. Okano, T.; Kuga, S.; Wada, M.; Araki, J.; Ikuina, J., Nisshin Oil Mills Ltd. *Japan. JP Patent* **1999**, 98-151052.
21. Leung, A. C.; Hrapovic, S.; Lam, E.; Liu, Y.; Male, K. B.; Mahmoud, K. A.; Luong, J. H., Characteristics and Properties of Carboxylated Cellulose Nanocrystals Prepared from a Novel One‐Step Procedure. *Small* **2011,** *7* (3), 302-305.
22. Beck-Candanedo, S.; Roman, M.; Gray, D. G., Effect of reaction conditions on the properties and behavior of wood cellulose nanocrystal suspensions. *Biomacromolecules* **2005,** *6* (2), 1048-1054.
23. Elazzouzi-Hafraoui, S.; Nishiyama, Y.; Putaux, J.-L.; Heux, L.; Dubreuil, F.; Rochas, C., The shape and size distribution of crystalline nanoparticles prepared by acid hydrolysis of native cellulose. *Biomacromolecules* **2007,** *9* (1), 57-65.
24. Xu, S.; Girouard, N.; Schueneman, G.; Shofner, M. L.; Meredith, J. C., Mechanical and thermal properties of waterborne epoxy composites containing cellulose nanocrystals. *Polymer* **2013,** *54* (24), 6589-6598.
25. Qian, D.; Dickey, E. C.; Andrews, R.; Rantell, T., Load transfer and deformation mechanisms in carbon nanotube-polystyrene composites. *Applied physics letters* **2000,** *76* (20), 2868-2870.
26. Dufresne, A., *Nanocellulose: from nature to high performance tailored materials*. Walter de Gruyter: 2012.
27. Mariano, M.; El Kissi, N.; Dufresne, A., Cellulose nanocrystals and related nanocomposites: Review of some properties and challenges. *Journal of Polymer Science Part B: Polymer Physics* **2014,** *52* (12), 791-806.
28. Petersson, L.; Kvien, I.; Oksman, K., Structure and thermal properties of poly (lactic acid)/cellulose whiskers nanocomposite materials. *Composites Science and Technology* **2007,** *67* (11), 2535-2544.
29. Espino-Pérez, E.; Bras, J.; Ducruet, V.; Guinault, A.; Dufresne, A.; Domenek, S., Influence of chemical surface modification of cellulose nanowhiskers on thermal, mechanical, and barrier properties of poly (lactide) based bionanocomposites. *European Polymer Journal* **2013,** *49* (10), 3144-3154.
30. Meyer, E., Atomic force microscopy. *Progress in surface science* **1992,** *41* (1), 3-49.
31. Pollak, F. H.; Cardona, M., Piezo-Electroreflectance in Ge, GaAs, and Si. *Physical Review* **1968,** *172* (3), 816.
32. Travis Heffernan, M. F., Piezoelectric Material. Santa Rosa Junior College: 2007.

33. V. J. Morris, A. R. K., A. P. Gunning, *Atomic Force Microscopy for biologists*. Imperial College Press: 1999.
34. V. J. Morris, A. R. K., A. P. Gunning, *Atomic force microscopy for biologists*. Imperial College Press: 1999; p 44.
35. Naeem, R. Lennard-Jones Potential. http://chemwiki.ucdavis.edu/Physical_Chemistry/Intermolecular_Forces/Lennard-Jones_Potential (accessed May 19th).
36. NT-MDT Effect of the tip curvature radius and cone angle. http://www.ntmdt.com/spm-basics/view/effect-tip-radius-cone-angle (accessed May 1st).
37. Berne, B. J.; Pecora, R., Dynamic light scattering with application to chemistry, biology and physics. *Courier Dover, New York* **1976**.
38. Instruments, M. Dynamic lighting scattering *An introduction in 30 minutes* [Online], p. 3-5.
39. Siegert, A., Radiation laboratory report no. 465. *Massachusetts Institute of Technology, Cambridge, MA* **1943**.
40. Shibata, M.; Inoue, Y.; Miyoshi, M., Mechanical properties, morphology, and crystallization behavior of blends of poly (L-lactide) with poly (butylene succinate-co-L-lactate) and poly (butylene succinate). *Polymer* **2006,** *47* (10), 3557-3564.
41. Edward, J. T., Molecular volumes and the Stokes-Einstein equation. *Journal of Chemical Education* **1970,** *47* (4), 261.
42. Zwanzig, R.; Harrison, A. K., Modifications of the Stokes–Einstein formula. *The Journal of chemical physics* **1985,** *83* (11), 5861-5862.
43. Instruments, M. DYNAMIC LIGHT SCATTERING COMMON TERMS DEFINED 2011, p. 2. http://www.biophysics.bioc.cam.ac.uk/wp-content/uploads/2011/02/DLS_Terms_defined_Malvern.pdf (accessed July 27 2015).
44. Boluk, Y.; Danumah, C., Analysis of cellulose nanocrystal rod lengths by dynamic light scattering and electron microscopy. *Journal of nanoparticle research* **2014,** *16* (1), 1-7.
45. Brown, S. C.; Boyko, V.; Meyers, G.; Voetz, M.; Wohlleben, W., Toward advancing nano-object count metrology: a best practice framework. *Environmental health perspectives* **2013,** *121* (11-12), 1282.
46. Williams, D. B.; Carter, C. B., *The transmission electron microscope*. Springer: 1996.
47. Mátyus, L.; Szöllősi, J.; Jenei, A., Steady-state fluorescence quenching applications for studying protein structure and dynamics. *Journal of Photochemistry and Photobiology B: Biology* **2006,** *83* (3), 223-236.
48. Jablonski Diagram http://www.expertsmind.com/topic/fluorimetry-and-phosphorimetry/jablonski-diagram-913753.aspx (accessed Mat 6th).
49. Lakowicz, J. R.; Masters, B. R., Principles of fluorescence spectroscopy. *Journal of Biomedical Optics* **2008,** *13* (2), 9901.
50. Andrew Gilbert , J. B., *Essentials of Molecular Photochemistry*. CRC PRESS Inc.: 1991.
51. Rehm, D.; Weller, A., Kinetics of fluorescence quenching by electron and H ‐ atom transfer. *Israel Journal of Chemistry* **1970,** *8* (2), 259-271.
52. Molecular Luminescence Spectroscopy. http://chemistry.tutorvista.com/analytical-chemistry/molecular-spectroscopy.html (accessed May 28th).
53. Valeur, B.; Berberan-Santos, M. N., *Molecular fluorescence: principles and applications*. John Wiley & Sons: 2012.
54. Group, S. F. Which Fluorescence Lifetime System is Best for You? 2004.
55. Lackowicz, J., Principle of Fluorescence Spectroscopy. Springer, New York: 2006; pp 353-382.
56. Stephen T. Ross, S. S., Thomas J. Fellers, Michael W. Davidson Total Internal Reflection Fluorescence (TIRF) Microscopy. https://www.microscopyu.com/articles/fluorescence/tirf/tirfintro.html (accessed May 11th).

57. Trache, A.; Meininger, G. A., Total internal reflection fluorescence (TIRF) microscopy. *Current protocols in microbiology* **2008**, 2A. 2.1-2A. 2.22.
58. Burmeister, J. S.; Olivier, L. A.; Reichert, W.; Truskey, G. A., Application of total internal reflection fluorescence microscopy to study cell adhesion to biomaterials. *Biomaterials* **1998,** *19* (4-5), 307-325.
59. Davidson, M. W. Numerical Aperture. https://www.microscopyu.com/articles/formulas/formulasna.html (accessed May 15th).

Chapter 2

Characterization of Cellulose Nanocrystal (CNC) Size Distribution

2.1 Introduction

Particle size distribution is one of the most important properties to characterize for any nanomaterial. The particle size of CNCs controls their behavior for applications as additives to increase the mechanical strength of composites, as additives to control the rheology of solutions and for producing thin film coatings, especially those with useful optical properties. The particle size distribution is also an essential quality control parameter for commercial producers of CNCs[1]. For the industry, an efficient, low cost, and real-time detection of particle size distribution is important. Controlling and measuring the particle size is also crucial for assessing the environmental health and safety aspects of nanomaterials. Although CNC is considered a relatively non-toxic nanomaterial, increasing emphasis on regulations for the use of nanomaterials will probably also apply to CNC. Despite the importance of measuring particle size, it is still challenging to develop reproducible and easy to implement methods that can be implemented for routine measurements.

CNC particle size distribution has been measured in a number of studies; different size distributions have been observed as a function of hydrolysis conditions and the type of cellulose biomass used[1-2]. However the lack of standard methods and approaches makes it quite difficult to draw comparisons between the various studies. The measurement of CNC particle size distribution has many of the same challenges that face other nanomaterials[3]. For example, particle size varies depending on the method used, the measurement of nano-sized particles requires expensive and difficult to use instrumentation and direct measurements require statistics for large numbers of particles. However, the measurement of CNC size distribution is more complex than for many other nanoparticles (such as metal and silica nanoparticles) due to their

nanorod shape, their broad size distribution and the strong tendency of the particles to aggregate even at low concentrations.

CNCs derived from wood pulps are small nanorods which have ~100 nm length and 5 nm height and a broad size distribution[2c]. Only EM and SPM[2c] have enough resolution to measure both the length and width or height. Both TEM and AFM have been widely used for CNC size measurement, although there are limitations. CNC contains no heavy atoms so has low contrast in TEM and a heavy metal stain has to be used to improve contrast. Furthermore, the number of particles that have to be counted to obtain results that are representative of the bulk sample is large. The number of count needed to distinguish between similar distributions is frequently not taken into account.

Ensemble techniques that can examine the entire sample, such as dynamic lighting scattering (DLS)[4] and small angle neutron scattering (SANS)[5] are also of interest for measuring CNC sizes . However, the ensemble scattering methods for measuring particle size distributions are challenging for high aspect ratio CNC nanorods, because the data analysis methods typically assume spherical particles. Despite the experimental observations of either square or rectangular cross sections of CNC particles, they have usually been treated as cylinders with mean diameter and length[6]. The tendency of CNCs to form large and tightly packed aggregates has so far limited the measurement of average particle size. Although light scattering methods are difficult to apply to non-spherical particles, they are much easier, faster and cheaper to use, than the expensive and time-consuming microscopy methods.

In this chapter, several experiments performed to characterize the size of CNC particles will be presented. Size distribution measurements by TEM, AFM or DLS are presented and a

comparative study between the different methods will be discussed. The effect of sonication on the size distributions from AFM and DLS is examined. Furthermore, a reliable and reproducible method for re-dispersing dry CNC powder will be explored in this chapter since CNC is often stored in a dry environment due to its stability but is almost always re-dispersed prior to characterization or use in applications[4].

2.2 Experimental

2.2.1 Types of CNC samples

CNC-1: The first generation CNC reference material was produced by National Research Council Canada (NRC). The CNC was prepared by sulfuric acid hydrolysis of softwood pulp by FPInnovations, Montreal and has sulfate groups on the surface. It is a spray dried CNC powder which was stored in a 2 g brown glass bottle in a 4 ℃ refrigerator until use. The sample was well sealed after being opened.

CNCS-1: The first generation CNC reference material was produced by NRC. The CNC was prepared by sulfuric acid hydrolysis of softwood pulp by FPInnovations, Montreal and has sulfate groups on the surface. It is a never dried CNC 6 wt. % suspension which was stored in a 20 ml brown glass bottle at 4 ℃. The sample was well sealed after being opened. As a suspension, the pH has been measured to be 3.97.

CNC-Maine: The CNC material was bought from Process Development Center of the University of Maine. The sample was prepared by sulfuric acid hydrolysis of softwood pulp and has sulfate groups on the surface. It is a never dried CNC 11.5 wt. % suspension which was

stored in a 10 L plastic bucket. Because of its size and non-refrigerated history, the sample was stored at room temperature. The pH of a sample of the suspension was measured to be 4.42.

CNC-2: The second generation CNC reference material was produced by NRC. Sample was prepared by sulfuric acid hydrolysis of softwood pulp by a commercial supplier and has sulfate groups on the surface. CNC-2 is a spray dried powder and was stored in a 2 g or 5 g brown glass bottle at 4 ℃. The sample was well sealed after being opened.

All the samples are also listed in Table 2-1.

Table 2-1: Properties of CNC samples used in this thesis.

Sample Name	Sample type	Storage Temperature	Surface Function Group	pH
CNC-1	Spray dried powder	4 ° C	Sulfate, hydroxyl	N/A
CNCS-1	Never dried 6 wt. % suspension	4 ° C	Sulfate, hydroxyl	3.97
CNC-Maine	Never dried 11.5 wt. % suspension	Room Temperature	Sulfate, hydroxyl	4.42
CNC-2	Spray dried powder	4 ° C	Sulfate, hydroxyl	N/A

2.2.2 Atomic force microscopy (AFM)

For the never dried CNC sample preparation, a pipette was used to remove a certain volume of the original CNC suspension. It was added to a 50 mL centrifuge tube and diluted to 1 wt. % suspension with 18.2 M ohm/cm MilliQ water. The suspensions were left for 5 minutes and shaken by a deluxe mixer (Canadian Laboratory Supplies, S8220) for 10 seconds at room temperature to create a uniform dispersion. For the dry CNC sample, the method described in chapter 2.2.5 was used create a 2 wt. % suspension. All the suspensions (1 wt. % for never dried CNC and 2 wt. % for re-dispersed dry CNC were then diluted with MilliQ water to 0.001 wt. %. Samples for AFM were prepared on freshly cleaved square mica (Ted Pella Inc. Hi-Grade Mica, Grade V2, 25 mm × 25 mm) slides. 50 μL of 0.01 M poly-L-lysine solution (PLL, Sigma-Aldrich, and Molecular Wt. 70000-150000) was deposited on the fresh mica surface and incubated for 30 minutes. The PLL coated mica was rinsed twice with MilliQ water and blown dry with dry N_2 gas (relative humidity near 0). Then, a 50 μL droplet of 0.001 wt. % CNC suspension was deposited onto the fresh PLL coated surface and incubated for 1 minute. The sample was rinsed with MilliQ water to wash away free CNC particles. The water was gently streamed over the edge of the mica surface and the sample was blown dry with N_2 for imaging in air by AFM.

Tapping mode (intermittent contact mode) AFM imaging was performed at room temperature in air using the JPK NanoWizard® II AFM. The tip used was the MikroMasch HQ: DEP-XCS-11 cantilever B which has a typical spring constant of 2.7 N/m, a resonance frequency of 80 kHz and is platinum coated. An area of 1×1 μm^2 was scanned with 512 ×512 pixel resolution (1.95 nm per pixel). The set point was adjusted to around 70% of the free amplitude such that minimum scanning force was used to obtain applied force-independent height measurements.

Applied forces were maintained within a range where the measured sample height was independent of the applied force, as verified by measuring images at several different set points. Normally, because of the tip ageing, ~4 tips are typically used for a single particle size characterization based on ~300 particles from ~20 images.

The AFM images for CNCS-1 size characterization were obtained by Dr. Maohui Chen. The CNCS-1 suspension was diluted 10000 times with MilliQ water and deposited on poly-lysine-coated mica slides as introduced before. Samples were imaged at room temperature (21 ℃) in air using a PicoSPM atomic force microscope (Molecular Imaging) which was calibrated with standard grids prior to use. Magnetic coated silicon tips (MAC Levers Type VII) with nominal spring constants of 0.14 N/m were used. In this thesis, all the AFM images are recorded by the author unless otherwise noted. The images from Dr. Chen were only used for the size measurement of 300 particles from CNCS-1.

The AFM data was analyzed by Gwyddion software v 2.41. Using the software, the image was levelled by subtracting the mean plane twice and the lines were corrected by matching the height median once. Then the minimum data value was shifted to zero and the height range was fixed at 0 to 12 nm. Typically the images had a mixture of individual and aggregated CNCs, but only single CNCs were analyzed for size measurement and particles touching the edge of the slide were not analyzed. CNCs were measured manually using the ‘extract profiles’ tool in Gwyddion.

2.2.3 Dynamic lighting scattering (DLS)

The DLS measurements were performed following a procedure modified from reference[7]. The CNC suspensions were diluted with MilliQ water to 2 wt. % as the initial stock solution. Then, 0.25 mL 2 wt. % suspension was diluted with 8.75 mL Milli-Q water and 1 mL 50 mM NaCl

solution to obtain 0.05 wt. % suspensions in 5 mM NaCl. The samples were injected into DTS1060C/ DTS1070 zeta cell (Malvern) sample cells through a 0.45 μm PVDF filter to remove CNC aggregates and larger impurities. The cell was placed in an instrument sample holder, and the temperature was equilibrated to 25 ℃ for 180 s. The DLS measurements were conducted using the Zetasizer Nano ZS (Malvern) which has a 173 °detector and 50 mW 633nm laser source. The dispersant viscosity at 25 ℃ was 0.8872 cP (water). The sample refractive index was 1.469 and dispersant refractive index was 1.330 [4]. Each sample was measured three times, with each measurement consisting of three 50-second-long runs. All DLS data was analyzed by Malvern nanosizer software which uses the normal resolution cumulants analysis method.

The DLS instrument was calibrated monthly with ERM-FD304 certified reference material, which is a silica nano bead sample with a certified Z-average value of 41.64 nm.

2.2.4 Transmission electron microscope (TEM)

The TEM images were recorded by Dr. M. Couillard. Samples were prepared by diluting the CNCS-1 suspension in MilliQ water to 0.001 wt. % and depositing on carbon grids. CNCs were stained with 2 % uranyl acetate for 20 seconds. TEM images were obtained on a Titan S/TEM (FEI). Size measurements were determined semi automatically using an ImageJ custom macro (modified by Dr. Zygmunt Jakubek) requiring operators to indicate particle end points for length and side edges for width measurements.. The measurement depends on the contrast of the TEM image.

2.2.5 Dry CNC re-dispersion

The dried CNC powder was placed in a 50 mL centrifuge tube and 18.2 M Ω/cm MilliQ water was added to obtain a 2 wt. % suspension. The suspensions were left overnight (12 hours) at

room temperature to disperse the dry CNC powder. After 12 hours, suspensions were ultrasonicated using a Cole-Parmer 130 W ultrasonic processor equipped with a 6 mm tip. Suspensions were ultrasonicated with the tip inserted approximately 15 mm into the suspensions. Unless otherwise specified sample preparation, 5000 J per g sonication energy was applied to re-disperse the dry CNC.

2.2.6 Effects of Sonication

9 samples of never dried CNCS-1 samples were prepared for DLS measurements. For each sample, approximately 1000 mg of 6 wt. % CNC suspension was placed in a 50 mL centrifuge tube, and diluted with 2000 mg of 18.2 M Ω/cm MilliQ water to obtain a 2 wt. % suspension. All suspensions were ultrasonicated using a Cole-Parmer 130 W ultrasonic processor equipped with a 6 mm tip. Suspensions were ultrasonicated with different sonication energies ranging from 0 to 10000 J per gram of CNC. Then, the ultrasonicated suspensions were diluted with MilliQ water and 50 mM NaCl to obtain 0.05 wt. % in 5 mM NaCl for DLS measurement.

For the dry CNC-2 samples, 15 samples were prepared for DLS measurements. From each bottle, approximately 300 mg of dry CNC was placed in a 50 mL centrifuge tube, and diluted with approximately 14.7 mL of 18.2 M Ω/cm MilliQ water to obtain a 2 wt. % suspension. The suspensions were left overnight (12 hours) at room temperature to disperse the CNC. After 12 hours, suspensions were ultrasonicated using a Cole-Parmer 130 W ultrasonic processor equipped with a 6 mm tip. Suspensions were ultrasonicated with different sonication energies ranging from 0 to 10000 J per gram of CNC. Because 5000 J/g is the energy which recommended in literature[7], three samples were sonicated with this energy. Then, the ultrasonicated suspensions were diluted with MilliQ water and 50 mM NaCl to obtain 0.05 wt. % in 5 mM NaCl for DLS measurement.

Each sample was injected into the DTS1060C zeta cell (Malvern) sample cell through a 0.45 μm PVDF filter. The cell was placed in an instrument sample holder, and the temperature was equilibrated to 25 ℃ for 180 s. The DLS measurements were made following the steps in chapter 2.2.3.

2.2.7 Statistical tests

The Kolmogorov–Smirnov test was done with Origin pro software. This test was used to decide whether two particle size distributions were taken from the same continuous distribution at the 0.05 significance level. The null hypothesis is that the data sets are from the same distribution. The K-S test does not assume a specific type of distribution and was used instead of a t-test which is applicable to normal distributions.

2.2.8 CNC-2 Homogeneity test

Fifteen randomly selected bottles of CNC-2 were selected for homogeneity tests. From each bottle, approximately 300 mg of dry CNC was placed in a 50 mL centrifuge tube, and diluted with approximately 14.7 mL of 18.2 M Ω/cm MilliQ (Type 1) water to obtain a 2% suspension by mass (details are shown in Table 2-2). The suspensions were left overnight (12 hours) at room temperature to disperse the CNC. Then, all suspensions were ultrasonicated using a Cole-Parmer 130 W ultrasonic processor equipped with a 6 mm tip. Suspensions were ultrasonicated with sonication energies of 5000J/g. The ultrasonicated suspensions were diluted with MilliQ water to 0.0556% by mass suspensions of CNC in water. Each suspension was mixed at a 9:1 ratio with 50 mM NaCl to obtain a 0.05% by mass suspension in 5 mM NaCl.

Table 2-2: Preparation of samples for homogeneity tests

Sample number	Bottle number	Dry CNC mass (g)	Total suspension mass (g)	Concentration by mass
1	15	0.3014	15.0909	1.997%
2	10	0.3034	15.2258	1.993%
3	13	0.3051	15.2675	1.998%
4	7	0.2963	14.8345	1.997%
5	14	0.2980	14.9005	2.000%
6	4	0.2984	14.9502	1.996%
7	6	0.3114	15.5638	2.001%
8	16	0.3008	15.0232	2.002%
9	19	0.2986	15.0087	1.990%
10	17	0.2980	14.8531	2.006%
11	9	0.3040	15.2206	1.997%
12	12	0.2992	14.9213	2.005%
13	3	0.3023	15.1794	1.992%
14	8	0.3006	15.0245	2.001%
15	5	0.3035	15.2276	1.993%

DLS of the suspensions was measured using Zetasizer Nano ZS (Malvern) as described earlier. However, the temperature was equilibrated to 25 ℃ for 300 s. Each sample was measured five times, with each measurement consisting of three 20-second-long runs.

2.3 Results and Discussion

2.3.1 AFM Size characterization of never-dried CNC

AFM characterization is a convenient, high resolution method for measuring CNC size. This method does not require complicated sample preparation and can provide high quality images. Typical CNCS-1 AFM images with different scan sizes are shown in Figure 2-1.

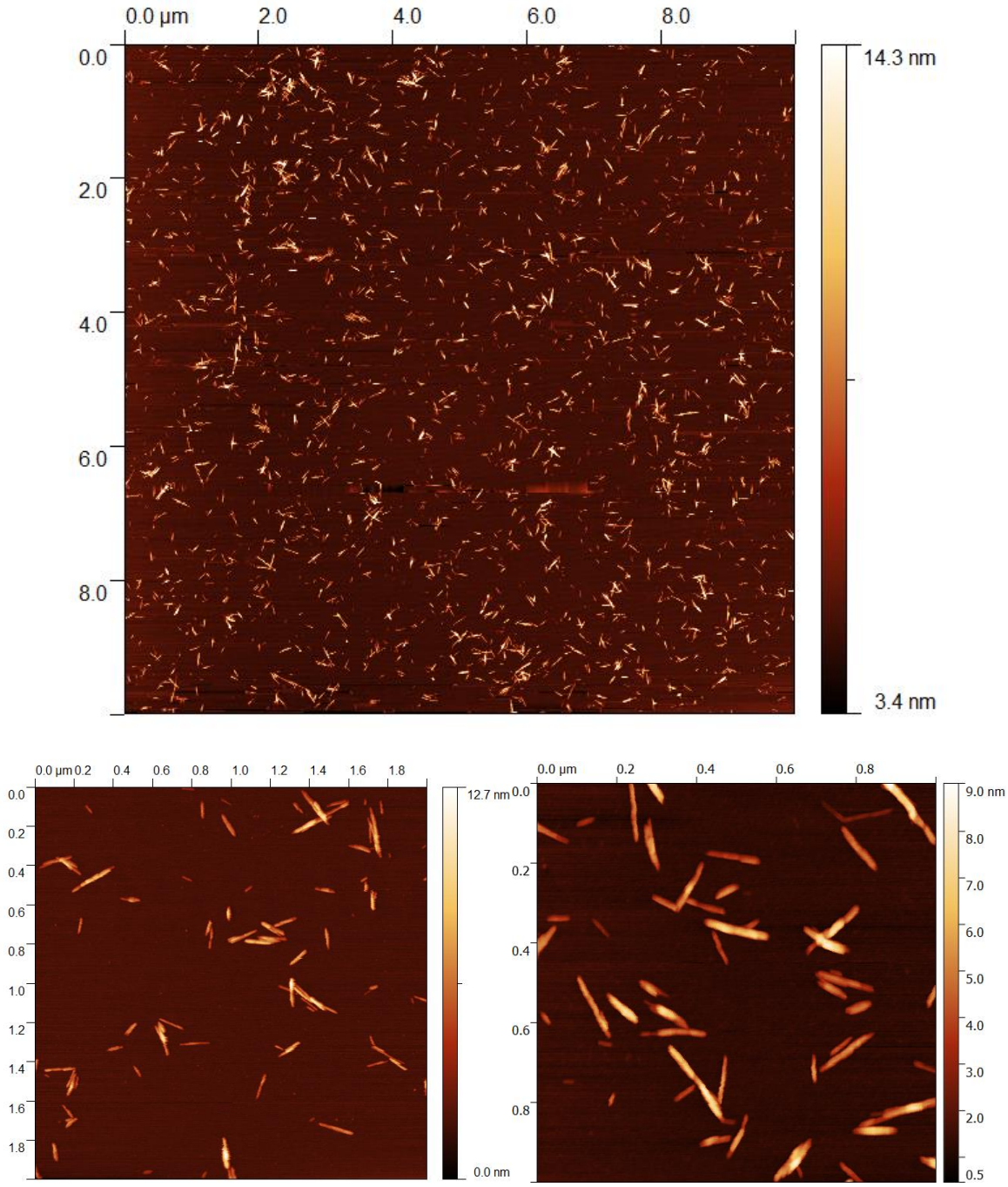

Figure 2-1: Typical never dried CNC AFM images: 10 × 10 µm^2 (top), 2 × 2 µm^2 (bottom left), and 1 × 1 µm^2 (bottom right).

From a 10 $\times$10 μm^2 scan size (Figure 2-1 top), a uniform distribution of CNC is observed with some obvious aggregates. Aggregation cannot be avoided in the samples prepared for AFM measurements. The 2 $\times$2 μm^2 (Figure 2-1 bottom left) and 1 $\times$1 μm^2 (Figure 2-1 bottom right) images show CNCs in greater detail. Only 1 $\times$1 μm^2 images were used in image analysis. This scan size was determined by optimizing resolution and scan rate, and minimizing tip aging.

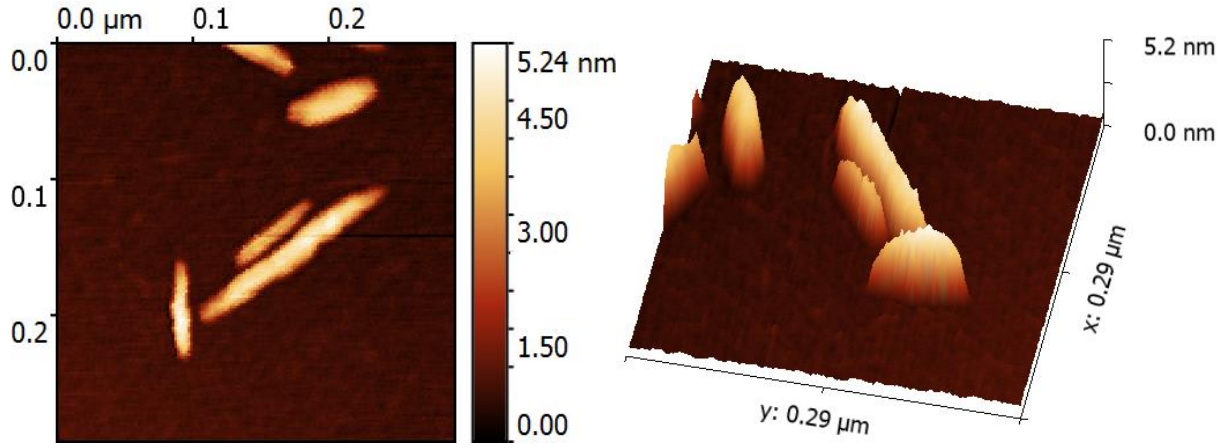

Figure 2-2: A cropped 0.3× 0.3 μm^2 image (left) from a 1 × 1 μm^2 AFM image of CNCS-1 and the corresponding 3D image (right).

An AFM image that was cropped from a 1 $\times$1 μm^2 image and the corresponding 3D image are shown in Figure 2-2. The images show that the CNC does not have a perfect cylindrical shape and has somewhat tapered ends, which also was mentioned in some literature reports[6, 8].

Before measuring the size of a large number of CNC it is important to ensure that the force applied during imaging is not compressing the particles. The set point used could affect the height measurement, and has to be carefully controlled to avoid using too much force. This was tested by scanning 500 $\times$500 nm^2 area with different set points in tapping mode. The image set point was changed from the highest value (lowest force) at which an image can be obtained to a

value that was xx lower (highest force). This measurement order (starting at low force) also helps to avoid tip contamination during the experiment. The images recorded at different set points are shown in Figure 2-3. The heights of CNCs at4 different positions were measured. Positions 1 and 3 are at the end of two single CNCs; position 2 is the center of a short CNC and position 4 is an area of two overlapping CNCs. The height measurements as a function of the set point/target amplitude ratio are shown in Figure 2-4.

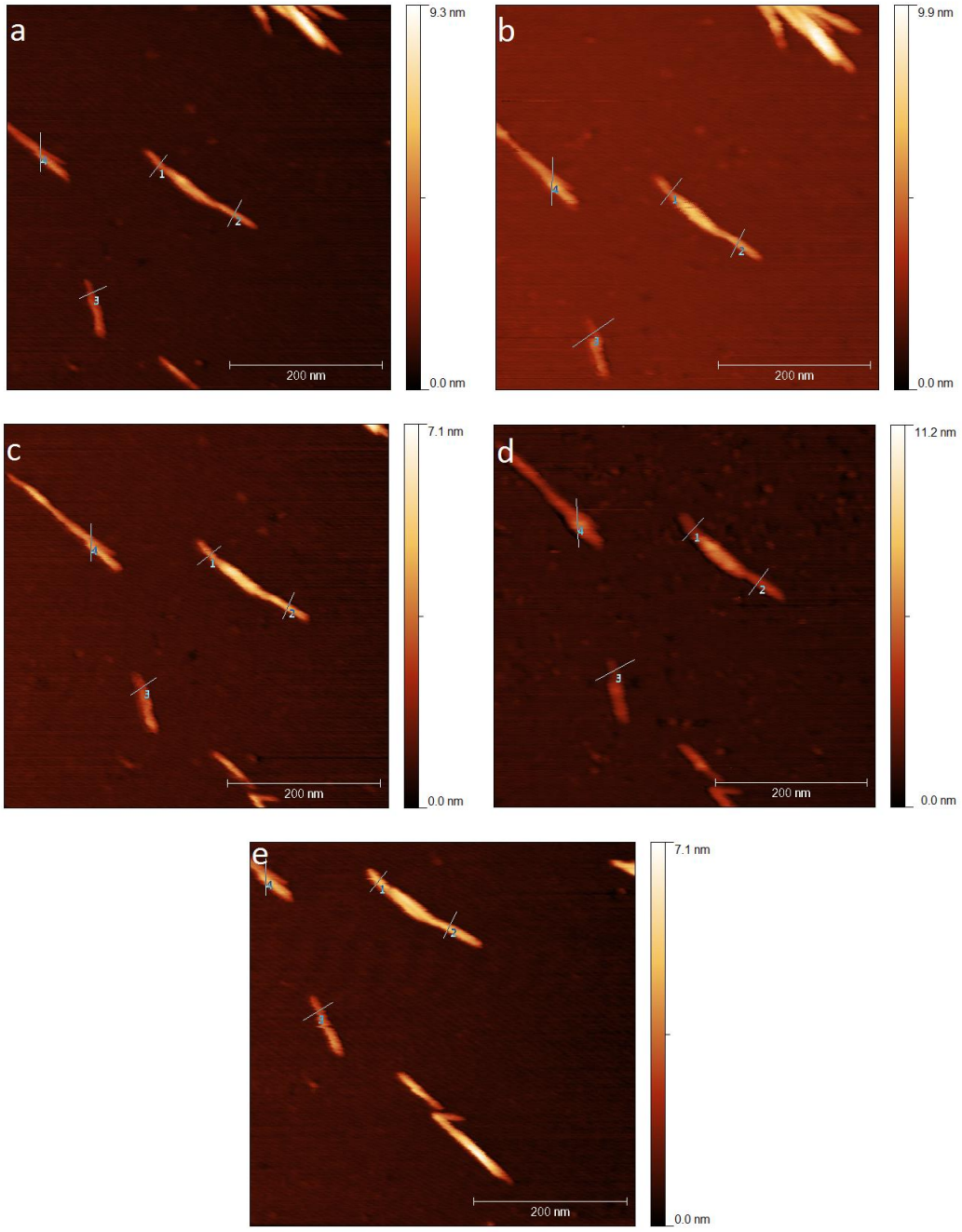

Figure 2-3: Images at different set points with free target amplitude of 2.5 V. the set point are a) 1.8 V (72 %), b) 1.65 V (66 %), c) 1.47 V (59 %), d) 1.28 V (51 %) and e) 1.1 V (44 %).

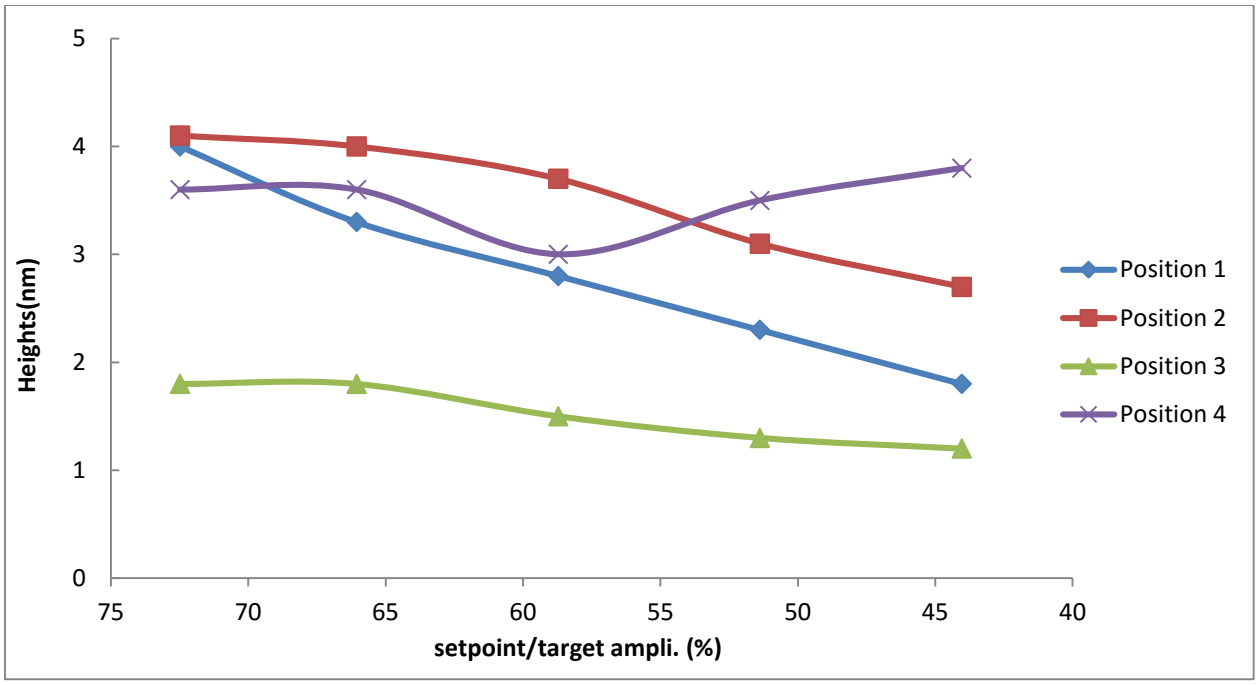

Figure 2-4: Heights at different positions vs. the ratio between set point and target amplitude.

The data in Figure 2-4 show that the height decreases when the force increases. Only position 4 which is two overlapping CNCs shows an increase at higher force. However, such an aggregate will not be measured for the size characterization. The height of position 1 decreases faster than the other positions. The heights of position 2 and 3 show a similar trend with little or no change in height between 72 % to 66 % set point ratios. These data suggest that there is a relatively narrow range of set points at which the CNC height is independent of imaging force. Thus, all the following AFM measurements used the minimum force at which stable imaging is obtained.

AFM images (1×1 μm^2) were collected for two CNC never dried suspensions for measurement of their particle size distributions. For analysis of the size of individual particles, a line was drawn through the longitudinal axis of the selected CNC particle, and its cross-section was shown in the graph window (Figure 2-5). The width of the cross section is 1 pixel. The length was measured between points at which the height signal begins to deviate from the baseline. For

the height measurement, the maximum height of the particle was obtained excluding obvious noise peaks, as illustrated in Figure 2-5. The histograms obtained by measuring 300 and 258 particles for CNCS-1 and CNC-Maine, respectively, are shown in Figure 2-6 and the results are summarized in Table 2-3.

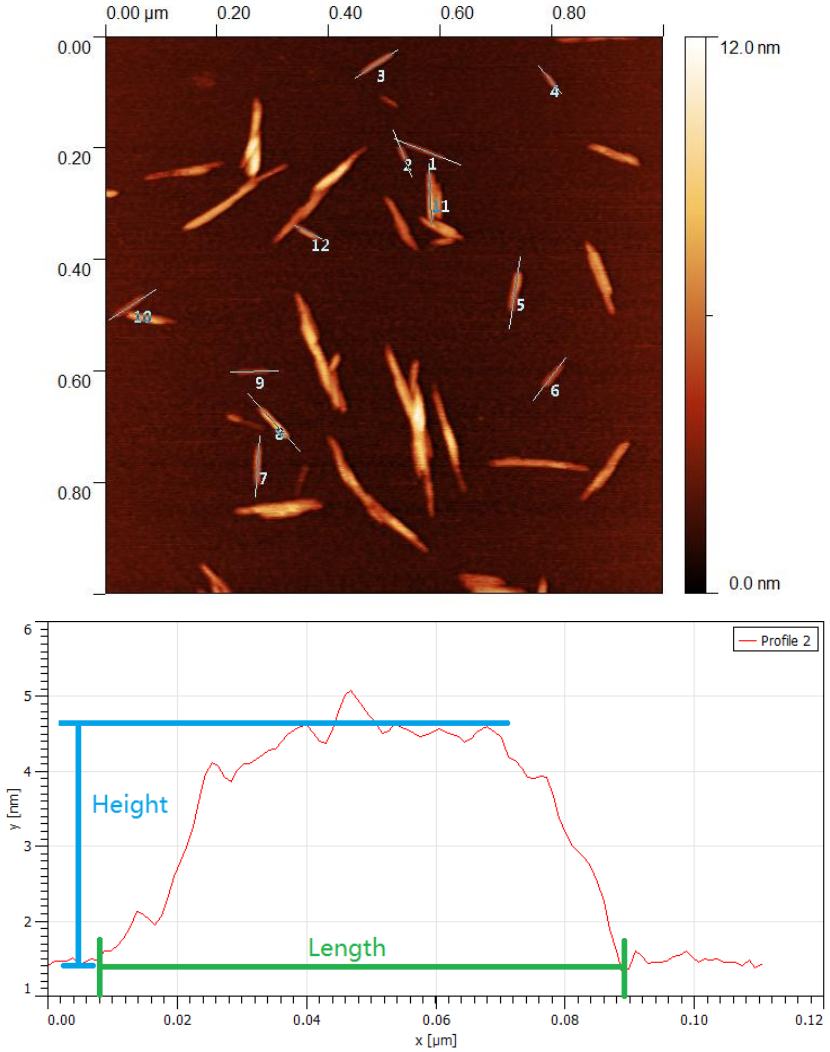

Figure 2-5: An AFM image showing the 12 CNCs selected for size analysis (top). The cross-section profile for CNC #2 is displayed in the bottom panel with the measured length and height shown in blue and green lines.

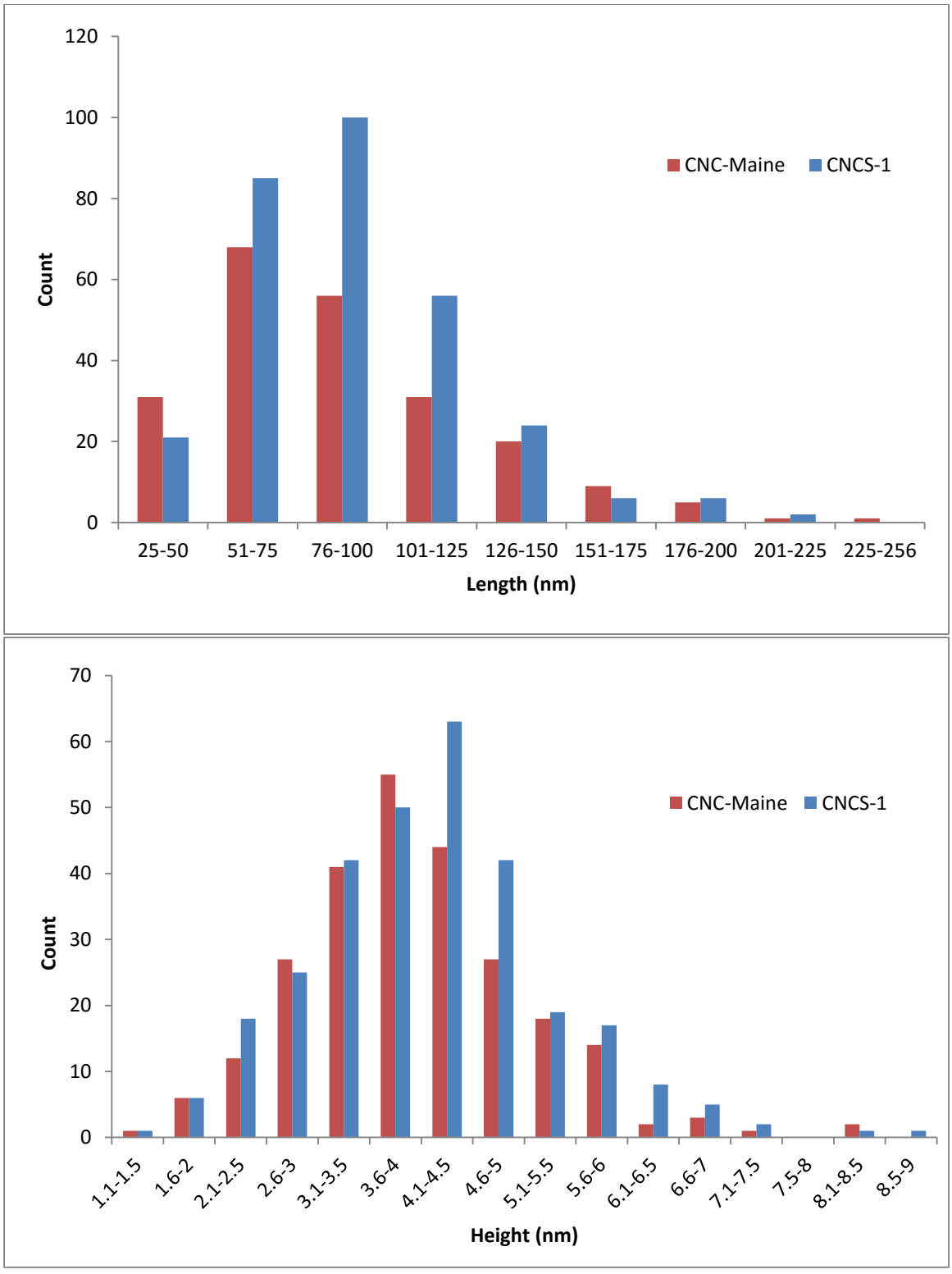

Figure 2-6: Histograms of length and height for CNCS-1 and CNC-Maine.

Table 2-3: Particle size distributions for never dried CNCs measured by AFM.

AFM	Length (nm)	Height (nm)	Count
CNC-Maine	89.5±38.3	4.1±1.1	258
CNCS-1	91.0±32.4	4.2±1.2	300

The average lengths and heights are very similar for 2 samples (Table 2-3). The size distribution of CNC fits a lognormal distribution[1, 6] and is not suitable for a two sample t-test which applies only to normal distributions. Thus, the nonparametric K-S test which can be applied to any distribution was used in this case. The K-S test indicates that the length and height of CNCS-1 and CNC-Maine are not significantly different.

2.3.2 TEM, AFM comparison

Examples of typical TEM images for CNCs stained with uranyl acetate and deposited on a carbon grid are shown in Figure 2-7. All the images are $1 \times 1\ \mu m^2$ with 1000×1000 pixels resolution. TEM images show both isolated and agglomerated CNCs, similar to the AFM results. Based on the TEM images, uranyl acetate was not washed out completely during sample preparation and forms dark patches in some areas of the images (Figure 2-7 left). These dark patterns can affect the measurement of the CNC size.

Size measurements of CNC were done semi automatically using an ImageJ custom macro. This macro requires the operator to indicate single particle end points for length measurements and side edges for width measurements from a gray value plot (Figure 2-8). When the operator draws a line through the longitudinal axis of a single CNC (Figure 2-8 b), the cross section is displayed

(Figure 2-8 c). At same time, a width cross section drawn perpendicularly through the middle of the first line is also displayed (Figure 2-8 d).

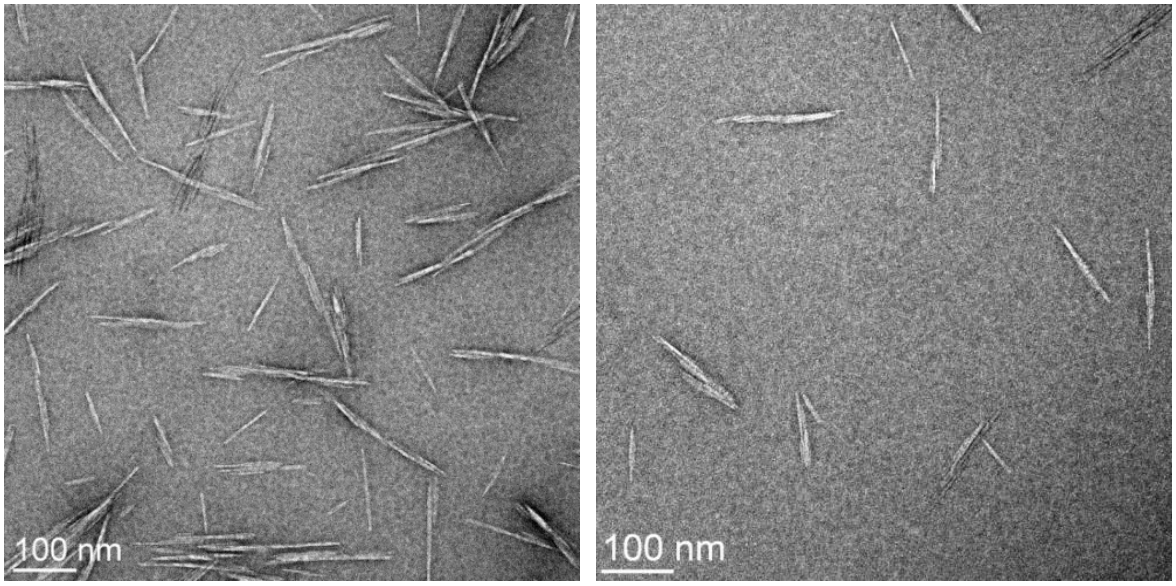

Figure 2-7: Typical TEM images for uranyl acetate stained CNCs on carbon grids, with higher CNC density (left) and lower density (right).

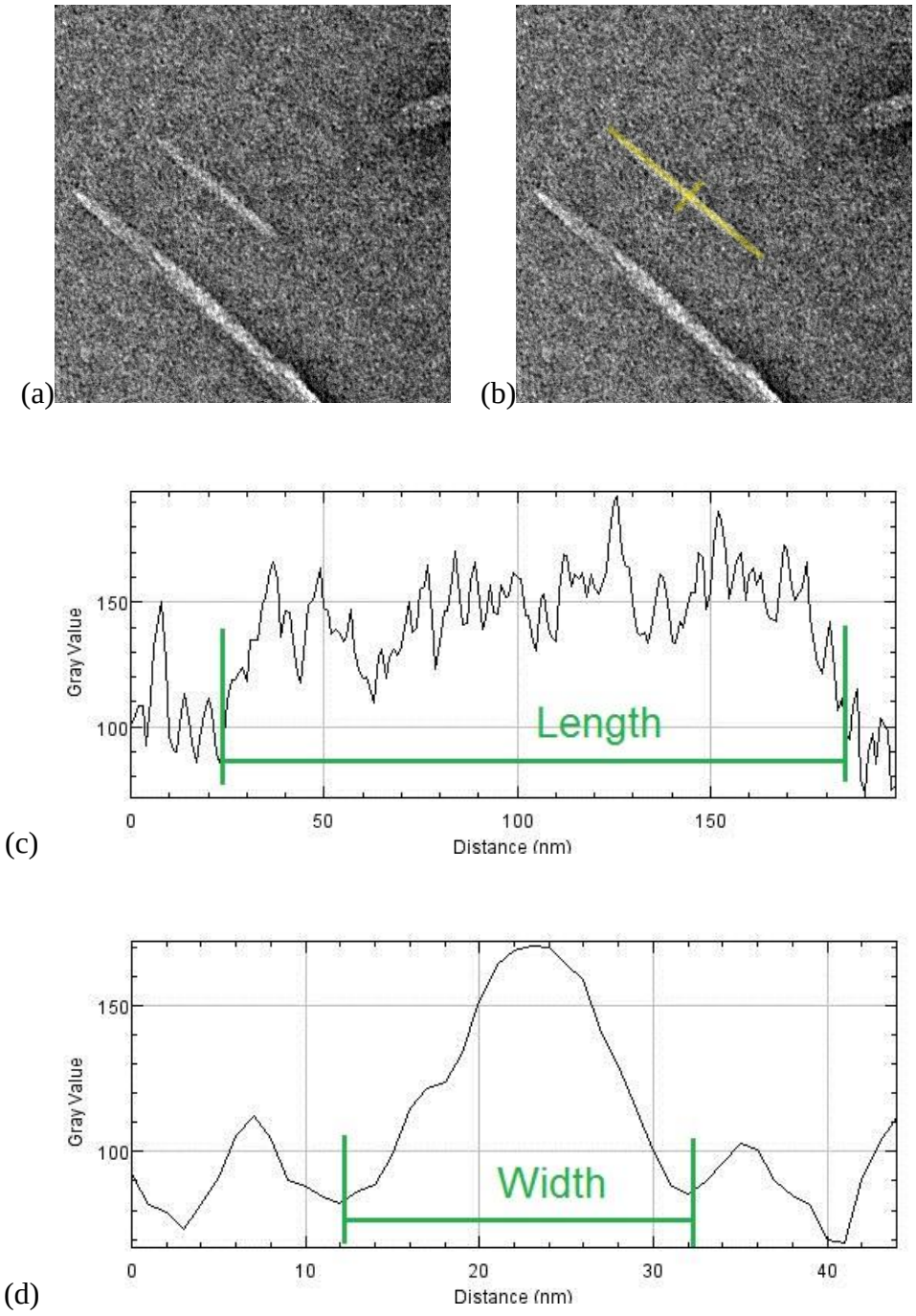

Figure 2-8: An enlarged TEM image (a) and the ImageJ macro analysis for this image (b). The image size is 400 × 400 nm^2. The length cross-section plot of the selected CNC (c) and the width cross-section plot of the selected CNC (d) are shown.

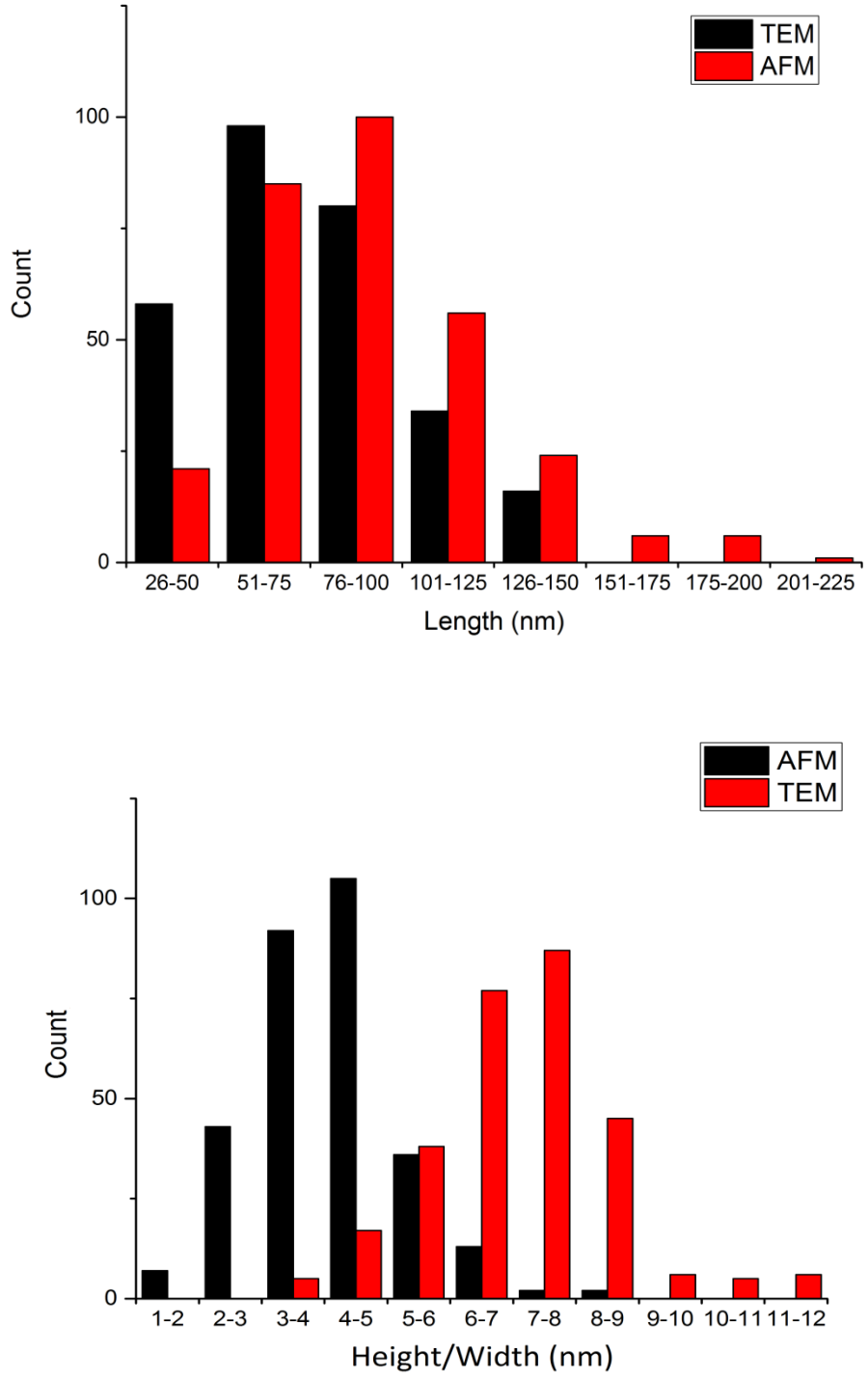

Figure 2-9: Length and height/width distribution histogram of AFM and TEM.

Table 2-4: CNCS-1 size comparison between AFM and TEM.

	Length (nm)	Width/Height (nm)	Count number
AFM	91.0±32.4	4.2±1.2	300
TEM	75.4±26.9	7.1±1.5	286

The results obtained by analyzing 286 CNCs from TEM images are shown in Figure 2-9 and Table 2-4 and are compared to AFM images for the same sample. The average length in AFM is ~15 nm larger than the average length in TEM. The K-S test indicates that both length and width/height are significantly different for the two data sets. Tip convolution effects are one possible reason for this difference (Figure 2-10). The movement of the tip across the object surface can be approximated by a sphere of radius R moving over sphere of radius r. As a result, the tip convolution effect can be approximated by the formulas[9]

$$r_c = 2\sqrt{Rr} \quad \text{(Equation 2-1)}$$

$$r_{extra} = r_c - r \quad \text{(Equation 2-2)}$$

Because the typical tip radius is 8 nm and the CNC radius is 2.1 nm (from the height measurement), r_c = 8.2 nm and r_{extra} = 6.1 nm can be calculated. The AFM average length corrected for the tip convolution effect is about 78.8 nm which is close to the average of the TEM measurement (Table 2-4). However, there are some assumptions with this correction. This calculation assumes that the end of the CNC is spherical which is not accurate. In fact, the ends are clearly tapered as shown in both AFM and TEM images. Furthermore, the CNC shape is more likely square or rectangular not cylindrical.[6, 10]

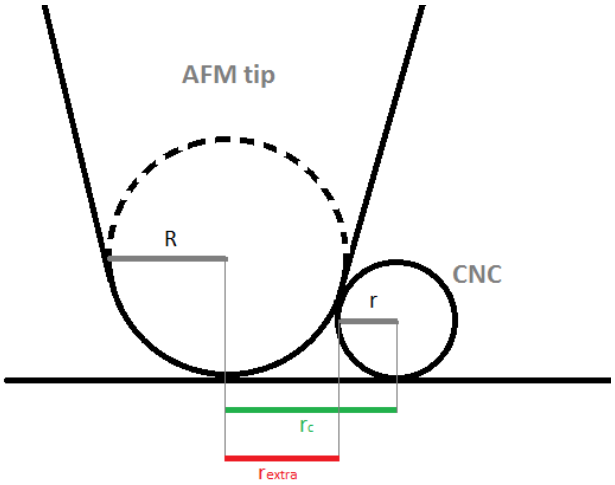

Figure 2-10: Scheme showing the tip convolution effect for CNC imaging. R is the radius of AFM tip and r is the radius of CNC.

The width measured by TEM is significantly larger than the height measured by AFM. This difference is not due to convolution effects of the AFM tip since these are not an issue for height measurements. The disparity between the two measurement methods may be a result of the CNC sample. One possible reason is that the CNC height does not equal the width, which has been reported previously in the literature[6]. The other possible reason is that one or both of the methods for depositing CNC on the solid supports (mica or TEM grids) used for AFM and TEM fail to select a representative population of particles. This could occur if the deposition is selective for a specific size of particles, e.g. one size of particle is selectively removed during sample washing. It could also occur if the aggregation of particles on the two supports occurs with some selection for specific particle sizes. An additional complication for TEM sample preparation is the requirement to stain the sample with uranyl acetate to enhance the contrast. Background staining of the grid frequently makes it difficult to distinguish the particle edge accurately. As a result,

AFM height measurement may be more accurate than width measurement by TEM. This assumption will be investigated in future experiments.

2.3.3 Test for personal bias in AFM image analysis

A variety of limitations exists in the measurement of CNC by AFM. CNC aggregation is difficult to avoid in samples prepared for microscopy and size measurements have to be restricted to only individual CNCs. However it is sometimes difficult to decide if a specific feature is due to one or several CNC particles. It is also difficult to completely standardize the AFM data analysis as different analysts may use slightly different criteria, even when given the same instructions. Therefore, an experiment was designed to test for possible effects of personal bias related to either CNC structure or AFM analysis procedures on the measured CNC size distribution.

This experiment was conducted by three assistants. Analyzer 1 is a summer student who only has limited knowledge of CNC and AFM. Analyzer 2 is a master student who has relatively more experience in AFM and CNC. AFM images were recorded by the other assistant (Dr. Maohui Chen) in 2013 by PicoSPM AFM (Molecular Imaging). Both of the two analyzers measured 300 particles from the same set of images, and each particle was labeled for comparison. Analysts were requested to analyze all individual CNCs in each image and to measure the CNC size by the method outlined in chapter 2.2.1. In this experiment, there are at least two sources of error: one is the selection of the single CNC for analysis, and the other is the variation/error in manual measurement of the length and height from the AFM images.

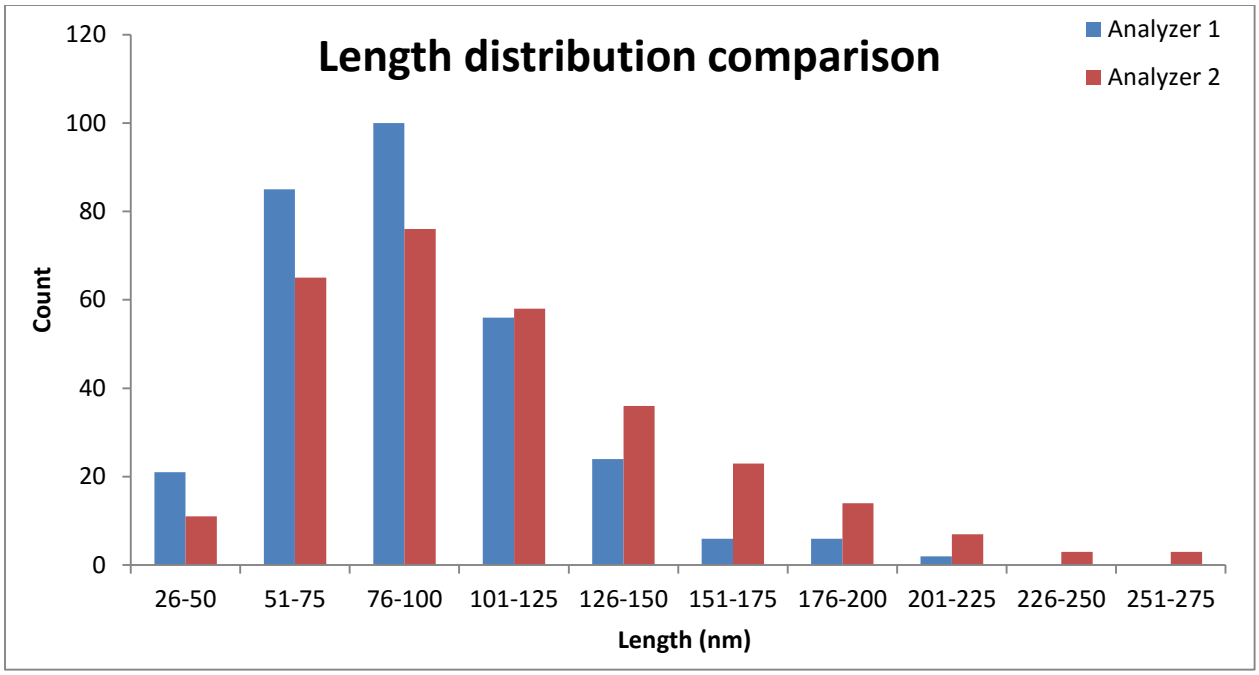

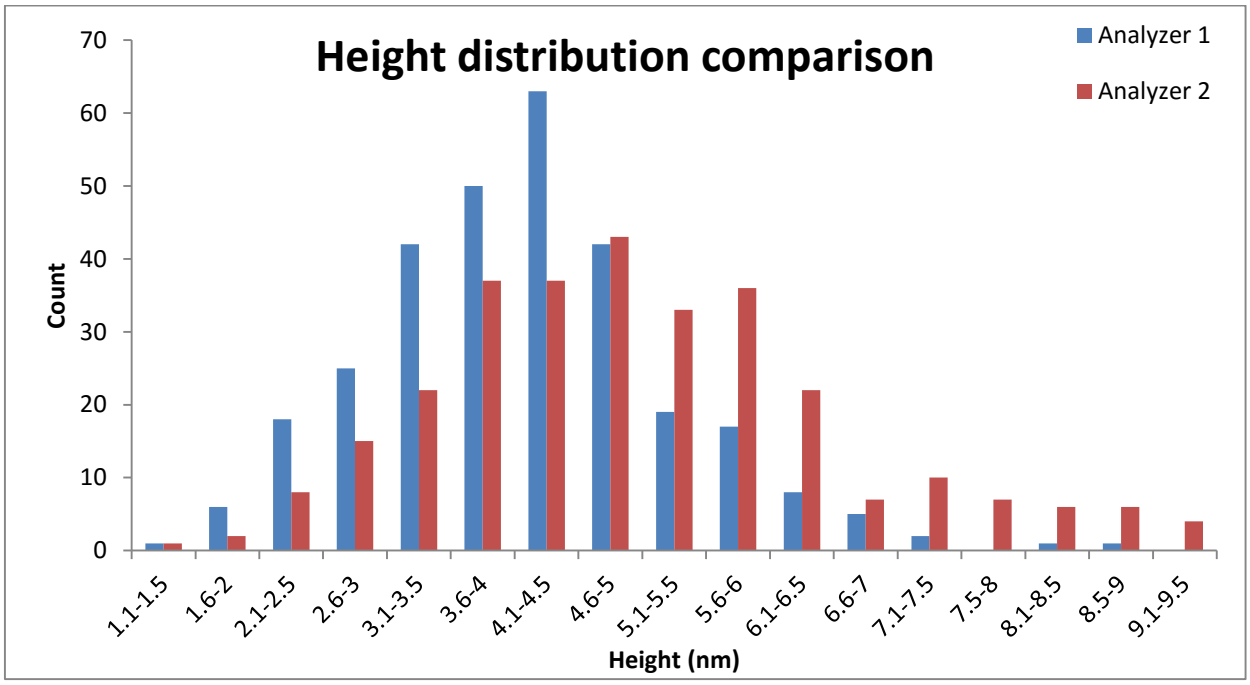

Figure 2-11: Comparison of histograms for the length distribution (top) and height distribution (bottom) as measured by two different analyzers.

The histograms obtained from this experiment are shown in Figure 2-11. The K-S test shows that both length and width distributions from the two analyzers are significantly different. To quantify the difference between analyzers, the Length/Height difference (D1) calculation formula is:

$$D1 = \frac{Ave.A1 - Ave.A2}{Ave.A2} \quad \text{(Equation 2-1)}$$

Based on the experiment, it is obvious that personal bias influenced the result (Table 2-5). The length average from analyzer 2 is 18.5 nm (20.3%) larger than analyzer 1's, and the height average is 0.8 nm (19.1%) higher than analyzer 1's. From the histogram comparison, a similar shift in the distribution was observed. This suggests that personal bias is selection of the analyzable particles or a systematic error in the manual measurement procedure can lead to apparently different particle size distributions from the same images.

Table 2-5: Comparison of results from different analyzers

Analyzer	Analyzer 1	Analyzer 2
Length (nm)	91.0±32.4	109.4±45.
Length difference (%)	20.3	
Height (nm)	4.2±1.2	5.0±1.7
Height difference (%)	19.1	

To test for differences in the manual measurement procedure, the 57 particles which were analyzed by both analyzer 1 and 2 were reconsidered. The result is shown in Table 2-6. The K-S test shows both length distributions of selected CNCs from two analyzers are not significantly different but height distribution are significant different. The Length/Height difference average (D2) calculation formula is:

$$D2 = \frac{\sum(L_{A1} - L_{A2})/L_{A2}}{n} \quad \text{(Equation 2-2)}$$

This difference average is able to describe the difference between the same particle measurements better (Table 2-6).

Table 2-6: Results when analyzer 1 and 2 choose the same CNC

Analyzer	Analyzer 1	Analyzer 2
Length (nm)	98.9±35.3	99.4±34.0
Length difference (%)	1.3	
Height (nm)	4.0±1.2	4.5±1.2
Height difference (%)	17.1	

The difference between length measurements is only 1.3%. This implies that both analyzers apply a consistent method for measuring the length. The length difference between the measurements by analyzer 1 and 2 was therefore caused by selection of different CNC particles for analysis. It is possible that analyzer 2 picks large CNC particles or analyzer 1 mistakes larger CNCs as "shoulder by shoulder" aggregates and therefore does not include them in the measurement. An example is shown in Figure 2-12. The difference in heights when the same particles are analyzed is 17.1% which is the same as the difference between the 300 particle averages. Both analyzers followed a rule which excludes obvious noise on the profile when measuring the height. Either the assessment of AFM image noise or the choice of background may have a strong influence on the result. In addition, from the histogram, analyzer 2 has higher counts in the 7 nm to 9.5 nm range compared to analyzer 1, which could be an effect of picking larger CNCs.

This experiment shows how much personal bias is capable of influencing quantitative size measurements. The best way to reduce the impact of personal bias is to analyze the images by

the one analyzer who has experience in AFM imaging and adequate knowledge of CNC structure. However, this will make it difficult to compare results between different laboratories.

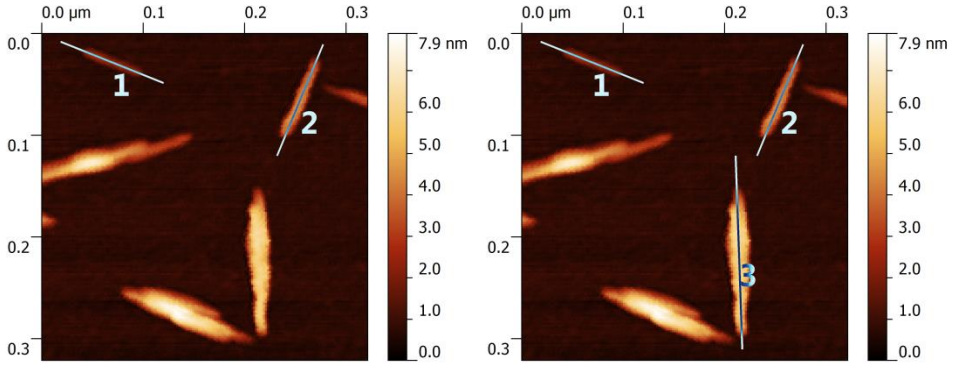

Figure 2-12: An example of the different selection of analyzed particles between analyzer 1 (Left) and 2 (Right). Analyzer 2 selected a large particle which is at least 2 CNCs in analyzer 1's opinion.

2.3.4 DLS measurements of never dried CNC samples

The size of two never-dried suspensions of CNCs was measured by DLS and the details are shown in Table 2-7. The data show that there is a large size disparity between CNC-Maine and CNCS-1(more than 20%). Furthermore, from the DLS intensity distribution (Figure 2-13) and PdI (Table 2-7), CNCS-1 clearly has a broader peak compared to CNC-Maine. This suggests that there are more large particles or aggregates in the CNCS-1 sample.

Table 2-7: DLS results of never dried CNC samples

DLS	Z-average (nm)	PdI	Z-potential (mV)
CNC-Maine	64.63±1.21	0.173±0.007	-48.5±13.7
CNCS-1	84.88±0.88	0.230±0.004	-57.1±18.7

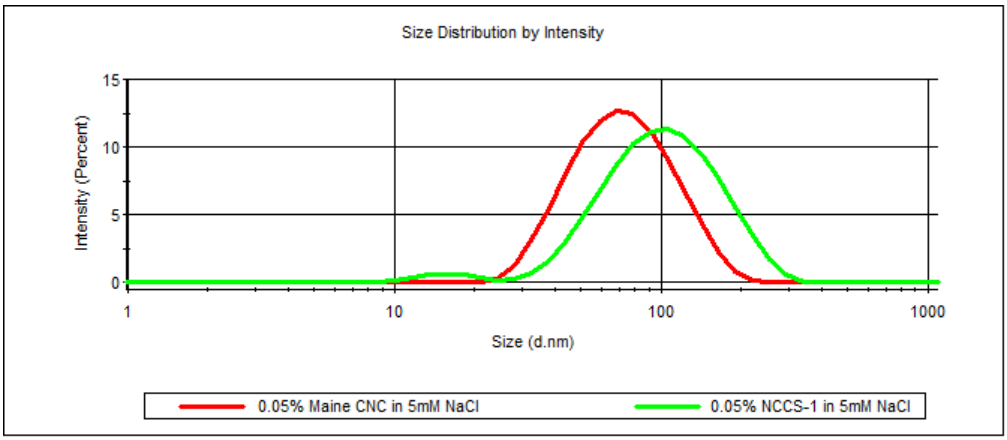

Figure 2-13: The DLS intensity distribution for two never-dried CNC suspensions. The green line is CNCS-1 and the red line is CNC-Maine.

Before comparing the AFM and DLS data it is important to consider the limitations of the methods. The DLS size distribution is intensity based and the microscopy size distribution is number based. Furthermore, the assumption of DLS is that all the particles are spherical[11]. DLS is good for interbatch comparisons particularly when the PdI of the sample low but cannot be directly correlated to the AFM results, as AFM enables the direct measurement of the particle length and height whereas DLS gives the Z-average for a sphere that would have the same light scattering intensity. DLS is an ensemble method and in AFM the sample set of particles used for measurement is small and may not be representative of the bulk sample.

Despite these considerations, the overall trends for the AFM and DLS data can be compared. The DLS results conflict with the AFM results (Table 2-3) which indicate that there is little difference in particle size between CNCS-1 and CNC-Maine. There is a possible explanation for the disagreement between the DLS and AFM results. For the DLS experiment, all samples were

filtered through a 0.45 μm PVDF filter. This will remove large aggregates while small aggregates of around 200-300 nm in length will remain in the suspension. These smaller aggregates will scatter more light than small particles and may shift the particle size distribution to a higher Z-average and increase the PDI. In AFM, since only individual CNCs were measured, CNCs that were part of aggregates were omitted from the size distribution. Also, the AFM sample is made from 0.001 wt. % suspension which is more dilute than the 0.05 % DLS sample. As such, it is possible that there may be fewer aggregates in the AFM sample because of dilution. These two CNC samples come from different manufacturers and may have different initial dispersions which will be assessed by DLS in chapter 2.3.6. The two samples have different surface potentials, CNCS-1 is more negatively charged than CNC-Maine. There could be a complex relationship between the state of aggregation and surface charge which could affect either measurement.

2.3.5 CNC Sonication effects as measured by DLS

Nine samples were prepared from the never-dried reference material CNCS-1 and fifteen samples were prepared from dry reference material CNC-2. All the samples were prepared and measured by DLS as described in chapter 2.2.6. Z-averages of the nine CNCS-1 samples are shown in Figure 2-14, top, and can be fitted by a single exponential function; those of the fifteen CNC-2 samples are presented in the lower part of Figure 2-14. By comparison, it can be observed that the z-average before sonication of CNC-2 (138 nm) is far higher than that of CNCS-1 (85 nm), but decreases rapidly when treated with low sonication energy. Z-averages of the two samples were almost the same when sonication energy reached about 2500 J/g. It is proposed that after being re-dispersed in water, CNC-2 particles form large but relatively fragile

aggregates through hydrogen bonding, which rapidly fragment upon ultrasonic treatment, leading to the rapid decrease in z-average. Stronger ultrasonic energy can break smaller aggregates, which exist in both CNC-2 and CNCS-1. Fits of the sonication data shown in Table 2-8 support this view; the data for CNC-2 can be fit to a double exponential function but a single exponential function provides the best fit for CNCS-1. Since t1 is large for both functions, this parameter has a significant impact on the fit. And because t1 values for the two fits are close, with only 60% difference, they would have little impact on the shape of the exponential functions. Since CNC-2 and CNCS-1 were produced by different manufacturers and from different raw materials, it is not surprising that they would have size differences. The extra exponential function for CNC-2, which represents the rapid decrease of z-average at low ultrasonic energy, has a t2 of 154, so it would show little effect on the trend line of the whole function when x exceeds 2500, at which the value of this part of function is only 3.21×10^4. Asymptotic values of the two functions differed by 5, which should be attributed to different sources of the two samples and different processing methods.

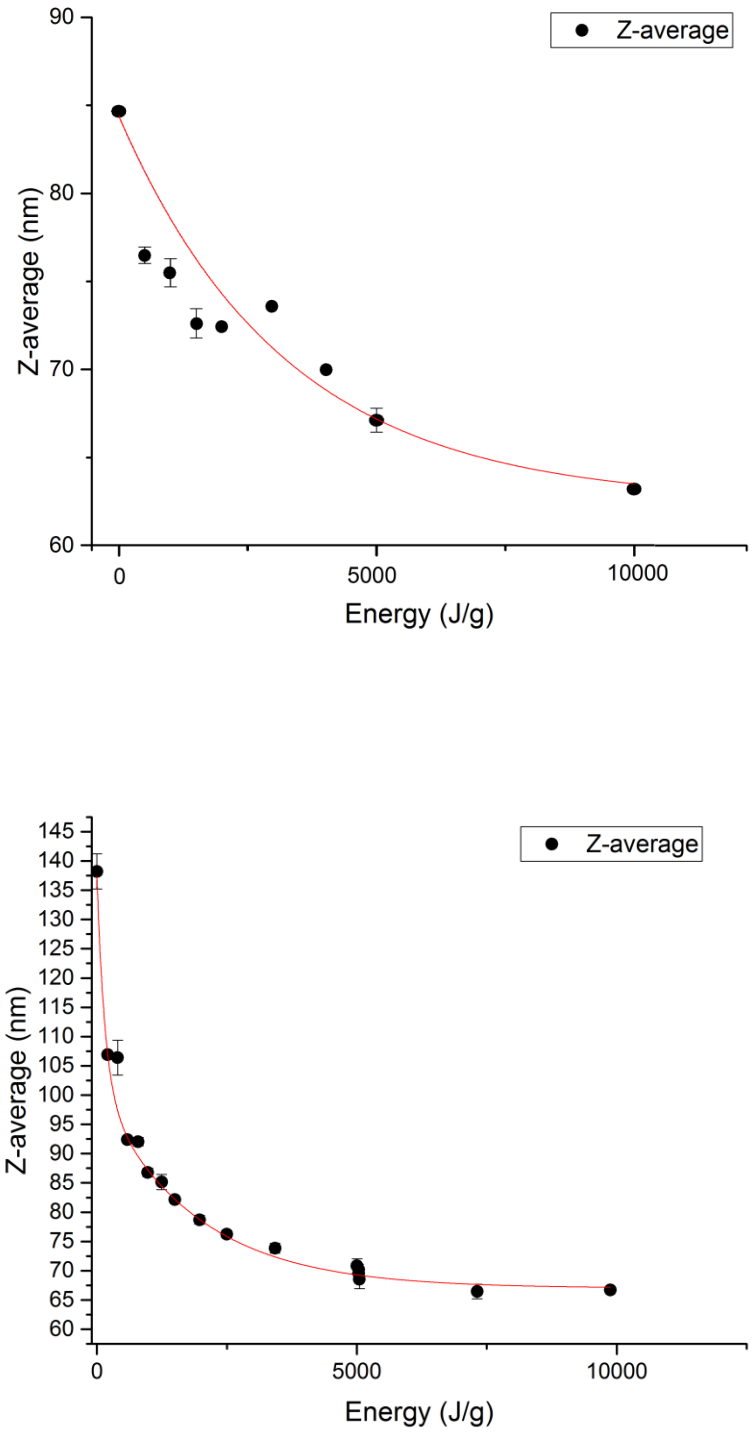

Figure 2-14: DLS results for CNCS-1 (top) and CNC-2 (bottom) for different sonication energies. The exponential fit is shown in red.

Table 2-8: The parameters obtained by fitting data in Figure 2-14 to single and double exponentials.

Equation	$y = A1*\exp(-x/t1) + A2*\exp(-x/t2) + y0$	
Samples	CNCS-1	CNC-2
y0	62.49	67.01
A1	21.86	34.27
t1	3.24×10^3	1.85×10^3
A2	N/A	36.11
t2	N/A	1.54×10^2
R^2	0.977	0.991

By comparisons above, we can see the difference between dried CNC and never-dried CNC when treated by ultrasound. Basically, never-dried CNC shows an extra process that may represent fragmentation of large aggregates. Although the mechanism of fragmentation of large aggregates is still not clear, it can be inferred from the data that large aggregates would generally be fragmented at relatively low sonication energy. Approximately 5000 J/g sonication energy is required for both samples to reach a plateau value where sonication has at most a minor effect on the size. Thus, 5000 J/g would be an appropriate energy for reproducible preparation of re-dispersed CNC suspensions.

Table 2-9: DLS results for re-dispersed CNC sonicated at 5000 J/g

	Z-average (nm)	**Peak (nm)**	**PDI**	**Zeta-potential (mV)**
CNC-1	68.44±0.14	82.78±0.21	0.172±0.007	-40.1±0.8
CNC-2	69.26±0.32	83.34±0.13	0.187±0.002	-39.7±1.5

Above we estimated that 5000 J/g is the optimal sonication energy for re-dispersion of CNC. Next DLS measurements were obtained for CNC-1 and CNC-2 suspensions prepared using the same re-dispersion method. From the data in Table 2-9 and Figure 2-15, it can be seen that DLS measurements for the two CNCs are very similar. They have very similar Z-average, peak position, Zeta-potential and PdI. Hence, we can say they basically have the same DLS performance and have the same surface charge.

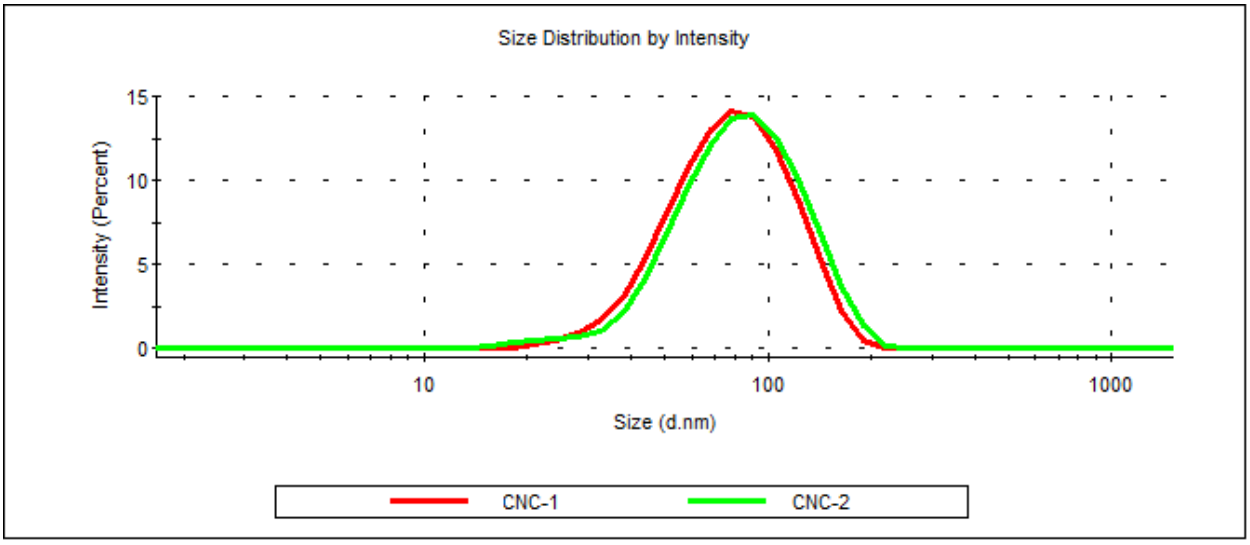

Figure 2-15: The DLS intensities for CNC-1 and CNC-2 re-dispersed with 5000 J/g sonication.

2.3.6 CNC-2 Homogeneity test

15 samples of CNC-2 were selected at random and re-dispersed to give 2 wt. % suspensions. The samples were diluted for DLS measurement. Right after the measurement of the CNC suspensions, a calibration of DLS was performed. The DLS calibration was run with ERM-FD304 certified reference material which has a known Z-average value of 41.64 nm. The result

of the calibration (Z-average of 42.1 ±0.6 nm) satisfactorily agrees with the certified value. Data were analyzed with standard Malvern software using the cumulants method and Z-average and polydispersity index were calculated. The data set normality was tested using Shapiro-Wilk test which concluded that at the level of significance higher than 0.05 the data was drawn from a normally distributed population (p-value of 0.20). Then, the data set was tested for outliers using a generalized extreme studentized deviate (ESD) test.

The details of all DLS result are shown in Table 2-10 and Figure 2-16. Points 13–15 were identified as possible outliers and the deviation was attributed to a change in CNC suspension ultrasonication conditions since the processing of samples number 1–12 and 13–15 were performed by different operators. To verify this hypothesis, the CNC suspensions were removed from storage, equilibrated to room temperature for 30 minutes, and DLS measurements were repeated in reverse order, from sample 15 to sample 1.

Table 2-10: Z-average and PdI values for 15 re-dispersed samples of CNC-2: (set a) samples measured in order from 1 to 15 and (set b) samples measured in the reverse order.

n	Z-average of set a (nm)	PdI of set a	Z-average of set b (nm)	PdI of set b
1	67.81±0.38	0.173±0.020	69.72±0.35	0.174±0.009
2	68.47±0.23	0.193±0.017	69.14±0.25	0.202±0.010
3	67.49±0.42	0.178±0.019	69.27±0.84	0.177±0.018
4	68.60±0.54	0.184±0.014	69.13±0.12	0.184±0.023
5	67.5±20.66	0.190±0.025	68.49±0.32	0.181±0.014
6	67.65±0.59	0.176±0.011	69.60±0.69	0.194±0.010
7	68.00±0.53	0.188±0.011	69.46±0.38	0.198±0.010
8	68.44±0.72	0.192±0.017	69.21±0.93	0.182±0.023
9	67.59±0.80	0.177±0.013	68.22±0.59	0.195±0.006
10	69.08±1.28	0.202±0.007	67.66±0.66	0.197±0.012
11	67.33±0.23	0.176±0.014	68.37±0.45	0.168±0.017
12	68.79±1.24	0.174±0.026	67.47±0.53	0.184±0.008

13	65.87±0.55	0.168±0.024	66.68±0.68	0.181±0.016
14	66.26±0.25	0.180±0.029	67.37±0.62	0.193±0.012
15	65.34±0.60	0.173±0.028	64.93±0.38	0.182±0.012

The second set of DLS measurements showed a similar trend (as a function of sample number) to the initial data set. The two sets were tested for correlation by the Pearson method and found to be correlated at the level of significance $\alpha = 0.05$ (p-value = 0.01). The data sets with point 13–15 removed showed no statistically significant correlation at $\alpha = 0.05$ (p-value = 0.24). Therefore, the difference in the DLS measurements is unlikely to come from a small systematic error in measurement for samples 13–15. Instead, the error likely originated the sample dispersion stage, most likely from differences in the sonication processes.

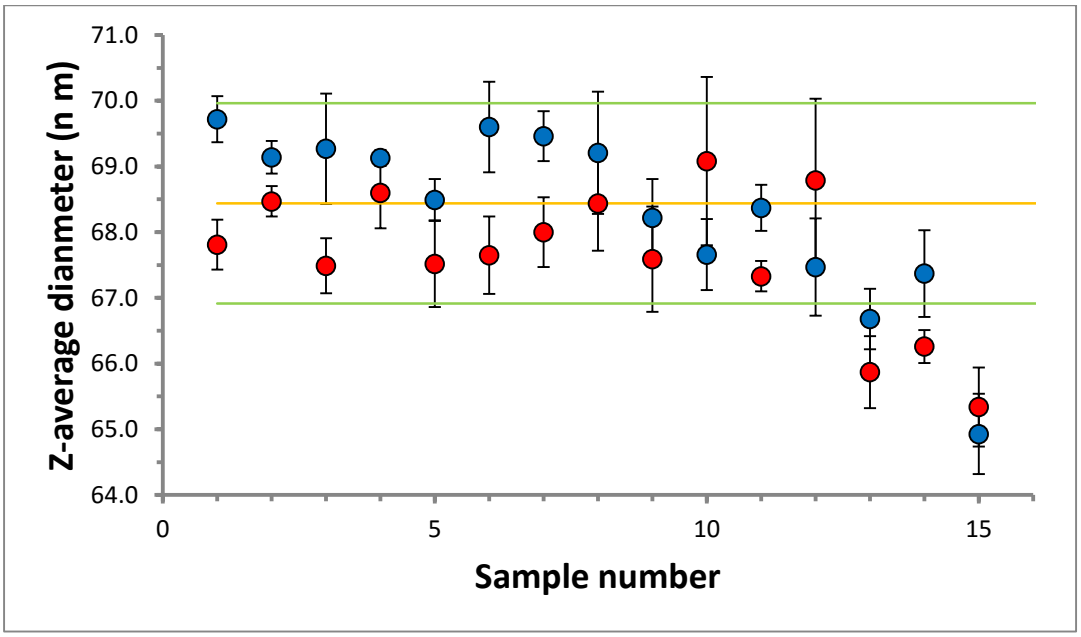

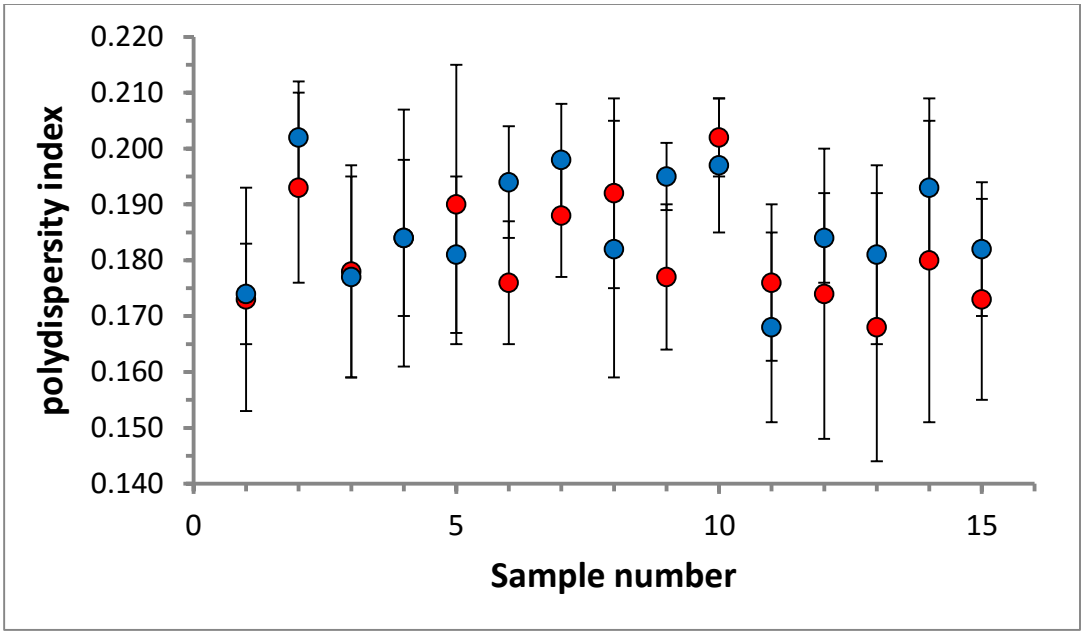

Figure 2-16: The Z-average (top) and PdI (bottom) of all samples (from Table 2-10, with set a in red and set b in blue). The average (yellow line) and standard deviation (green line) of the Z-average are shown in the top figure.

Since it was possible to identify a possible technical reason (different sample dispersion conditions) for the deviation of Z-average for points number 13–15, only measurements of samples 1–12 from the primary set (a) were used for the preliminary homogeneity evaluation (see Table 2, n=1–12; Figure 2-16, red circles). The evaluation was conducted by using ANOVA following ISO Guide 35[12]. Results of the analysis are shown in Table 2-11 below and confirm that the samples are homogeneous.

Table 2-11: Summary results for the homogeneity analysis.

	Z-average	PdI
Average	68.06 nm	0.184
Mean Square (total)	0.510 nm^2	2.91E-04

2.3.7 AFM for CNC-2 as a function of sonication time

Since the DLS results show a large change in Z-average as a function of sonication, AFM measurements were done for four CNC-2 samples prepared with three different sonication energies. Because 5000 J/g is the estimated best sonication energy, two samples were made using this energy and tested. The particle size analysis was performed as described in chapter 2.2.1 with approximately 300 CNC particles measured for each sample. Figure 2-17 shows typical AFM images of CNC treated with different ultrasonic energies. Under different ultrasonic energies, the distribution of CNC on the mica appears to be different. It can be seen from Figure 2-17 (a) that, when ultrasonic energy is zero, huge aggregates appear. These aggregates have an extremely loose structure, but contain a large number of CNC. In some other images of the same sample (Figure 2-17 b), the population of CNC is extremely low. However, quite a few aggregates still exist at this low density of CNC. For the sample sonicated with 1000 J/g (Figure 2-17 c), the huge aggregates disappeared and were replaced by small aggregates composed of about a dozen CNC. In the image with relatively few aggregates (Figure 2-17 d), individual CNCs are more commonly seen compared to the sample with 0 J/g sonication. When ultrasonic energy reaches 5000 J/g, aggregates are rare and are mostly composed of four or five CNC (Figure 2-17 e). In the image with relatively few aggregates (Figure 2-17 f), almost no change was detected in the ratio of individual CNC to aggregates, compared to the 1000 J/g sample. For this sample most images show a similar ratio of individual and aggregated CNC.

A parameter which can describe the aggregation degree in the AFM images is the individual CNC count number per image (Table 2-12). Because the initial CNC concentration is the same for all samples, we assume that if fewer particles are counted per image, then more particles must be part of CNC aggregates. It can be seen from the table that, along with the increase of

ultrasonic energy, the number of individual CNCs in each image increases accordingly and the counting rate is also more efficient. The AFM images at different ultrasonic energies also support the conclusions from the DLS study of sonication effects: very large, loose aggregations exist in the unsonicated turbid suspensions prepared from dry CNC, but they can be easily dispersed by ultrasound.

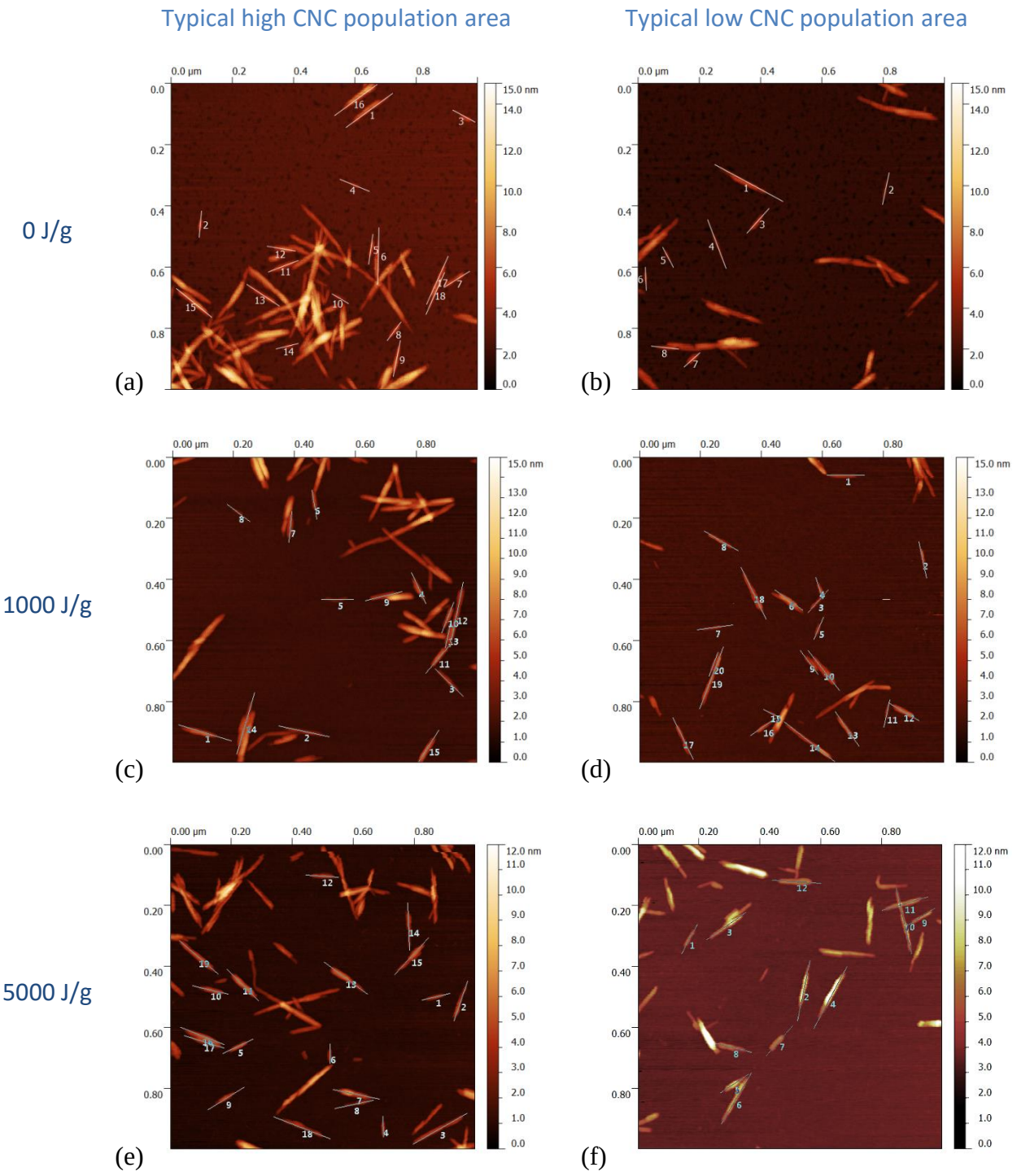

Figure 2-17: Typical images of high CNC population areas (right column) and low population areas (right column) for CNC-2 samples prepared with different sonication energies.

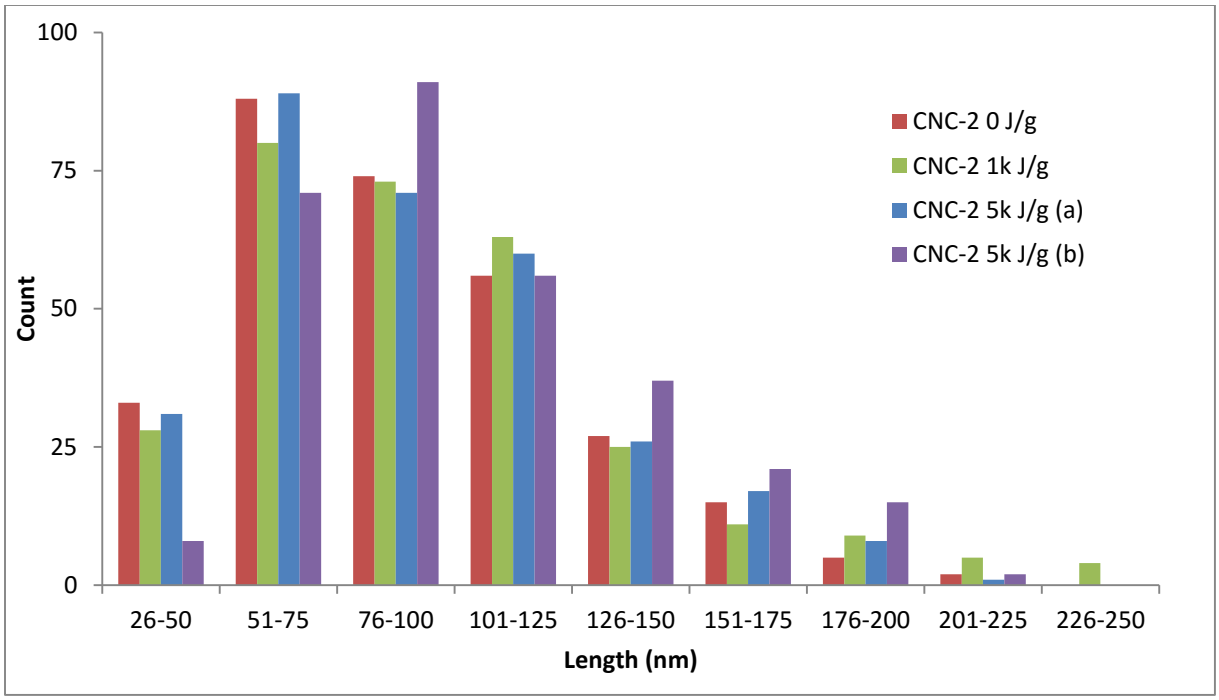
100
75
50
25
0
Count
CNC-2 0 J/g
CNC-2 1k J/g
CNC-2 5k J/g (a)
CNC-2 5k J/g (b)
26-50
51-75
76-100
101-125
126-150
151-175
176-200
201-225
226-250
Length (nm)

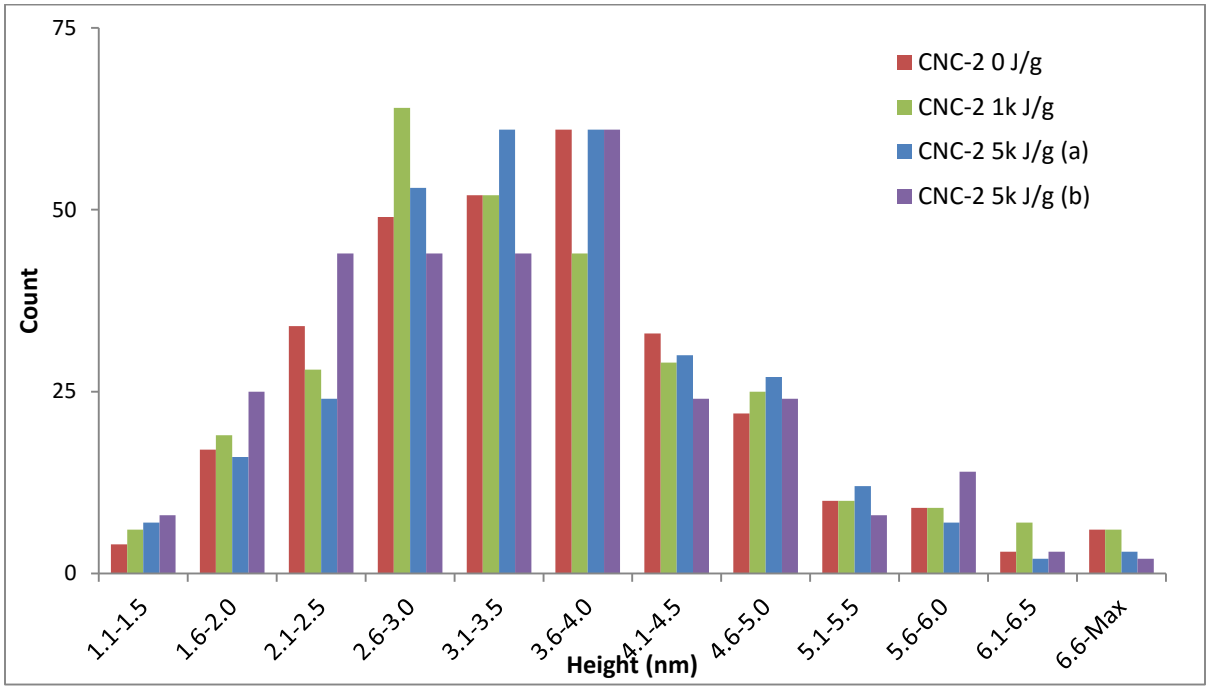
75
50
25
0
Count
CNC-2 0 J/g
CNC-2 1k J/g
CNC-2 5k J/g (a)
CNC-2 5k J/g (b)
1.1-1.5
1.6-2.0
2.1-2.5
2.6-3.0
3.1-3.5
3.6-4.0
4.1-4.5
4.6-5.0
5.1-5.5
5.6-6.0
6.1-6.5
6.6-Max
Height (nm)

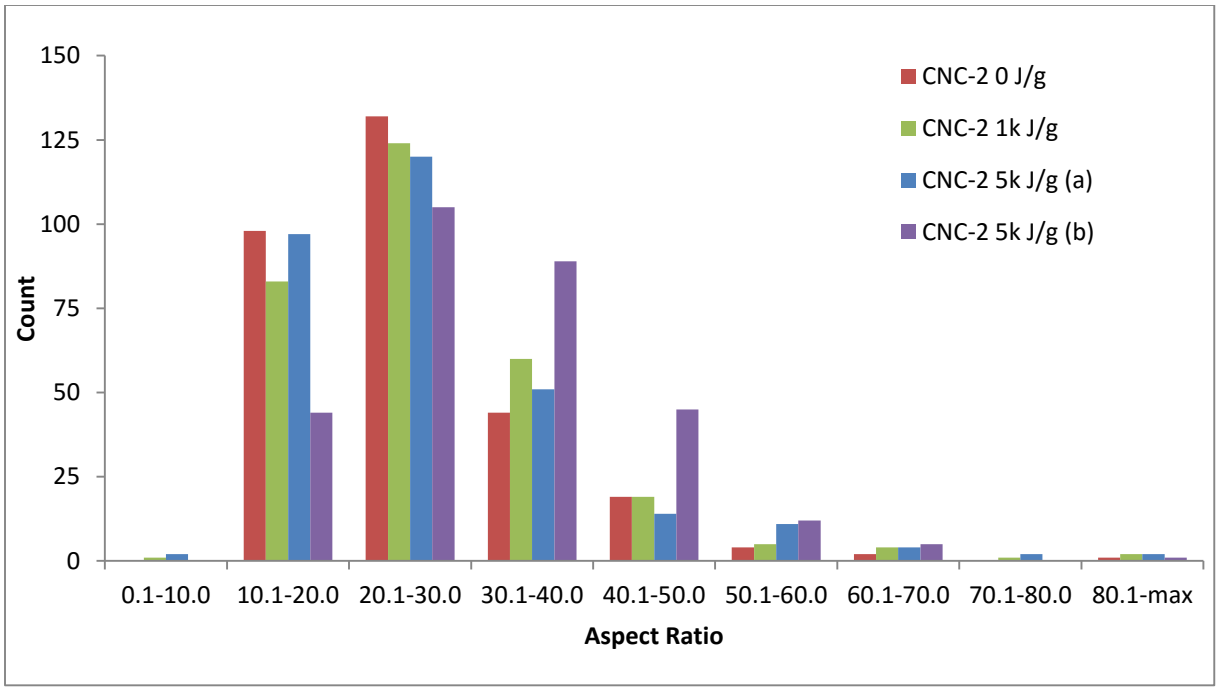

Figure 2-18: The length (top), height (middle), and aspect ratio (bottom) histogram for CNC-2 samples prepared with different sonication energies.

Table 2-12: Results of AFM analysis for CNC-2 samples prepared with different sonication energies.

	Length (nm)	Height (nm)	Aspect Ratio	CNC Count	CNC Count per image
CNC-2 0 J/g	90.42±35.42	3.65±1.15	25.72±9.91	300	9.1
CNC-2 1000 J/g	96.31±41.97	3.68±1.21	27.31±11.71	299	13.0
CNC-2 5000 J/g (a)	92.83±36.22	3.66±1.06	26.86±12.75	303	16.8
CNC-2 5000 J/g (b)	103.51±36.78	3.48±1.18	31.64±11.88	300	15.0

Histograms obtained for the four CNC-2 samples are shown in Figure 2-18 and the average length height and aspect ratios are summarized in Table 2-12. One of the CNC-2 samples with

5000 J/g (b) has an approximately 10 % difference in length from the other three samples. This difference is also observed in the length and aspect ratio histograms for this sample, which are slightly shifted from the others.

The average length and aspect ratio for each sample was tested using the K-S test (Figure 2-19). A significant difference was detected only between sample CNC-2 5000 J/g (b) and the other samples. However, the K-S test for height indicates no significant difference among all samples. Two conclusions can be drawn from this result: firstly, when AFM is used to measure CNC length, the degree of aggregation of the sample has little impact on the measurement result. Although one sample sonicated at 5000 J/g is different, the other three samples are similar to each other. Thus, when AFM is used to measure length of CNC, ultrasonic treatment will not exert too much impact on the results, unlike DLS which showed a significant difference between measurements without ultrasonic treatment and at 5000 J/g sonication. Secondly, individual selection bias or the state of the AFM tip may significantly affect the measurement result. Among the four samples, only one sample with 5000 J/g sonication showed an obvious difference in length and length-width ratio from the other samples, but no obvious difference in height. Although the analyzer is the same, individual bias may shift with time, so that longer CNC were more often chosen and measured by the analyzer. It is also possible that the AFM tip is aging and passivating during the scanning; the usage limit of a tip is judged by the experimenter based on image quality and may vary from one experiment to the next.

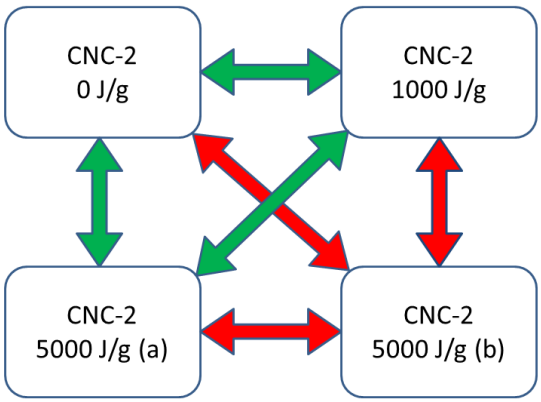

Figure 2-19: The results of K-S tests for the length and aspect ratio of CNC-2 samples dispersed with different sonication energies. Red arrows indicate that both lengths and aspect ratios are significantly different and green arrows indicate that length and aspect ratios are not significantly different.

2.4 Conclusion

In this chapter, the particle size distribution for several never-dried CNC samples was measured by AFM, TEM and DLS. For both AFM and TEM relatively large number of particles was analyzed in order to test for differences in the measured distributions for the two methods. The statistical K-S test was used to assess whether differences were large enough to conclude that the distributions were different. Although there were length differences between AFM and TEM, the difference is much smaller after consideration of the tip convolution effect. The width (TEM) and height (AFM) were significantly different. This may be related to the structure of CNC since some other studies have also observed that width is not equal to height.

The AFM data was also used to test for personal bias from the analyzer in the selection of suitable particles for analysis for the AFM measurements. This experiment demonstrated that

the selection of individual particles had a significant effect on the measured length, but less effect on the height. Because this error is based on the choice of individual CNC for analysis, the most effective method to reduce this error is to reduce the CNC aggregation. Since the aggregates may be formed in the suspension or when CNCs adsorb on the substrate, both sonication and spin coating should be tried in future experiments.

In comparing AFM and DLS for never-dried samples, DLS was able to detect differences between samples that were not observed in AFM. This indicates that small aggregates that were not removed by the filter used lead to a larger Z-average for DLS but do not affect the AFM results, since aggregates are excluded from size analysis. Tests of the effect of sonication indicated that the Z-average for never-dried samples decreased rapidly and then reached a plateau at approximately 5000 J/g. Thus, in the future, any quantitative measurement of CNC by DLS should be treated with 5000 J/g sonication energy to obtain a reproducible and easily repeatable sample.

The re-dispersion of dry CNC was examined in detail, especially the extent of sonication needed. Plots of Z-average against sample sonication show a clear two exponential fit, unlike the curves for never-dried suspensions. Test of homogeneity and reproducibility indicate that it is possible to reproducibly disperse the dry material and obtain reliable DLS data. The ability to obtain reproducible dispersions from dry material is an important step to be able to characterize samples and identify differences in particle size distribution and other properties.

Finally our results show that AFM and TEM provide comparable results when large data sets are used and the AFM tip convolution is taken into account. However, data analysis of mixtures of aggregates and individual particles is an issue that may cause the largest measurement error. The

presence of small aggregates has a relatively large effect on DLS, which will make it hard to use DLS as a substitute for the more time-consuming microscopy experiments for routine experiments.

2.5 References

1. Fraschini, C.; Chauve, G.; Le Berre, J.-F.; Ellis, S.; Methot, M.; O'Connor, B.; Bouchard, J., Critical discussion of light scattering and microscopy techniques for CNC particle sizing. *NORDIC PULP & PAPER RESEARCH JOURNAL* **2014,** *29* (1), 31-40.
2. (a) Habibi, Y.; Lucia, L. A.; Rojas, O. J., Cellulose nanocrystals: chemistry, self-assembly, and applications. *Chemical reviews* **2010,** *110* (6), 3479-3500; (b) Kimura, F.; Kimura, T.; Tamura, M.; Hirai, A.; Ikuno, M.; Horii, F., Magnetic alignment of the chiral nematic phase of a cellulose microfibril suspension. *Langmuir* **2005,** *21* (5), 2034-2037; (c) Beck-Candanedo, S.; Roman, M.; Gray, D. G., Effect of reaction conditions on the properties and behavior of wood cellulose nanocrystal suspensions. *Biomacromolecules* **2005,** *6* (2), 1048-1054.
3. Brown, S. C.; Boyko, V.; Meyers, G.; Voetz, M.; Wohlleben, W., Toward advancing nano-object count metrology: a best practice framework. *Envir. Health Perspectives* **2013,** *1221*, 1282-1291.
4. Beck, S.; Bouchard, J., Effect of storage conditions on cellulose nanocrystal stability. *TAPPI JOURNAL* **2014,** *13* (5), 53-61.
5. Terech, P.; Chazeau, L.; Cavaille, J., A small-angle scattering study of cellulose whiskers in aqueous suspensions. *Macromolecules* **1999,** *32* (6), 1872-1875.
6. Elazzouzi-Hafraoui, S.; Nishiyama, Y.; Putaux, J.-L.; Heux, L.; Dubreuil, F.; Rochas, C., The shape and size distribution of crystalline nanoparticles prepared by acid hydrolysis of native cellulose. *Biomacromolecules* **2007,** *9* (1), 57-65.
7. Beck, S.; Bouchard, J.; Berry, R., Dispersibility in water of dried nanocrystalline cellulose. *Biomacromolecules* **2012,** *13* (5), 1486-1494.
8. (a) Boluk, Y.; Danumah, C., Analysis of cellulose nanocrystal rod lengths by dynamic light scattering and electron microscopy. *Journal of nanoparticle research* **2014,** *16* (1), 1-7; (b) Eichhorn, S.; Dufresne, A.; Aranguren, M.; Marcovich, N.; Capadona, J.; Rowan, S.; Weder, C.; Thielemans, W.; Roman, M.; Renneckar, S., Review: current international research into cellulose nanofibres and nanocomposites. *Journal of Materials Science* **2010,** *45* (1), 1-33.
9. NT-MDT Effect of the tip curvature radius and cone angle. http://www.ntmdt.com/spm-basics/view/effect-tip-radius-cone-angle (accessed May 1st).

10. Kaushik, M.; Chen, W. C.; van de Ven, T. G.; Moores, A., An improved methodology for imaging cellulose nanocrystals by transmission electron microscopy. *NORDIC PULP & PAPER RESEARCH JOURNAL* **2014,** *29* (1), 77-+.

11. Instruments, M. Dynamic lighting scattering *An introduction in 30 minutes* [Online], p. 3-5.

12. Guide, I., 35: 2006. *Reference materials—General and statistical principles for certification* **2006**.

Chapter 3

Fluorescent cellulose nanocrystals

3.1 Introduction

Cellulose nanocrystals (CNC) are a nanomaterial which is currently of significant interest for a wide range of applications. This has led to increasing interest in methods to conjugate dyes, polymers and biomolecules onto cellulose nanocrystals[1] and cellulose-derived nanostructures for bio-imaging[2], material science[3], sensors[4], and other technological applications[5]. In the past few years, dye labeled CNCs have been prepared and used for different purposes. The 5-(4,6-dichlorotriazinyl) amino fluorescein (DTAF) labeled CNC was proposed as an optical marker for assessing the dispersion quality of CNC-polymer fibers by Abitbol et al[6]. A doubly labeled CNC containing Fluorescein isothiocyanate (FITC) and Rhodamine B isothiocyanate (RBITC) for ratiometric pH sensing was reported by Nielsen et al[4]. FITC labeled amino group modified CNC was suggested by Dong et al for drug delivery imaging[7]. Both Alexa labeled CNC[2] and RBITC labeled CNC[8] were synthesized for bio-imaging applications. In addition to CNC, a dye labeling approach was reported recently for studies of CNF distribution in composites[9]. These studies have covalently attached dyes to both sulfated and carboxylated CNCs and a wide range of dye loading levels (~32 μmol/g to ~2.1 μmol/g)[4, 10] have been reported. The dye loading has usually been assessed by UV-vis absorption and occasionally by fluorescence.

Applications of fluorescent CNCs have several challenges. One is the importance of understanding and optimizing the photochemical performance of the dye, including the dye loading[2]. A second is developing fluorescence methods to measure the distribution of CNCs in composite materials.

In this chapter, we examine the first challenge by measuring the photophysical parameters of dye labeled CNCs in more detail than has typically been used in other studies. Two dyes (RBITC and DTAF) that have been successfully used for bio-imaging[6] and pH sensors[4] were selected for

labelling CNCs. These dyes have the advantage of being cheap and readily available and compatible with relatively simple synthetic chemistry without first functionalizing the CNC surface, compared to some of the methods used in the literature. The photophysical properties of all dye labeled CNCs were studied in detail using UV-vis absorption and scattering and several fluorescence methods. The main goal was to determine the most appropriate labeling efficiency to maximize the ability to detect individual CNCs while minimizing the amount of dye used to avoid modifying the CNC properties. One of the dye-labelled CNC samples has been selected for a series of experiments to characterize the dye loading using single particle TIRF and correlated TIRF/AFM measurements. All of these methods have their advantages and disadvantages but the combined information gives a much better assessment of the performance of the dye-labeled CNC than the absorption method which is usually the only method used for dye loading characterization.

After characterizing the labeled CNCs, the second challenge was addressed by selecting the most suitable dye labeled CNC samples for development of a fluorescence microscopy method to characterize CNC distribution in CNC/polymer composites, as described in Chapter 4.

3.2 Experimental Procedures

3.2.1 5-(4, 6-dichlorotriazinyl) amino fluorescein (DTAF) labeled CNC

Never-dried 11.5 wt. % CNC suspension prepared from softwood pulp was purchased from the University of Maine Process Development Center. DTAF (Figure 3-1) was purchased from Sigma-Aldrich Inc. The CNC suspension was diluted to 1 wt. % and 4 wt. % with Milli-Q water (18.2 MΩ), as recommended by Abitbol for the reaction[6]. Solid NaOH and DTAF were added

directly to the appropriate volume of CNC suspension (50 mL of 1 wt. % and 50 mL of 4 wt. %) such that the mass ratio of CNC to DTAF was constant (1g CNC: 14 mg DTAF). The CNC was reacted with DTAF under alkaline conditions (0.2 M NaOH) for 24 h in the dark at room temperature with stirring.

The CNC products for the two reactions were isolated by centrifugation with Millipore 30K MW centrifuge filters using a 3175 g (4500 RPM), 90 minute cycle. The centrifuge used was the Hettich Universal 320R, which possesses a 140 mm radius 4-place swing-out rotor. After centrifugation, the filters were washed once with 0.1 M NaOH solution and the product was resuspended in Milli-Q water. Dialysis was performed against Milli-Q water using a Spectra/Por 4 12-14 kD dialysis membrane. The water was exchanged every 12 hours and the dialysis process was monitored by measuring the absorption of the dialysis water using the Cary 5000 UV/Vis spectrometer. The dialysis was stopped when the UV-Vis absorption of the water wash was less than 0.0005 at 490 nm, which required approximately 5 water exchange cycles.

Since the pH affects DTAF photophysics, the two suspensions were adjusted to pH 6.5 by sulfuric acid for long term storage. Finally, the dye-labeled CNC suspension was stored in the refrigerator at 4 ℃.

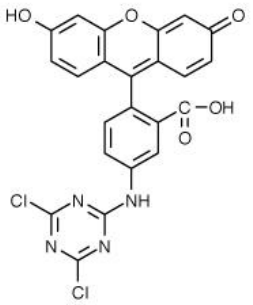

Figure 3-1: Structure of DTAF.

3.2.2 Rhodamine B isothiocyanate (RBITC) labeled CNC

A simple one-pot reaction for labeling microcrystalline cellulose by reaction of free hydroxyl groups with isothiocyanates to form the thiocarbamate bond has been reported[11]. This method for RBITC (Figure 3-2) labeling of CNC suspensions was also described by Nielsen et al [4] and is the method used here.

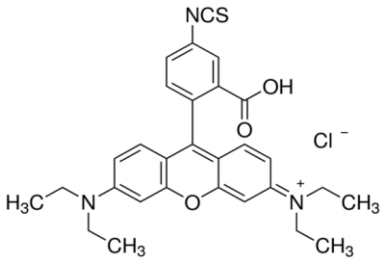

Figure 3-2: The structure of RBITC.

RBITC was bought from Sigma-Aldrich Inc. The never-dried CNC suspension (11.5 wt. %, University of Maine) was diluted to 1 wt. % with Milli-Q water (18.2 MΩ) and reacted with 0.1M NaOH and a specific amount of RBITC for several hours at room temperature in the dark with stirring. Three different reaction times and RBITC concentrations were tested to find the optimal conditions for dye-labeling (Table 3-1).

Table 3-1: RBITC concentration and reaction time of dye-labeled reaction

Sample name	CNC-RBITC-1	CNC-RBITC-2	CNC-RBITC-3
RBITC concentration	420 mg/L	45 mg/L	200 mg/L
Reaction time	96 hours	48 hours	72 hours
Sample volume	100 mL	100 mL	200 mL

The CNC suspension was isolated by centrifugation with a Millipore 30K MW centrifuge filter and then washed once with 0.1 M NaOH solution using the same filter. The CNC was

resuspended and dialysed against Milli-Q water using a Spectra/Por 4 12-14 kD dialysis membrane. The water was changed every 12 hours and the absorbance of the washed water was measured using a Cary 5000 UV-Vis spectrometer. The dialysis required 3-5 days to obtain UV-Vis absorption of the wash water of less than 0.0005 at 555 nm (10 mm path length quartz cell). Finally, the dye-labeled CNC suspension was stored in the refrigerator at 4 ℃.

3.2.3 UV-Vis absorption measurements

Absorption spectra were measured using a Cary 5000 UV-Vis-NIR spectrometer at room temperature with a 1 cm path length quartz cuvette. Before each measurement, the instrument was adjusted using Milli-Q water in a cuvette as a 100% transmission standard and a black rubber baffle as a 0% transmission standard.

For the scattering curve measurement, the dye labeled CNC stock suspension was diluted ten times with Milli-Q water and measured using a Cary 5000 spectrometer.

3.2.4 Fluorescence measurements

The photophysical properties of dye-labeled CNC were measured by a Horiba Jobin Yvon Fluorolog Tau 3 Spectrofluorometer with a photomultiplier tube detector (R928P, Hamamatsu Photonics). A free dye solution was measured for comparison with dye-labeled CNC. The dye-labeled CNC suspensions and dye reference solution were diluted until the maximum absorption was less than 0.1 in order to reduce the self-quenching and minimize uneven absorption across the cell. The spectra were corrected for variation of the excitation light-source intensity with excitation energy using a reference detector. For the lifetime measurements, the frequency-domain method was used. A 60 nm silica nanoparticle suspension was used as the scattering reference material. The same intensity (± 5 %) was used for both sample and reference. A

nonlinear least-square fitting program (Horiba Jobin Yvon Inc.) was used to analyze the raw-phase and modulation data in terms of single-exponential and double-exponential decays.

3.2.5 Total internal reflection fluorescence microscopy (TIRFM)

TIRF images were measured using an Olympus 1X81 microscope with a high resolution CCD camera (512 ×512 pixels, evolve, Photometrics) and an Olympus 150x Plan Apochromat objective (oil immersion, NA 1.45). The objective has 0.17 mm cover glass correction at 25 ℃ and was used with low florescence immersion oil (IMMOIL-F30CC Optics Low Autofluorescence Immersion Oil, Olympus Inc.). DTAF labeled CNC was excited by a 488 nm laser and emission was collected at 515-552 nm with a FITC filter. RBITC labeled CNC was excited by a 543 nm laser with emission collected at 570-616 nm with a Cy3 filter. A 543 nm quarter wavelength plate (Thorlabs, ½ inch) was used to give circularly polarized excitation for all the TIRF imaging experiments, except for the experiment where the effects of varying the polarization were examined. In this case a 532 nm half wavelength plate (Thorlabs, ½ inch) was used to give a linearly polarized excitation beam.

All the cover slides used for imaging were piranha treated. The piranha solution is a mixture of 98 % sulfuric acid and 30% hydrogen peroxide solution in 3:1 ratio. It can remove all organic residues from the coverslide and makes the slides highly hydrophilic. The Poly-L-lysine (PLL, 0.01 %) solution was incubated 30 minutes and washed with Milli-Q water. Then 50 µL of sample suspension was deposited on the PLL-coated cover slide, incubated for 1 minute and washed with Milli-Q water. All the Milli-Q water washing was done gently with a wash bottle. Lastly, the sample was blown dry with dry N_2 gas.

3.2.6 Atomic force microscopy

50 μL of 0.01M poly-L-lysine solution (PLL, Sigma-Aldrich, and Molecular Wt. 70000-150000) was deposited on a freshly cleaved mica surface and incubated for 30 minutes. Then, 50 μL of dilute dye labeled CNC suspension (1 million times dilution of CNC-RBITC-3) was deposited on PLL coated square mica (Ted Pella Inc. Hi-Grade Mica, Grade V2, 25 mm × 25 mm), and blown clean with dry N_2 gas.

Tapping mode (intermittent contact mode) AFM imaging was performed at room temperature in air using the JPK NanoWizard® II AFM. The tip used was the MikroMasch HQ: DEP-XCS-11 cantilever B which has a typical spring constant of 2.7 N/m, a resonance frequency of 80 kHz and is platinum coated.

The AFM images for dye labeled CNC were analyzed by Gwyddion as described in chapter 2.2.3. JPK SPM data processing software was used to analyze AFM data for the AFM-TIRF correlation experiments. Unlike Gwyddion, the JPK SPM data processing software can display the original scanning position accurately and overlap different AFM images easily, because it records the position and size of each image.

3.2.7 AFM-TIRF Correlation

The dye labeled CNC (CNC-RBITC-3) suspension was diluted with Milli-Q water one million times. The dye labeled bead (Molecular Probes, Eugene, Oregon USA, carboxylate-modified microsphere, 0.02 μm, Ex/Em is 535/575 nm) suspension was diluted with Milli-Q water ten thousand times. Both suspensions (50 μL each) were deposited on the piranha-cleaned and PLL coated cover slide at the same time. The sample was incubated for 1 minute, washed with Milli-Q water and blown dry with dry N_2 gas.

The correlation experiment was done using a JPK NanoWizard® II AFM and an Olympus 1X81 microscope with a 150x Plan Apochromat objective. The 543 nm laser was used to excite the dye labeled CNC and beads in TIRFM. The emission was collected at 570-616 nm with a Cy3 filter.

3.3 Results and discussion

3.3.1 5-(4, 6-dichlorotriazinyl) aminofluorescein (DTAF) labeled CNC

The one step dye labeling reaction described in the literature [6] was used to label CNC with fluorescein. The reagent, 5-(4, 6-dichlorotriazinyl) aminofluorescein (DTAF), reacts directly with the hydroxyl groups of cellulose[6]. The photophysical properties of the fluorescein labeled CNC were measured by absorption and fluorescence spectroscopy (Figure 3-3) using a diluted CNC sample at pH 8.5. DTAF (2 mg/L) in 0.4 mM NaOH solution was chosen as the free dye reference sample.

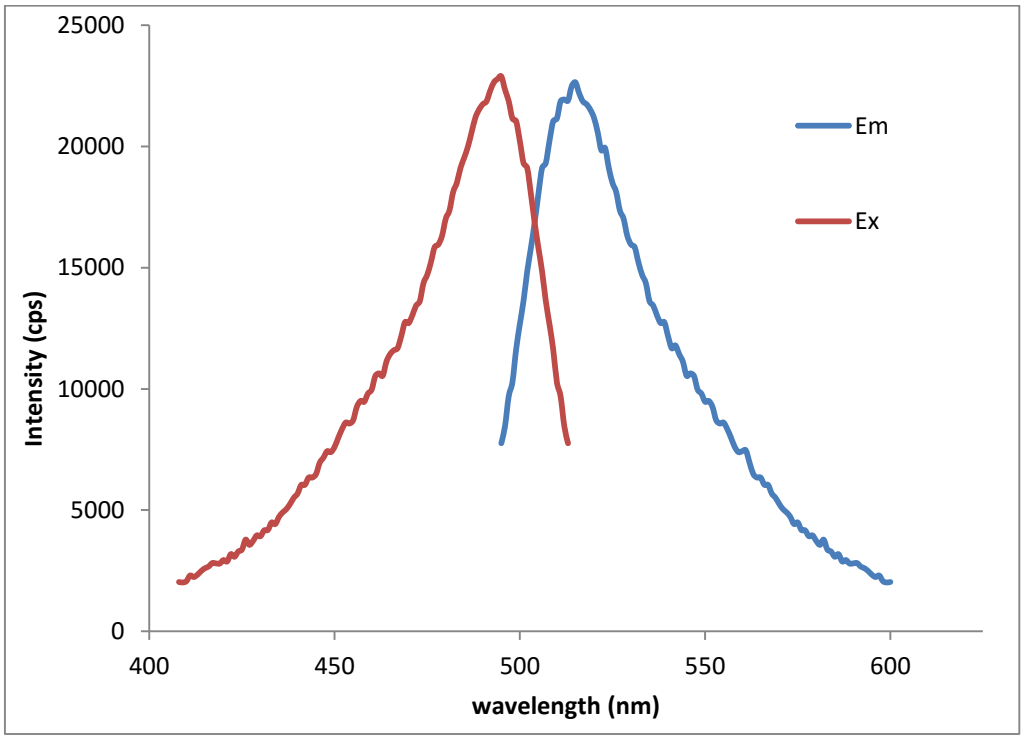

Figure 3-3: The excitation and emission spectra of DTAF labeled CNC (from 1 wt. % reaction) at pH 8.5 environment.

The fluorescence properties of the two CNC samples and the reference were measured using the Horiba Fluorolog Spectrofluorometer. Four parameters (max excitation wavelength, max emission wavelength, anisotropy, and lifetime) have been measured for each sample and the results are shown in Table 3-2. Both the maximum excitation and emission wavelengths show a small shift (2-4 nm) between free dye and dye labeled CNC, which may be due to a change of dye environment.The anisotropy of dye labeled CNC is more than 10 times higher than the anisotropy of the free dye. This is evidence that the dye molecule is attached to the surface of CNC and therefore has restricted rotational mobility. The lifetime was measured (Figure 3-4) and

Table 3-2: The maximum excitation wavelength, maximum emission wavelength, anisotropy, and lifetime of DTAF samples. The lifetimes were fit to a double exponential for DTAF-CNC with the number in parenthesis the fraction decaying with that lifetime.

Sample Name	Max Excitation wavelength (nm)	Max Emission wavelength (nm)	Anisotropy	Lifetime (ns)
DTAF reference	490	513	~0.017	2.539
DTAF-CNC made from 1 wt.% suspension	492	515	~0.190	①3.809 (57.8%) ②1.289 (42.2%)
DTAF-CNC made from 4 wt.% suspension	494	517	~0.200	①4.038 (56.9%) ②1.278 (43.1%)

the data were tested for fitting to both single and double exponentials. The best fit (lowest χ^2) was obtained for a double exponential for both CNC samples. This is consistent with a change of environment and possibly also with two distinct environments for the dye on the CNC surface. The photophysical results indicate that the 4 wt. % and 1 wt. % dye reactions gave labeled CNC with similar performance.

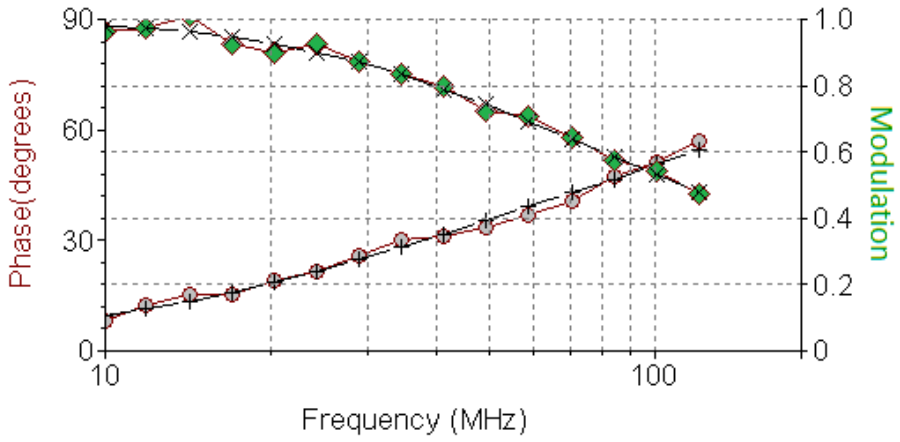

Figure 3-4: Lifetime measurement and fitting for DTAF labeled CNC. The phase angle is displayed with grey dots and the modulation with the green rhombus. The best fits to a double exponential decay are shown in black lines.

The photophysical behavior of DTAF-CNC is complicated by the pH-sensitivity of fluorescein which has been described in many references[12]. Thus, an experiment to measure the change in the emission of DTAF-CNC with pH is shown in Figure 3-5. This complex dependence on pH is not ideal for use of the dye-labeled CNC for characterization of CNC-polymer composites, for

which it will be difficult to control the pH. Therefore, despite the ease of synthesis of DTAF, it was decided to investigate labeling of CNC with a different dye.

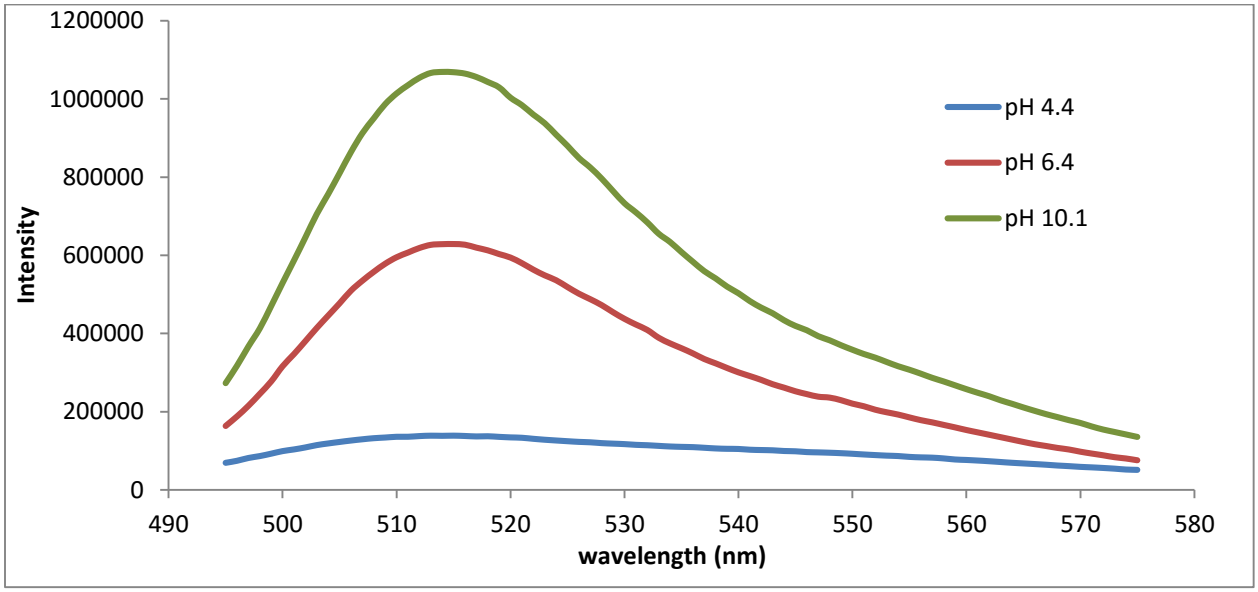

Figure 3-5: The DTAF-CNC emission spectra at different pH. DTAF has higher fluorescence intensity in a basic environment.

3.3.2 Rhodamine B isothiocyanate (RBITC) labeled CNC

A one step reaction has been used to label CNC with RBITC, as shown in Figure 3-6. The RBITC reacts with the hydroxyl group to form a thiocarbamate bond to the CNC surface in basic solution.

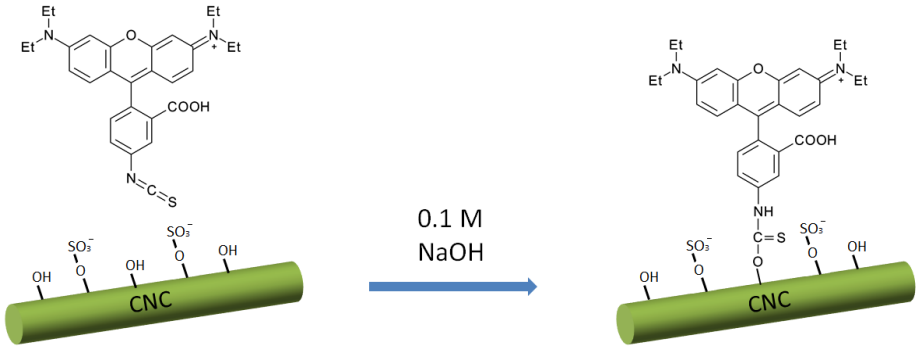

Figure 3-6: The RBITC reaction scheme.

Three different recipes have been tried as shown in Table 3-1. Each CNC sample was characterized by UV-vis absorption and fluorescence spectroscopy. The absorption spectra (Figure 3-7) show two peaks, one at 560 nm due to monomeric RBITC and a weaker peak at 530 nm due to a dimer. The dimer of Rhodamine B (RB) with a strong absorption peak at 530 nm has been described previously in the literature[13] and is formed from two monomers by hydrogen bonding or covalent bonding. The dimer of RB does not behave like dimers of the acridine dyes or eosins[13a]. It not only emits phosphorescence but also has low fluorescence intensity. The RBITC dimer absorption is observed as a small shoulder for the free dye solution. For dye labeled CNC, the dimer shoulder becomes higher, indicating an increase in dimer concentration when RBITC is attached to CNC. CNC-RBITC-2 which has the lowest initial dye concentration has the smallest dimer peak indicating that dimer formation increases with increases in the dye concentration.

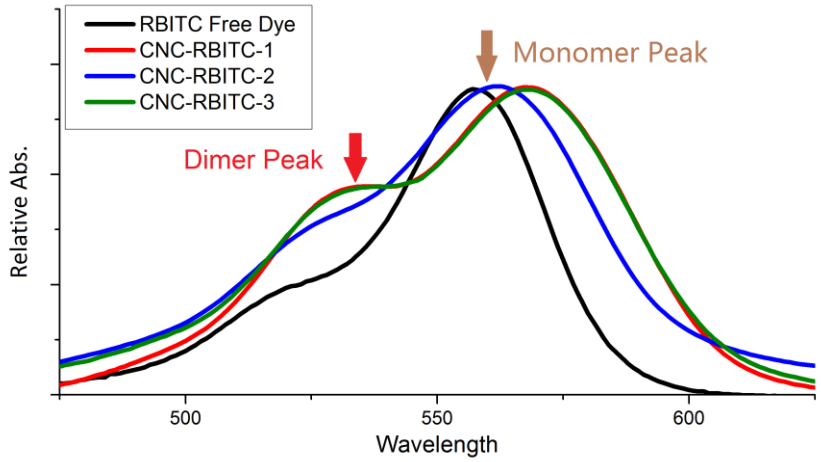

Figure 3-7: The absorption spectra of RBITC and RBITC-CNC samples. The sample absorptions are normalized. The Dimer peak and monomer peak have been labeled.

Table 3-3: Absorption wavelength, excitation wavelength, emission wavelength, fluorescence anisotropy, and lifetime and pH measurement for RBITC and RBITC-CNC samples.

Sample name	RBITC	RBITC-CNC-1	RBITC-CNC-2	RBITC-CNC-3
Max Absorption wavelength (nm)	557	559	560	564
Max Excitation wavelength (nm)	557	558	560	564
Max Emission wavelength (nm)	580	583	584	585
pH	4.9	5.3	5.5	5.4
Anisotropy	0.06	0.18	0.36	0.29
Lifetime (ns)	1.174	2.352	2.515	2.185

The photophysical parameters (max excitation wavelength, max emission wavelength, anisotropy, and lifetime) for each sample are shown in Table 3-3. The anisotropy of dye labeled CNC is more than 10 times higher than the anisotropy of the free dye. This is evidence that the

dye molecule is attached to the surface of CNC and therefore has restricted rotational mobility. The lifetime of RBITC labeled CNC has the best fit (lowest χ^2) to a single exponential, and is approximately twice as large as the free dye, which also suggests that the dye is covalently attached to the CNC.

The fluorescence excitation and emission spectra of CNC-RBITC-3 are shown in Figure 3-8. Although two absorption peaks at 530 nm and 564 nm are clearly shown in the absorption spectrum in Figure 3-7, the fluorescence excitation spectrum shows a single fluorescence excitation peak at 560 nm (Figure 3-8) with a very small shoulder near 530. This demonstrates that the dimer has weak emission, as described previously by Kajiwara et al [13a]. The 530-nm shoulder in the absorption spectrum was also reported previously for RBITC labeled CNC[10].

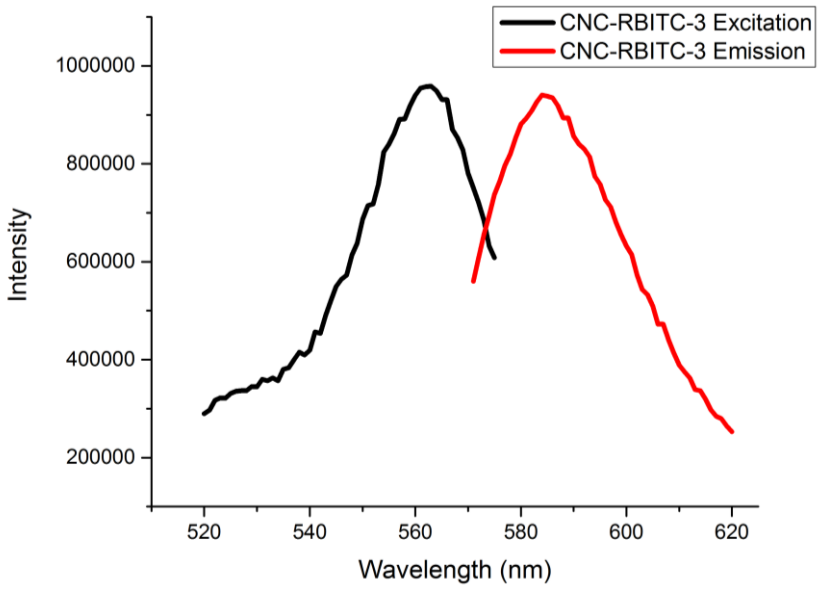

Figure 3-8: The excitation and emission spectra of CNC-RBITC-3. The spectra have been normalized. The excitation spectrum has a very weak shoulder at approximately 530 nm.

3.3.3 Scattering to estimate the CNC concentration

Scattering was used to estimate the concentration of the CNC-RBITC suspensions. This relies on fitting the scattering curve to the Mie-scattering theory which describes nanoparticle light scattering. The following fitting equation was used[14]:

$$I = a + \frac{b}{(\lambda - \lambda_0)^4} \qquad \text{(Equation 3-1)}$$

$$b \propto c$$

In this equation, parameter I is the absorption, parameter a and λ_0 are constants, parameter b is proportional to the concentration c and λ is the wavelength of the incident light. The absorption spectra for CNC samples were measured with a Cary 5000 UV-Vis-NIR spectrophotometer. Figure 3-9 shows an example of an experimental scattering curve and the fitting curve obtained using equation 3-1. In this figure, the difference between the experimental and calculated curves is 0.015 abs in the range between 250 nm and 800 nm. Only scattering data between 250 – 800 nm were used in the following experiments because the CNC absorption is much higher than the scattering beyond 250 nm. Thus, the convolution between absorption and scattering is more complex than described by equation 3-1. For the dye labeled CNC, because the dye has absorption between 450 nm to 650 nm, the fit in this range is ignored.

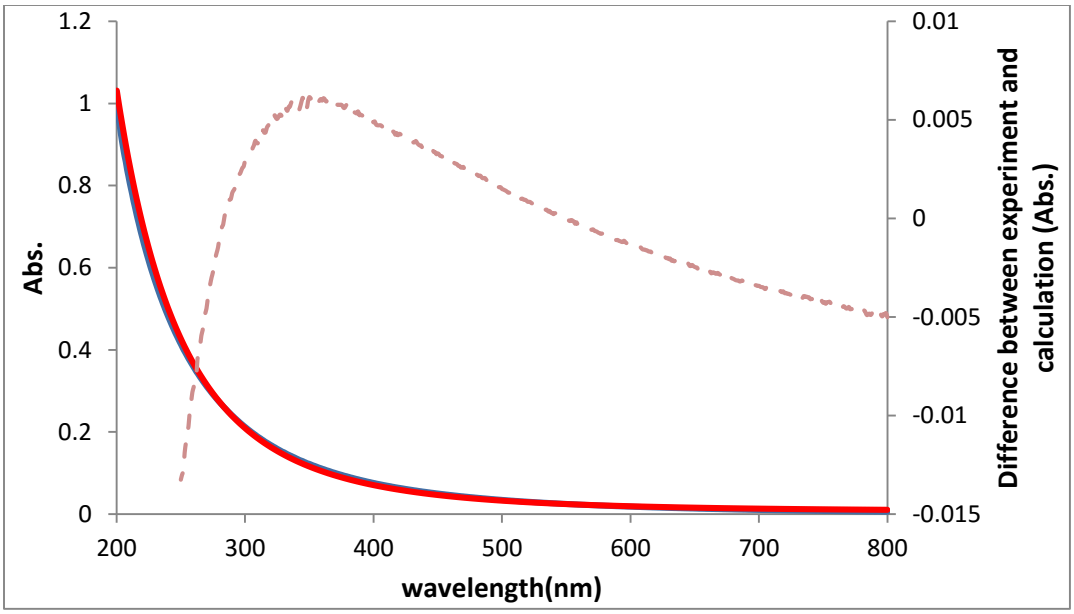

Figure 3-9: The experimental scattering curve (solid red line) measured using a UV-Vis spectrometer and the fitted scattering curve (solid blue line) for CNC-Maine suspension (0.5 wt. %, no labeled). The difference between experiment and calculation (dotted red line) is displayed on the right y axis.

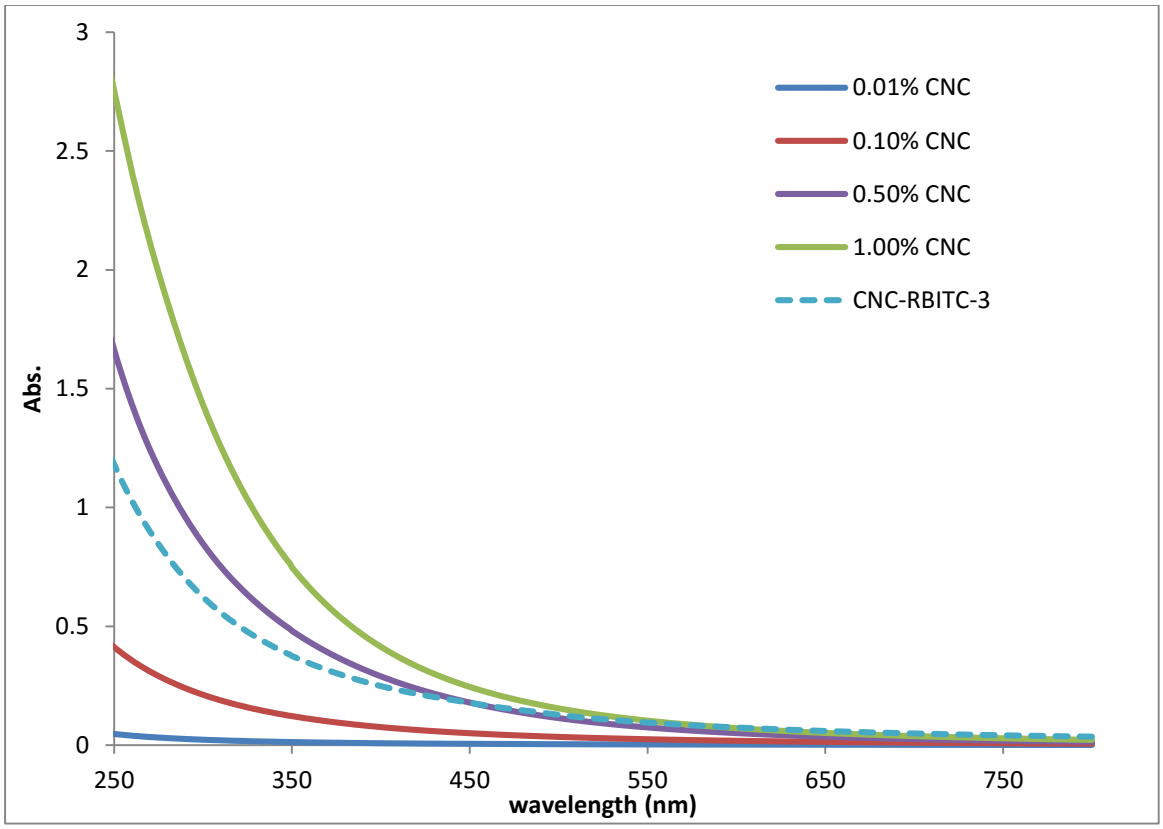

Figure 3-10: The different CNC suspension scattering curves measured by UV-Vis absorption. Solid lines are the standard CNC suspensions and the dotted line is the diluted dye labeled CNC suspension. The CNC-RBITC curve is shifted in the range of 400 -650 nm because of dye absorption.

Four CNC-Maine suspensions with known concentrations were used as standards to calibrate this method. The scattering curves for the standards and CNC-RBITC-3 are shown in Figure 3-10. Because the dye labeled CNC has more than 1 wt. % concentration which gives high scattering in the UV range, the RBITC-CNC samples were diluted ten times. The curve for RBITC-CNC shows increased signal between 400-650 nm due to the dye absorption. All the experimental curves were fitted by equation 3-1 to calculate the b value. The b value vs. concentration plot for the standard solutions is shown in Figure 3-11 (blue triangles) along with a quadratic curve fit of the data with R^2 =0.9995. The fitting curve is quadratic because of self-absorption and multiple

scattering. That may not be obvious for low concentrations of particles but is clear for high concentrations of CNC. The red circle in Figure 3-11 is the b value for the ten times diluted CNC-RBITC-3 suspension which gives a CNC concentration of 0.147 wt. % from the fitting curve.

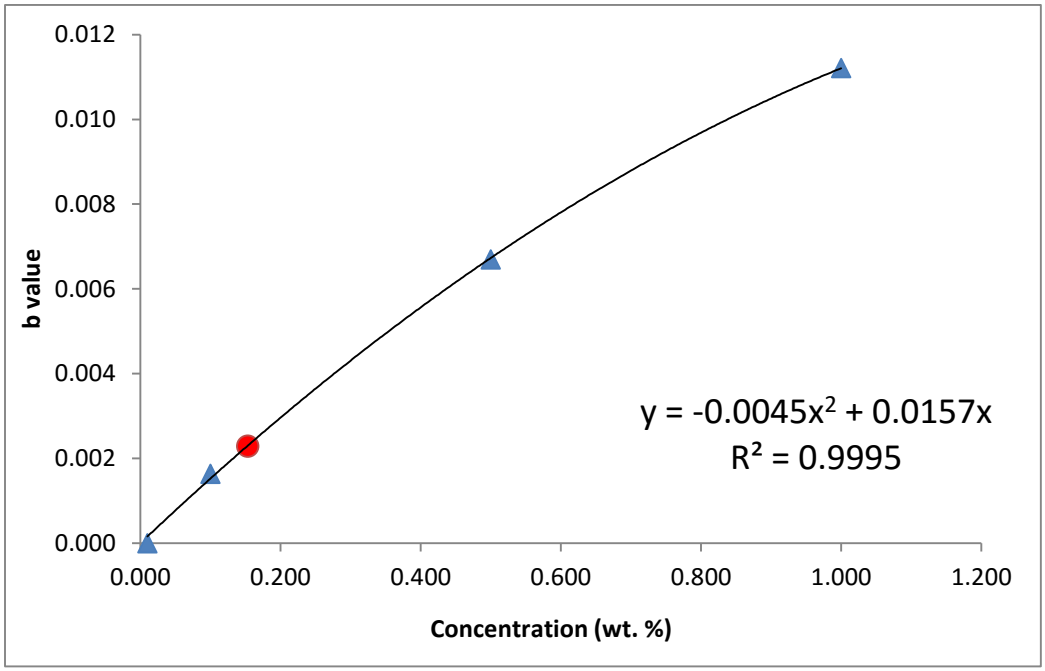

Figure 3-11: The b values calculated by fitting the standard CNC suspension scattering curves (blue triangles) as a function of CNC concentration and the fitting curve of b (solid line). The equation for the fitted line is shown in the graph. The b value for ten times diluted CNC-RBITC-3 (red circle) is used to obtain the concentration of this sample.

The CNC concentrations of all the RBITC labeled samples were calculated by the above mentioned method and are listed in Table 3-4. The measured concentration is higher than the initial reaction concentration (1 wt. %) for some samples because the dye labeled CNC was isolated by centrifugation and then re-dispersed in a new solution.

Table 3-4: The concentration of the dye labeled CNC stock suspensions.

Sample Name	CNC-RBITC-1	CNC-RBITC-2	CNC-RBITC-3
Concentration (wt. %)	1.00	0.78	1.47

3.3.4 RBITC dye loading efficiency

Two methods were used to estimate the dye loading efficiency. One uses the extinction coefficient (ε) of RBITC in solution to determine the dye concentration for CNC suspensions, with the assumption that the extinction coefficient is not altered by conjugation of the dye to the CNC. The experimental extinction coefficient was measured from four different known concentrations RBITC solutions. Using the maximum absorption of those four RBITC solutions, an average extinction coefficient of 82519 $cm^{-1}M^{-1}$ was calculated, which can be compared to a literature value of 103000 $cm^{-1}M^{-1}$.[15] The overlap of the dimer peak with the monomer peak was not taken into account, which will introduce some error in this measurement.

The second method uses the quantitative fluorescence emission at 584 nm to compare free dye (of known concentration) and CNC-RBITC. This method assumes that the fluorescence quantum yield of the dye does not change after attachment to CNC. However the lifetime of the dye does change after attachment to the CNC, which may result in a change in quantum yield. Thus, the quantum yield assumption may introduce error in the dye loading calculation.

After obtaining the dye concentration in μmol per gram CNC (Table 3-5, top), the number of dye molecules per CNC particle can be estimated based on the AFM size measurement of CNC-Maine. In this calculation, CNC has been assumed to be a perfect cylinder with 96 nm length and 4 nm diameter (average size data from chapter 2). The density of 1.6 g/cm^3 from reference [16] and the volume/CNC particle were then used to calculate the number of particles for suspensions with a known wt. % CNC. The results of this calculation are shown in Table 3-5, bottom.

Table 3-5: The dye concentration for three different CNC-RBITC samples expressed as micromole per gram CNC (top) and dye molecules per CNC particle (bottom).

Sample Name	Absorption method (experimental ε)	Absorption method (literature ε)[15]	Fluorescence comparison method
CNC-RBITC-1	1.57 μmol/g	1.26 μmol/g	0.81 μmol/g
CNC-RBITC-2	0.21 μmol/g	0.17 μmol/g	0.22 μmol/g
CNC-RBITC-3	0.98 μmol/g	0.78 μmol/g	0.73 μmol/g

Sample name	Absorption method (experimental ε)	Absorption method (literature ε)[15]	Fluorescence comparison method
CNC-RBITC-1	1.74 molecule/CNC	1.40 molecule/CNC	0.90 molecule/CNC
CNC-RBITC-2	0.23 molecule/CNC	0.19 molecule/CNC	0.24 molecule/CNC
CNC-RBITC-3	1.07 molecule/CNC	0.86 molecule/CNC	0.80 molecule/CNC

The results show that CNC-RBITC-1 has the highest dye loading, and CNC-RBITC-2 has the lowest dye loading. For CNC-RBITC-2 which has the lowest dye loading there is good agreement between absorption and fluorescence methods. This is not the case for CNC-RBITC-1 and 3. CNC-RBITC-1 has the highest dye loading but the largest gap between the concentrations from absorption and fluorescence methods. From the absorption spectra in Figure 3-5, CNC-RBITC-2 has the lowest dimer peak, and CNC-RBITC-1 has the highest dimer peak. The presence of a larger amount of dimer will give a larger error in the absorption measurement. The CNC-RBITC-3 has a dye loading between the other two samples, and the difference between the two methods is smaller. Since dimer alone does not seem adequate to explain the

variation between methods, another possibility is that the dimer may quench monomer fluorescence[13b]. Furthermore, literature studies also suggest that there may be multiple types of dimer and possibly also oligomers for RB in some organized environments.[13b]

CNC-RBITC-2 has the lowest dye loading of ~ 0.2 molecules per particle, which is not ideal for single particle fluorescence or for characterizing the CNC distribution. CNC-RBITC-3 has the largest dimer contribution and its fluorescence yield is similar to CNC-RBITC. Since CNC-RBITC-3 has a labeling ratio of about 0.8 dyes per CNC particle and has less dimer than CNC-RBITC-1 but a similar fluorescence yield, it was used for the following experiments.

3.3.5 TIRFM experiment to measure the dye linked CNC

TIRFM was used to study the dye labeled CNC (CNC-RBITC-3). An overview of the theory behind TIRFM was presented in chapter 1. TIRFM was favoured over other fluorescence microscopy methods for studying dye-labeled particles due to its high signal-to-noise ratio. Typical TIRF dye labeled CNC images are shown in Figure 3-12 for a sample diluted 10,000 times. This sample has a number of large bright spots that are due to CNC aggregates as well as less bright spots that may be single CNCs. The density of spots and the presence of aggregates mean that this sample is too concentrated for single particle fluorescence studies.

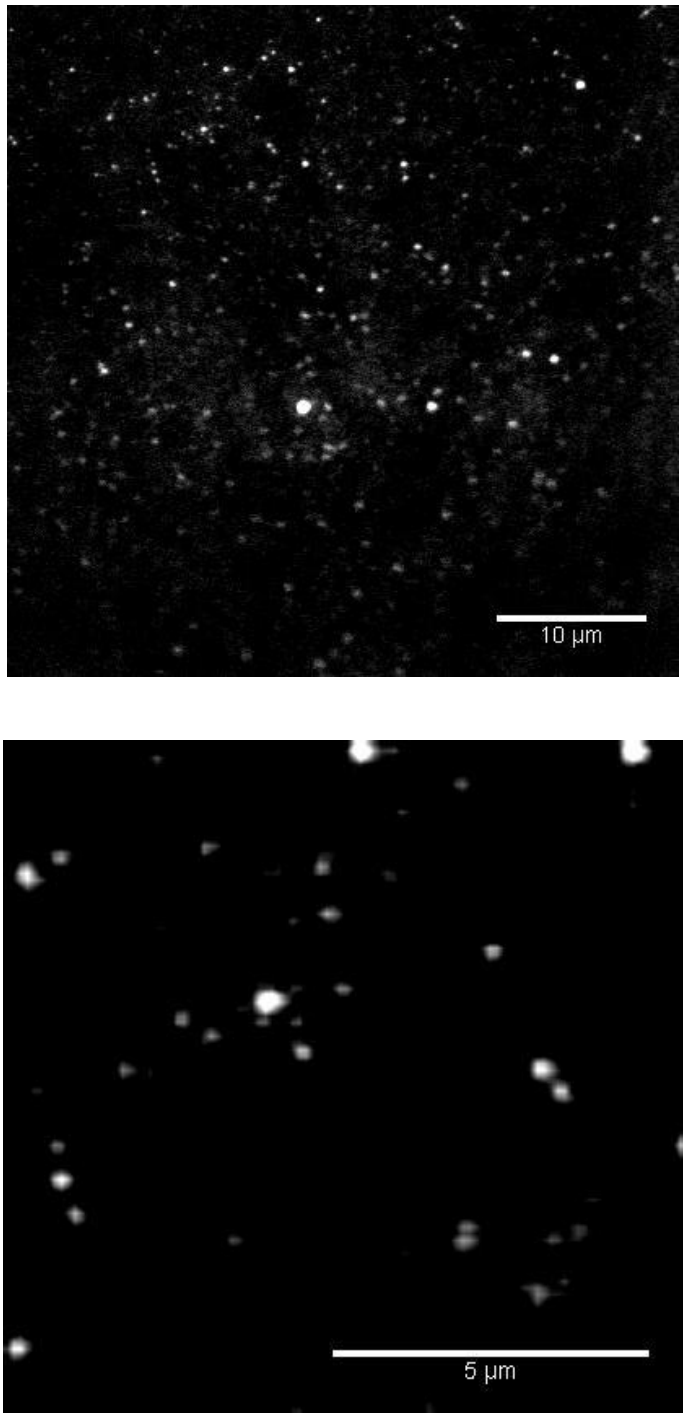

Figure 3-12: An example of a TIRFM image for CNC-RBITC-3 (top) and a cropped image (bottom). This high concentration (10k times diluted CNC-RBITC-3) sample has bright spots that are CNC aggregates as well as weaker spots due to single CNCs.

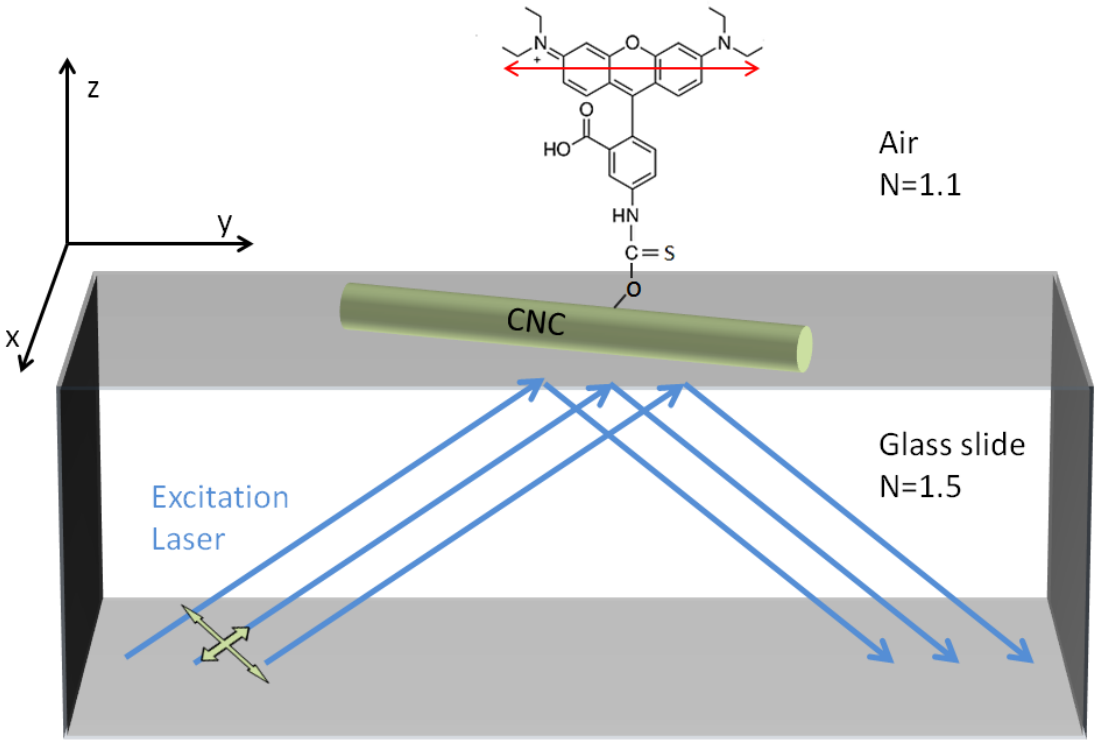

Figure 3-13: The schematic depiction of polarized TIRFM. The dye attached to the CNC surface will be at various orientations. The absorption dipole moment of RBITC is shown by the red arrow. The excitation laser emits with a certain angle and polarization direction. If the laser is circularly polarized, the polarization direction is shown by the green arrows.

Before imaging samples of CNC with lower density, the effects of laser polarization were examined. The probability of excitation is dependent on the alignment of the electric field vector of the light and the absorption dipole of the fluorophore[17] (Figure 3-13). To assess the polarization effect, a linearly polarized excitation laser obtained using a 532 nm half wavelength plate was used to excite the dye labeled CNC. The polarization direction of the laser was changed by rotating the half wavelength plate. A series of ten images were taken where the polarization angle was adjusted from 0 °to 180 °by 20 °steps. Small cropped regions from five

of these images are shown in Figure 3-14 (a) to (e).A change of intensity for individual particles at different polarizations was shown clearly for this experiment. An image excited by a circular polarized laser was simulated by averaging the intensities of all ten images (Figure 3-14 (f)). In this average intensity image, all the dye molecules can be detected, even though their dipoles are oriented at different angles with respect to the polarization of light. Thus, the circularly polarized excitation laser is an advantage to detect dye molecules with different orientations. However the circularly polarized laser beam will not excite molecules with their absorption dipoles oriented in the z-direction. Nevertheless, circularly polarized excitation is a good compromise as it will excite most dye molecules and was used for the following experiments. Thus, a circularly polarized excitation laser was used to minimize polarization effects and maximize the detection of the fluorophores.

(a) 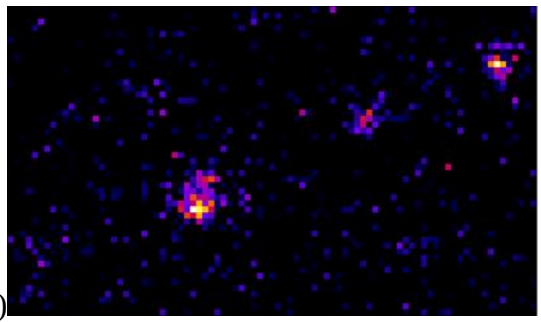 (b) 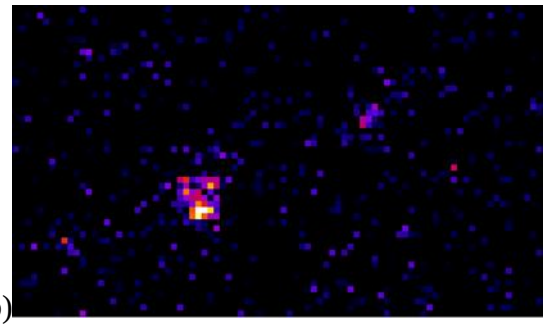

(c) 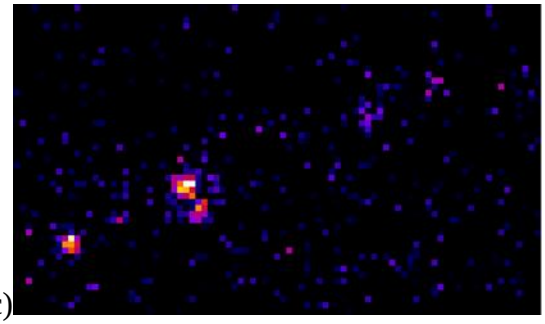 (d) 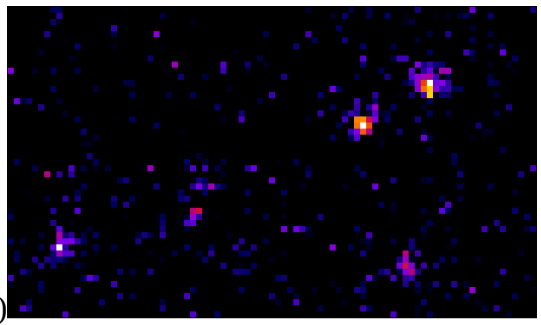

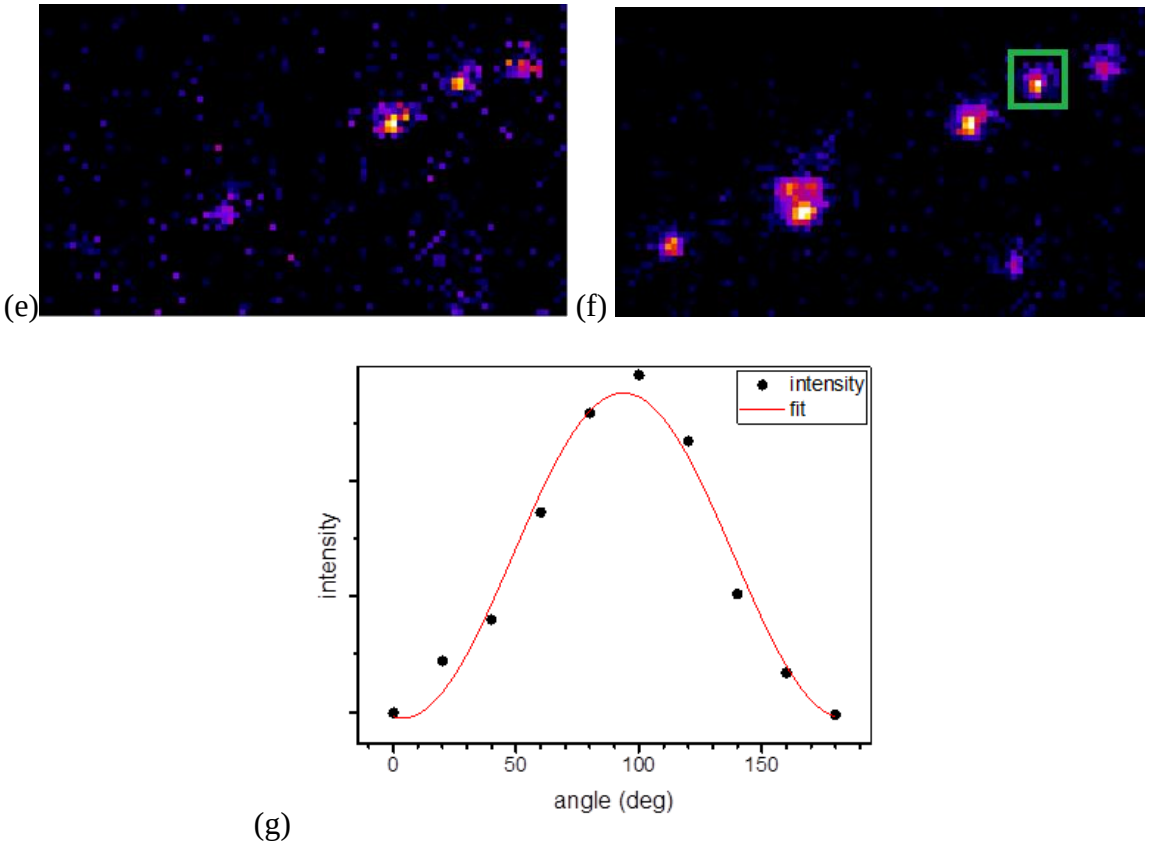

Figure 3-14: Five TIRF images from the total of ten images measured at various polarization angles: 0 (a), 40 (b), 80 (c), 120 (d), and 150 (e) degree; (f) intensity average image of all polarization images. The size of all images is 9 × 5 µm^2.The intensity plot of one selected fluorophore (green square) is shown in (g), which includes the all nine polarization angles. The red curve in (g) is sine square function fitting of all spots.

3.3.6 TIRFM photobleaching method to measure the dye loading in CNC

To determine the number of linked dyes per CNC particle, the blinking and photobleaching behaviour of single diffraction limited spots was analyzed. This method depends on measuring irreversible decreases in intensity that can be assigned to bleaching one fluorophore at a time. Irreversible bleaching of dye molecules frequently involves reaction with singlet oxygen

generated by energy transfer from the excited triplet state of the dye. Reversible bleaching or blinking of triplet states may also occur[18]. When the dye molecule is photobleached, it no longer emits and the number of dye molecules can be determined by counting the number of discrete intensity levels over a certain exposure time. In this experiment, a stream of 500 frames with 200 ms per frame exposure time was acquired. To maximize the excitation of fluorophores, a circularly polarized excitation laser was used. The intensity averaged image is shown in Figure 3-15, for a sample of CNC-RBITC diluted 1 million times. The density of spots is much lower than in Figure 3-12 and is ideal for a single molecule experiment. There are some rings in the background because of dust in the light-path. Dye labeled CNC produces diffraction-limited spots in TIRF which are approximately 3×3 pixels (107 nm per pixel) in the image. However, this spot size is larger than the size of individual CNC particles. Thus, TIRFM cannot distinguish whether a single spot contains an individual dye-labeled CNC or a small aggregate of dye-labeled CNCs. Moreover, unlabeled CNC is undetectable by TIRFM and free dye cannot be distinguished from dye attached to CNC. However, based on the anisotropy of CNC-RBITC-3 and the UV-Vis absorption of the dialysis wash, there is a low probability of unlinked dye molecules absorbed on the sample surface.

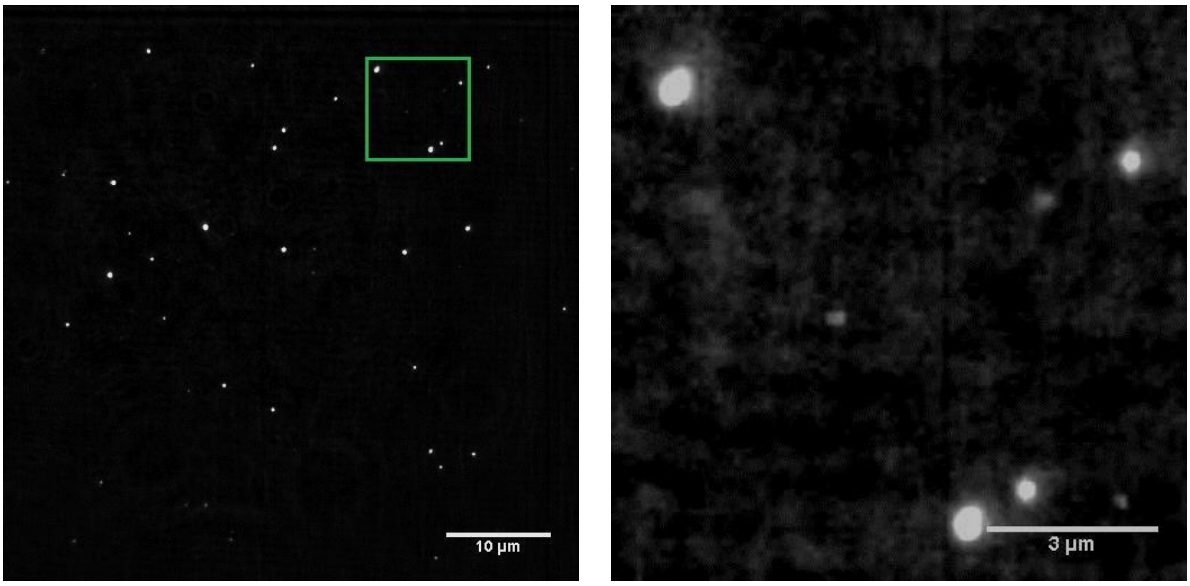

Figure 3-15: A typical average intensity image from a 500 frame stream (55 × 55 µm^2, left) and a cropped TIRF image (10 × 10 µm^2, right) from left (green square).

The data are analyzed using a macro which locates features that are four times higher than the standard deviation of a manually determined background. Then, the macro will let the analyzer look at the intensity vs times trace for each spot and determine the dye number from the intensity. An example of the imageJ macro measurement of a single spot is shown Figure 3-16 (a) which measures the average intensity of a selected 3 × 3 pixel area (green box in, Figure 3-16 a). The intensity vs frames of selected spots are plotted in red whereas a local background of 7 × 7 pixel area (yellow box in Figure 3-16 a) is plotted in black. The macro set the backgrounds measurement box at 20 pixels away from the spot being analyzed. However, if the local background box overlaps other fluorescent spots it can be moved manually. A typical one dye bleaching trace is shown in Figure 3-16 b. The intensity threshold (blue line) for a spot to be considered for analysis was set at two standard deviations above the local background intensity

(black trace). Then, the plots of intensity vs. frames for individual spots are analyzed to estimate the number of dyes.

(a) 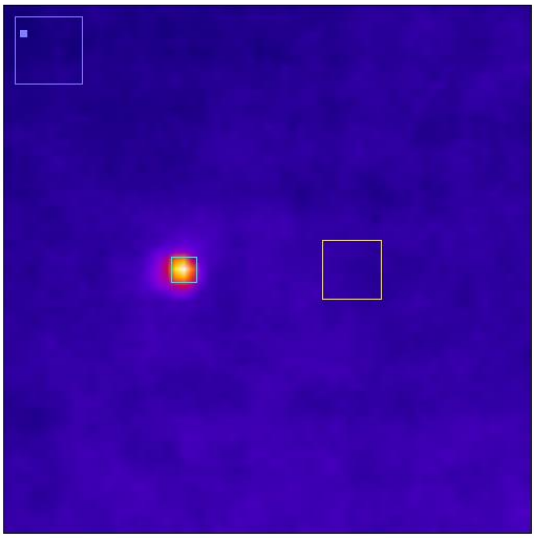 (b) 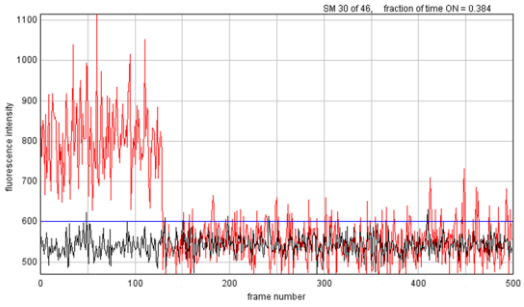

Figure 3-16: Enlarged area (a) of intensity averaged image. The green box is the 3 × 3 pixels measurement area and the yellow box is the 7 × 7 pixels background measurement area. Typical intensity vs. time trace assigned to one dye molecule photobleaching (b).

Figure 3-17 (a) shows an example with two dyes photobleaching. Sometimes, a quencher like oxygen reversibly turns off fluorescence by quenching the dye molecule, resulting in blinking (Figure 3-17 b). A one dye blinking trace is shown in Figure 3-17 (c). These complex blinking and bleaching processes can happen at the same time, as shown in Figure 3-17 (d). There are several possible interpretations for this trace. For example, there could be four dyes in this spot, three dyes are active at the beginning and the fourth dye is off. Then the first dye is quenched at the 20^{th} frame, followed by quenching of the 2^{nd} dye, then photobleaching of the third. The fourth dye is back on in the 150^{th} frame and the 2^{nd} dye is back on between frames 250 and 320.

This was the interpretation used by the author. For all 274 spots analyzed, only 2 were deemed ambiguous and open to interpretation. Thus, it cannot affect the result much.

In the case where dyes survive the exposure without blinking or photobleaching (Figure 3-17 e), the intensity approximation was used to determine the dye number. The intensity of a single dye can be approximated as ~500 in most cases. Thus, the dye number for traces that do not bleach has been determined as one if the intensity is between 300 and 700. Based on this rule, Figure 3-17 (e) is an example of one dye that never bleaches and Figure 3-17 (f) is two dyes where only one is bleached. Figure 3-17 (g) is two dye molecules that do not bleach during experiment; the dye number is determined to be 2, because the intensity difference between the trace and background is 1300. The second possibility is that there are 3 dyes, each of them with an intensity of 300. This intensity is the minimum intensity based on the data for clear one-step bleaching events. However, it seems unlikely that 3 dyes in the same area will all have the minimum intensity so the author assigned this spot to two dyes. The macro also selected some "fake spots" for analysis (Figure 3-17 h and i). The trace in Figure 3-17 (h) was rejected because the intensity of the spot was lower than the threshold line. The image in Figure 3-17 (i) was rejected because it is a digital noise spike from a CCD "hotspot".

(a)

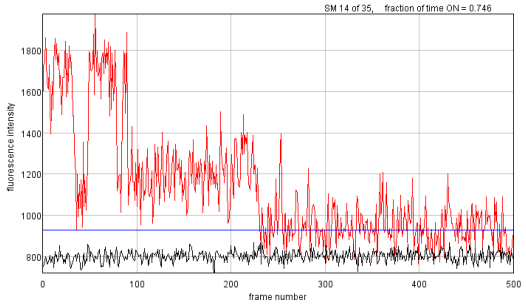

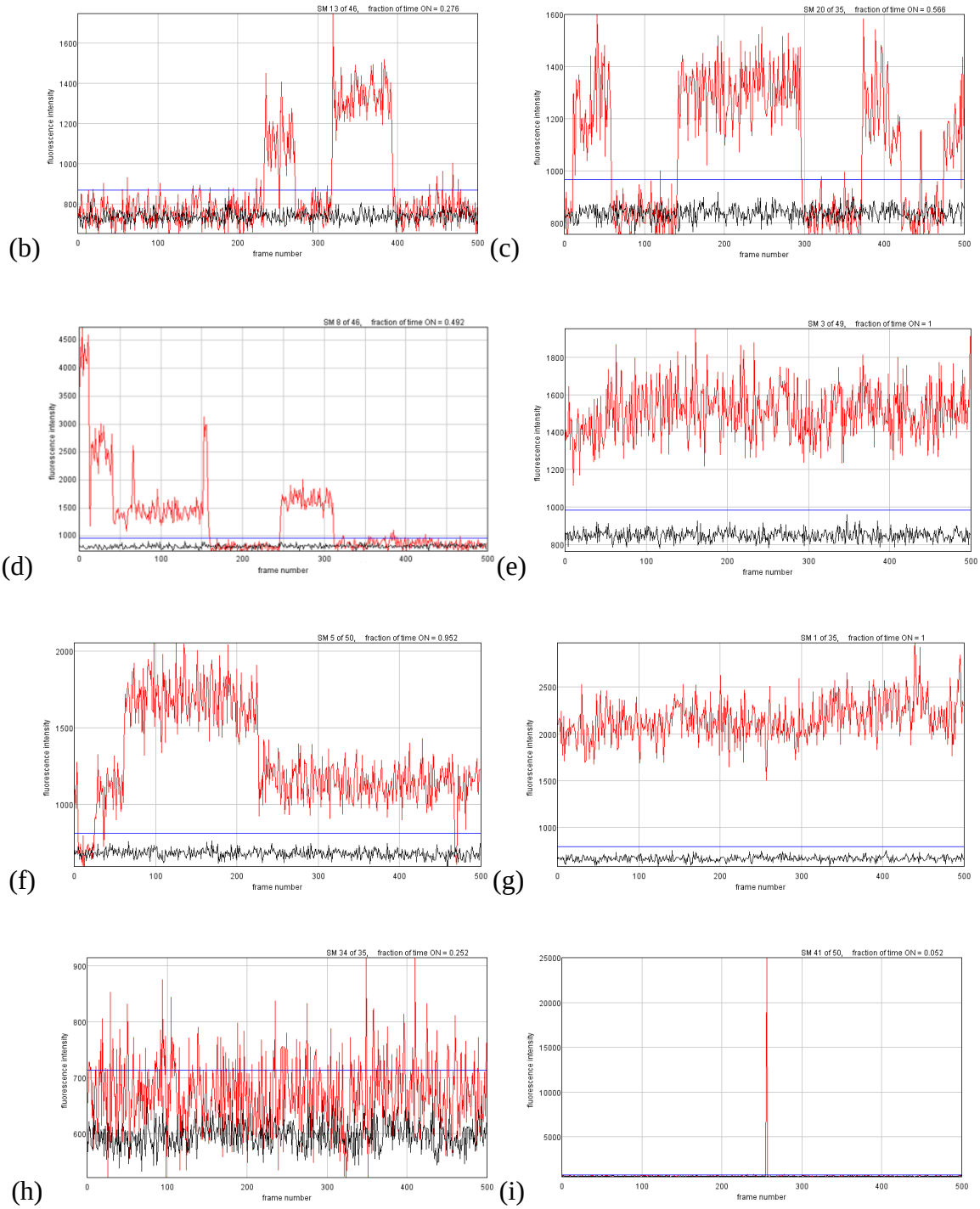

Figure 3-17: Typical intensity vs. time traces assigned to (a) two dyes photobleaching; (b) two dyes blinking, (c) one dye blinking, (d) three or four dye photobleaching and blinking, (e) one dye that does not bleach, (f) one dye blinking and another on for the entire trace; (g) two dyes that do not bleach.

Two typical rejected traces are shown in (h) which has a signal lower than the threshold and (i) which is digital noise from the detector.

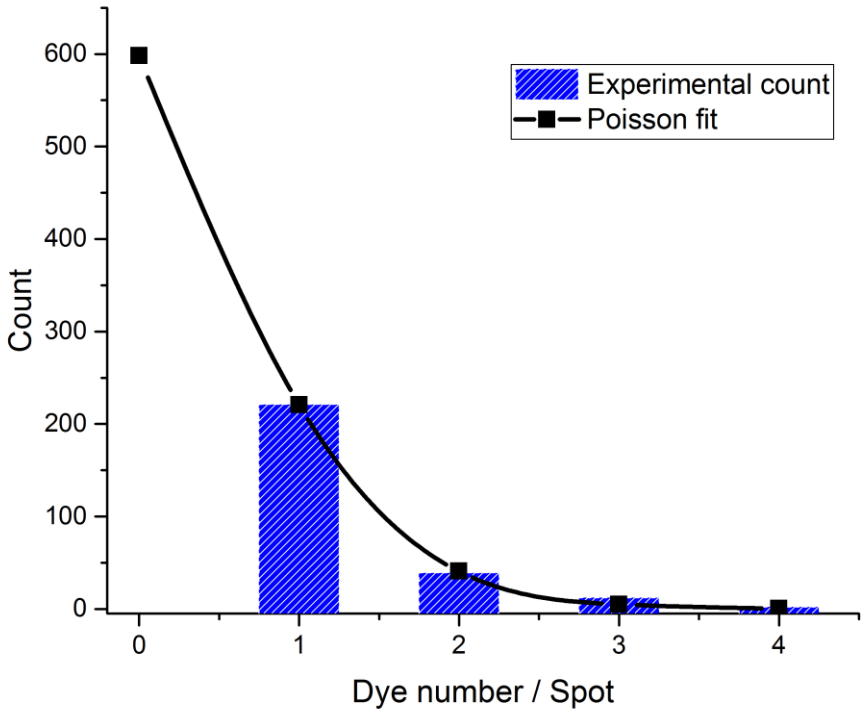

$$y(k) = A\frac{\lambda^k e^{-\lambda}}{k!}$$

A	λ	R^2
865	0.379	0.998

Figure 3-18: The dye number histogram for 274 spots analyzed by ImageJ Macro (blue).The Poisson distribution fitted to the dye number was used to estimate the number of unlabeled CNCs (Black line). The estimated unlabeled CNC is 598. The fitting function is shown in the bottom of the figure.

The histogram of dye number per TIRF spot obtained from 10 images with a total of 274 single spots is shown in Figure 3-18. All ten images came from one sample. Most of the spots

correspond to single dye molecules; however, there are some unlabeled CNC which are undetectable by TIRFM. A Poisson distribution was fitted to the histogram to estimate the number of unlabeled CNC. The Poisson distribution is a discrete distribution which expresses the probability of a given number of events occurring in a fixed interval of time or space if these events occur with a known average rate and independently of time [19]. The number of unlabeled CNCs is necessary to determine the dye loading efficiency for comparison with the estimates from absorption and emission in Table 3-5. The Poisson distribution and the fitting function are shown in Figure 3-18. The estimated number of unlabeled CNCs is 598 according to the fit. The estimated average CNC labeling ratio is 0.39 dye molecule per CNC according to equation 3-1.

$$c = \frac{1}{N}\sum nd \qquad \text{(Equation 3-1)}$$

N is the total count number including the experimental count of labeled spots and the estimated count for unlabeled particles, d is the dye number/spot and n is the count number for each d. The estimate of 0.39 dye per CNC is lower than the estimate obtained from either absorption or fluorescence methods (0.98, 0.73). The estimated value from the TIRF experiment has some assumptions. The most important assumption is that spots analyzed do not contain aggregates of labeled and unlabeled CNCs. Another assumption is that all fluorophores are excited and detected, has not been verified. Thus, an AFM experiment was performed to check the aggregation of CNC at this concentration.

3.3.7 AFM of RBITC labeled CNC

An AFM experiment was used to determine the level of aggregation for CNC-RBITC-3. In this case, the CNC-RBITC-3 suspension was diluted 1 million times, which is the same concentration

as the TIRF photobleaching experiment, but the sample was prepared on a PLL coated fresh mica substrate instead of the Piranha treated cover slide. A typical AFM image is shown in Figure 3-19. Red squares in the images highlight the CNC aggregates and green squares highlight the single CNC. The numbers of single CNC and aggregates were counted from 10 images (68 total counts) and the histogram is shown in Figure 3-20.

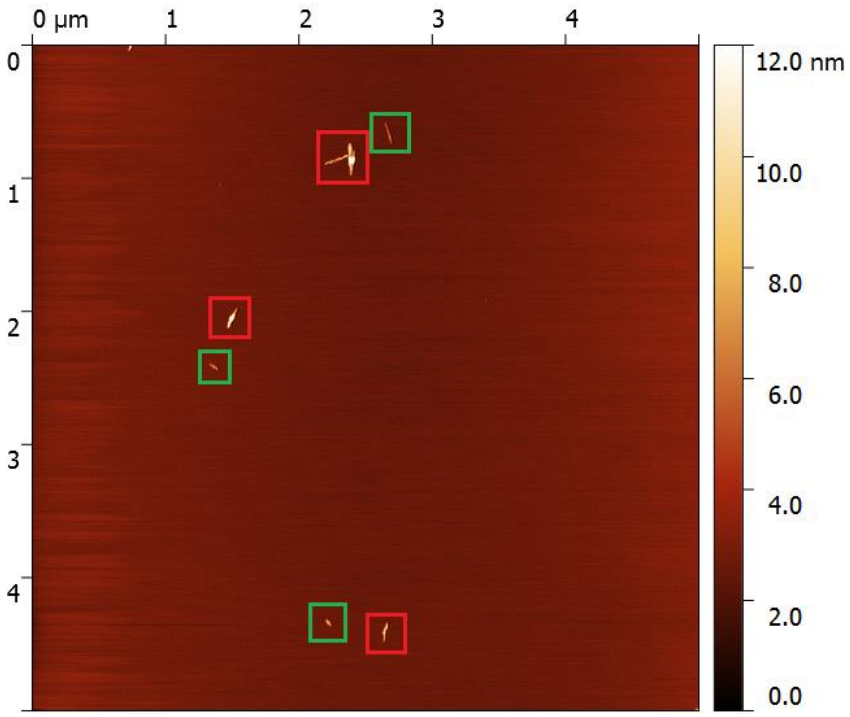

Figure 3-19: AFM image for 1 million times diluted CNC-RBITC-3 (5 × 5µm^2). Red squares highlight the CNC aggregates and green squares highlight the single CNC.

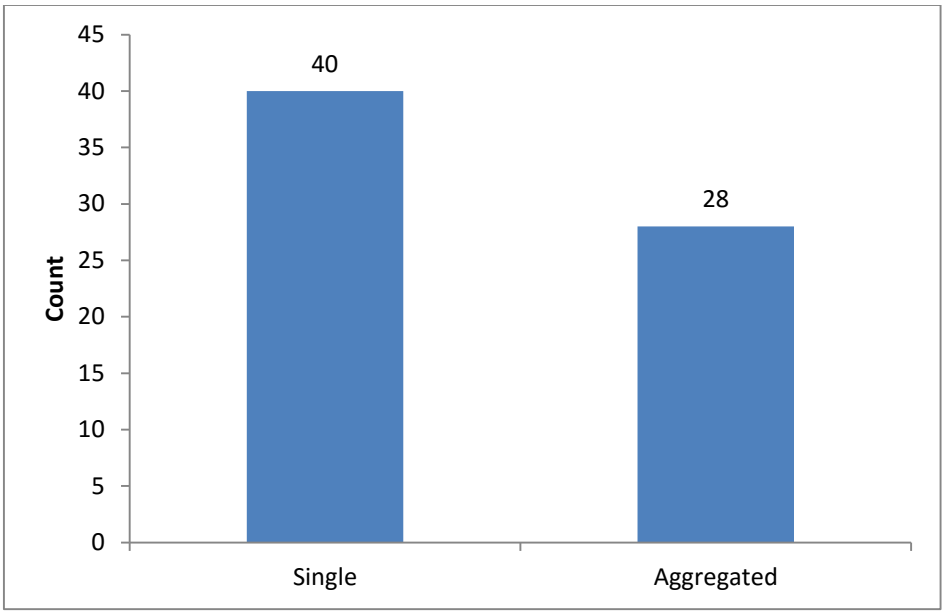

Figure 3-20: The histogram (n=68) of single and aggregated CNC-RBITC-3 from ten AFM images.

From the histogram, CNC aggregation is common for this concentration. Approximately 40% of the CNCs are aggregates, despite the high dilution. The high fraction of aggregates is a significant source of error for the estimates from the TIRF photo bleaching experiment. Because the aggregation situation is complex, it is hard to determine whether the dye loading is overestimated or underestimated from the single particle experiments.

3.3.8 AFM TIRF correlation for RBITC labeled CNC

Correlated AFM TIRF imaging for CNC-RBITC-3 can potentially be used to identify CNC with no dye and also to distinguish aggregates from single CNCs. Thus, an AFM TIRF correlation experiment was attempted. The process of correlation is first to obtain a TIRF image for a good sample area. The ideal sample area has well-separated fluorescent spots (~3 μm) and identifiable "constellations of spots" for ease of location of the same area in both AFM and TIRF images.

Then, the AFM tip is moved to the area of interest (Figure 3-21). The AFM is used to image the same position with a large scan area. If the position is roughly correlated based on the "constellation" or any other identification marker (i.e., dye labeled beads or aggregates), a smaller scan is recorded. Finally a second TIRF image is taken after the AFM scans to relocate every spot and check whether any are moved by AFM scanning. Since the small size of CNC makes it extremely difficult to ensure that the AFM and TIRF images overlap, 20 nm fluorescent beads were used for the correlation experiment. The fluorescence beads are brighter in TIRF images and higher in AFM images which helps to find the same area in the two images.

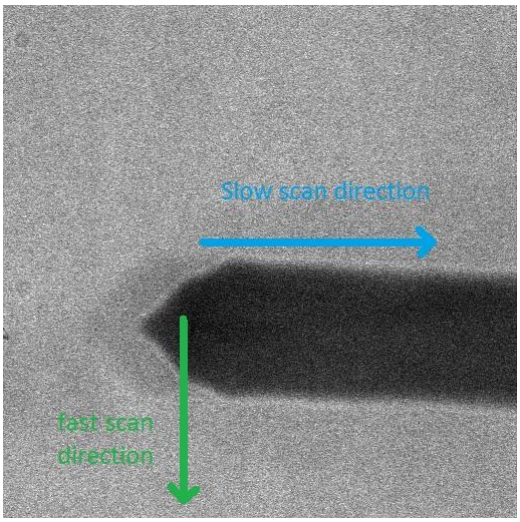

Figure 3-21: The AFM tip viewed using the 150 x TIRF lens in bright field. The image size is 55 × 55 μm²

The initial TIRF and AFM images for correlation are shown in Figure 3-22. An area which is believed to be a drying line is shown in both images. For the AFM image the height scale is 0 - 20 nm, thus, the white spots or bright red spots are the 20 nm beads, and the cyan spots should be the CNC particles or aggregates. The dying line helps to locate the same scan area more rapidly. The constellation like area which is selected in the green box is detected in both AFM and TIRF. Thus, this area has been selected for obtaining correlated images on a smaller length scale. The

other areas may correlate, but they do not have an obvious pattern of bright fluorescent beads to use to check the overlap of the images. Because the AFM tip is aging during scanning, the other areas cannot be measured at the same time.

The TIRF images recorded before and after the AFM image was collected are shown in Figure 3-23. In this figure, all the fluorescence spots have been labeled and named. The name consists of two letters and a number. ‘FB” means the spot is determined to be a fluorescent bead, ‘FC’ is assigned as dye labeled CNC, and ‘UK’ means the spot cannot be fully characterized. Green labeled spots appear in both TIRF images and the AFM image; orange labeled spots appear only in one of the TIRF images and the AFM image; red labeled spots appear in one TIRF image but not the AFM image, and are assigned as unknown fluorophores. The AFM image of this area is shown in Figure 3-24, in which all the particles are labeled the same way as in the TIRF images. There is also a red labeled spot in the AFM image that does not fluoresce at all. The AFM image was obtained by overlapping 7 different images at different resolutions, because some particles can be identified by scanning large area with low resolution and some have to be scanned as a small area to observe CNCs. The relative distances and angles between particles are listed in Table 3-6.

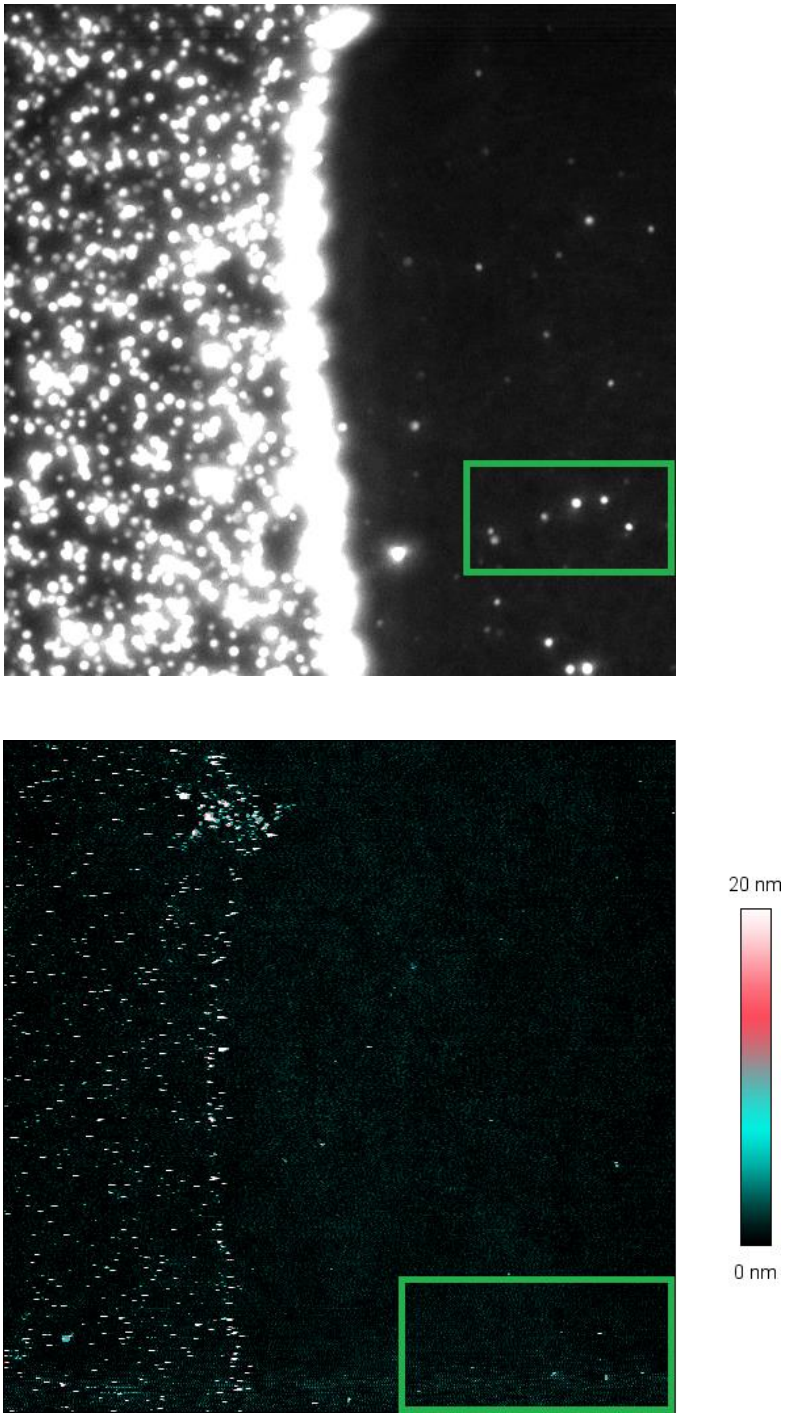

Figure 3-22: The TIRF overview image (top, 55 × 55 µm^2) and the AFM overview image (bottom, 30 × 30 µm^2). The correlation area is labeled with a green box in both images.

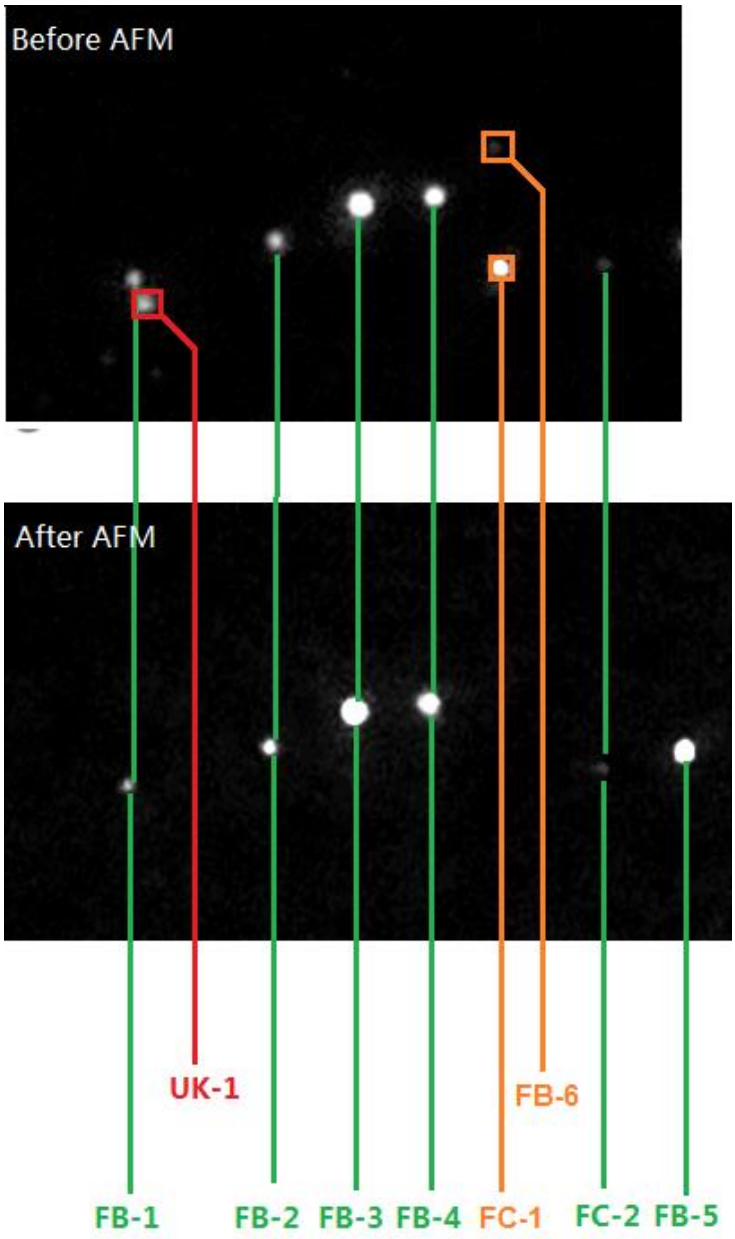

Figure 3-23: Comparison of TIRFM images for the correlated area before and after AFM scanning. Because of the scanner placement, the whole sample was moved about 1.5 µm after AFM scanning. Thus, the cropped image after AFM is longer than the before image. All spots are labeled and named.

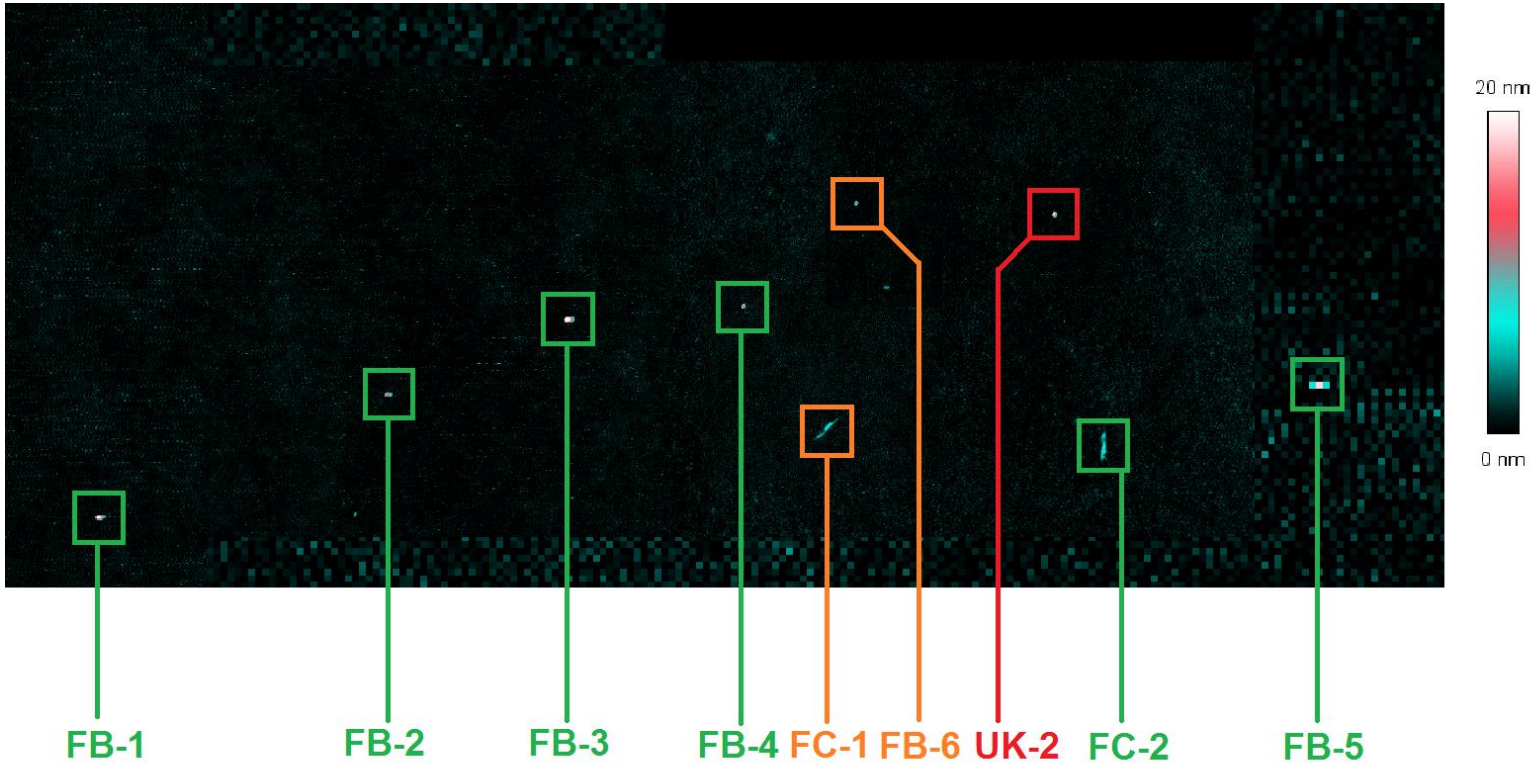

Figure 3-24: The AFM image of the correlation area. The image is created from 7 different AFM images. The red label means that the feature appears only in the AFM image, and is probably a non-fluorescent bead.

Table 3-6: The relative distances and angles between two particles in TIRF and AFM images. The right horizontal direction is set as 0 degree.

Between Particles	FB-1/FB-2	FB-2/FB-3	FB-3/FB-4	FB-4/FC-1	FB-4/FC-2	FB-4/FB-5	FB-4/FB-6
Distance in AFM image (μm)	2.75	1.62	1.52	1.50	3.30	4.94	1.52
Distance in TIRF image before AFM (μm)	2.80	1.74	1.40	1.64	3.47	N/A	1.48
Distance in TIRF image after AFM(μm)	2.70	1.68	1.44	N/A	3.38	4.90	N/A
Angle in AFM image (°)	22	23	6	-50	-22	-8	45
Angle in TIRF image before AFM (°)	16	23	6	-49	-23	N/A	45
Angle in TIRF image after AFM (°)	15	25	7	N/A	-22	-11	N/A

Comparing the TIRF images, AFM image, and data in Table 3-6, all the green labeled particles are well correlated. Only FB-1 and FB-5 have complications that need to be considered. FB-5 is at the very edge of the before TIRF image, so that its position is not clear. FB-1 has a different angle between the TIRF and AFM image (Table 3-6), but is well correlated based on the distance. This error may come from the irregular cover slide. The orange labeled particles FC-1 and FB-6 only appear in the TIRF image before AFM and the AFM image. Both of them may be quenched in the second TIRF image or removed during AFM scanning. FC-1 is a CNC aggregate (Figure 3-25 d) with dyes linked. FB-6 is a dim fluorescent bead. There are two red 'UK' labeled particles. UK-1 only appears in the TIRF image before AFM. This feature may be either a fluorescent bead which attached to the AFM tip and moved, or a free dye aggregate which was removed during AFM scanning. The first possibility is more reasonable. UK-2 is identified as a no fluorescent bead from the high resolution AFM image (Figure 3-25 c) since it looks similar to FB-3 (Figure 3-25a). That is reasonable because there is no guarantee that every single bead has been labeled.

From this experiment, two CNC particle aggregates have been correlated successfully. Both of these aggregates consist of two CNCs. FC-1 (Figure 3-25 d) is a short CNC stuck to a longer one. FC-2 (Figure 3-25 b) is probably two CNCs, either one on top of a second or two end-to-end. Both FC-1 and FC-2 are validated as having at least one dye labeled CNC. Although this experiment demonstrates that dye-labeled CNCs can be detected in both AFM and TIRF images, more areas and more CNCs correlated are required to draw any conclusions on the fraction of labeled CNCs. However, the correlation experiment is limited by tip aging. After fast scanning a large area (30×30 μm^2, 1 Hz), the tip is easily contaminated before scanning the small area

required to image CNC. Moreover, the tip cannot be changed during the correlation experiment, because it is impossible to replace the tip and scanner and scan exactly the same sample area.

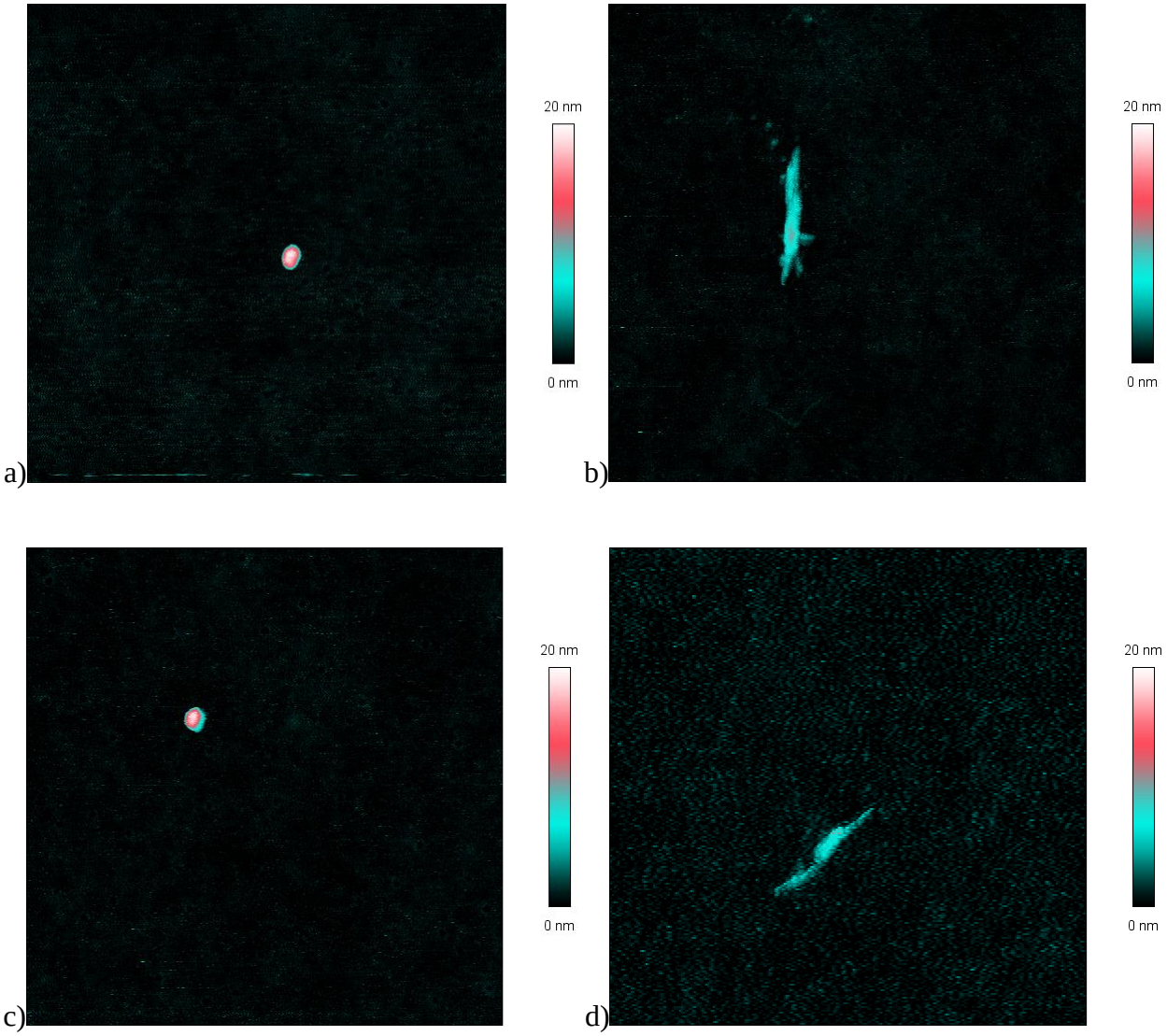

Figure 3-25: The high resolution AFM images (1 × 1 µm^2) of (a) FB-3, (b) FC-2, (c) UK-2 and (d) FC-1.

3.4 Conclusion

In this chapter, two dyes have been covalently attached to the CNC surface successfully. Moreover, the photophysical parameters have been studied in detail using four different absorption and fluorescence methods, which has not typically been done for other dye-labeled CNCs. Although, fluorescence lifetimes and anisotropy showed clear changes that were consistent with covalent attachment of the dye to the surface, DTAF dye labeled CNC was not examined in further detail because its pH sensitivity would be problematic for applications for polymer composites.

RBITC has been one of the most popular dyes used for labeling CNCs. Three RBITC labeled CNC with different dye loadings have been prepared and examined by absorption and fluorescence methods. The scattering method has been used to characterize the concentration of the CNC suspension because it requires less sample. In this case, the experimental scattering curves gave good fits to the Mie scattering equation. In the future, if the conditions permit, a simple drying process will be used to measure the suspension concentration. Fluorescence lifetimes and anisotropy measurements were consistent with covalent attachment of the dye to the CNC surface.

Two approaches, absorption method and fluorescence spectroscopy have been used to characterize the dye loading efficiency. Each of them has potential advantages and disadvantages and assumptions which may contribute to error. Both methods are fast and convenient to use, but competing absorption by the dimer has not been accounted for. Furthermore, the fluorescence intensity decreases with increased dye loading which probably reflects quenching by dimers or oligomers. These results indicate that adding more RB will not lead to a better dye-labeled CNC

due to problems associated with the dimer and possibly other oligomers. Therefore, understanding the photophysics indicates that a low dye loading is optimal for RB and that if a higher dye loading is needed, then a different dye is likely to be more useful. The dye loading used in this thesis (~ 1.0 μmol/g) is similar to Nielsen's results for a RB-labeled CNC (2.1 μmol/g)[4]. However, Mahmoud and Endes have used ten times higher dye loadings (21 μmol/g[10] and 32 μmol/g[8]), so the presence of the dimer will have resulted in much lower fluorescence intensity than would be expected for the higher dye loading.

One of the RBITC-CNC samples was selected for TIRF single particle fluorescence and correlated AFM/TIRFM experiments. Most features observed in TIRF were identified as having one or two dye molecules and the number of unlabeled CNCs was then estimated by Poisson fitting, assuming that all features observed in TIRF were individual CNCs (not aggregates). However AFM and correlated AFM-TIRF experiments showed the limitations of this assumption. Another problem is that the dimer will lead to a nonfluorescent RB and the CNC will be "off" in the TIRF images.

Comparing all three methods for estimating the dye loading, we have 0.98 dye per CNC for absorption, 0.73 dye per CNC from fluorescence and 0.39 dye per CNC from TIRF. We assume that the absorption number is overestimated since some absorption is due to dimer and presumably 0.98 is the upper limit for the amount of dye. The fluorescence method gives a lower result than absorption. The TIRF is even lower, suggesting that it is the least good. Probably this is because TIRF has the same problems as both other methods, plus the additional complication of aggregated CNCs. Complications aside, it is clearly possible to use relatively low dye labeling efficiencies and still have adequate sensitivity to detect individual CNCs.

The AFM/TIRFM correlation has the potential to give more accurate estimates of dye loading for CNC. However, as a high-end single molecule detection experiment, the correlation method demands high operator skill and an expensive instrument, and is limited by AFM tip aging. It is unlikely to be a common testing method for dye loading. In the future, AFM/TIRFM correlation might be used to estimate dye loading with more number of correlated particles.

3.5 References

1. Filpponen, I.; Sadeghifar, H.; Argyropoulo, D. S., Photoresponsive cellulose nanocrystals. *Nanomaterials and Nanotechnology* **2011,** *1* (1), 34-43.
2. Grate, J. W.; Mo, K.-F.; Shin, Y.; Vasdekis, A.; Warner, M. G.; Kelly, R. T.; Orr, G.; Hu, D.; Dehoff, K. J.; Brockman, F. J., Alexa Fluor-Labeled Fluorescent Cellulose Nanocrystals for Bioimaging Solid Cellulose in Spatially Structured Microenvironments. *Bioconjugate chemistry* **2015,** *26* (3), 593-601.
3. Moon, R. J.; Martini, A.; Nairn, J.; Simonsen, J.; Youngblood, J., Cellulose nanomaterials review: structure, properties and nanocomposites. *Chemical Society Reviews* **2011,** *40* (7), 3941-3994.
4. Nielsen, L. J.; Eyley, S.; Thielemans, W.; Aylott, J. W., Dual fluorescent labelling of cellulose nanocrystals for pH sensing. *Chemical Communications* **2010,** *46* (47), 8929-8931.
5. Sadeghifar, H.; Filpponen, I.; Clarke, S. P.; Brougham, D. F.; Argyropoulos, D. S., Production of cellulose nanocrystals using hydrobromic acid and click reactions on their surface. *Journal of Materials Science* **2011,** *46* (22), 7344-7355.
6. Abitbol, T.; Palermo, A.; Moran-Mirabal, J. M.; Cranston, E. D., Fluorescent labeling and characterization of cellulose nanocrystals with varying charge contents. *Biomacromolecules* **2013,** *14* (9), 3278-3284.
7. Dong, S.; Roman, M., Fluorescently labeled cellulose nanocrystals for bioimaging applications. *Journal of the American Chemical Society* **2007,** *129* (45), 13810-13811.
8. Endes, C.; Mueller, S.; Kinnear, C.; Vanhecke, D.; Foster, E. J.; Petri-Fink, A.; Weder, C.; Clift, M. J.; Rothen-Rutishauser, B., Fate of cellulose nanocrystal aerosols deposited on the lung cell surface in vitro. *Biomacromolecules* **2015,** *16* (4), 1267-1275.
9. Thomson, C. I.; Lowe, R. M.; Ragauskas, A. J., Imaging cellulose fibre interfaces with fluorescence microscopy and resonance energy transfer. *Carbohydrate polymers* **2007,** *69* (4), 799-804.
10. Mahmoud, K. A.; Mena, J. A.; Male, K. B.; Hrapovic, S.; Kamen, A.; Luong, J. H., Effect of surface charge on the cellular uptake and cytotoxicity of fluorescent labeled cellulose nanocrystals. *ACS applied materials & interfaces* **2010,** *2* (10), 2924-2932.

11. Vieira Ferreira, L.; Cabral, P.; Almeida, P.; Oliveira, A.; Reis, M.; Botelho do Rego, A., Ultraviolet/visible absorption, luminescence, and X-ray photoelectron spectroscopic studies of a rhodamine dye covalently bound to microcrystalline cellulose. *Macromolecules* **1998,** *31* (12), 3936-3944.

12. (a) Siegler, R.; Sternson, L.; Stobaugh, J., Suitability of DTAF as a fluorescent labelling reagent for direct analysis of primary and secondary amines—spectral and chemical reactivity considerations. *Journal of pharmaceutical and biomedical analysis* **1989,** *7* (1), 45-55; (b) Johnson, I.; Spence, M., The molecular probes handbook. *Life Technologies Corporation* **2010**.

13. (a) Kajiwara, T.; Chambers, R. W.; Kearns, D. R., Dimer spectra of rhodamine B. *Chemical Physics Letters* **1973,** *22* (1), 37-40; (b) Ramette, R.; Sandell, E., Rhodamine B equilibria. *Journal of the American Chemical Society* **1956,** *78* (19), 4872-4878.

14. Graaff, R.; Aarnoudse, J.; Zijp, J. R.; Sloot, P.; De Mul, F.; Greve, J.; Koelink, M., Reduced light-scattering properties for mixtures of spherical particles: a simple approximation derived from Mie calculations. *Applied optics* **1992,** *31* (10), 1370-1376.

15. Marius, P.; Leung, Y. M.; Piggot, T.; Khalid, S.; Williamson, P., Probing the oligomeric state and interaction surfaces of Fukutin-I in dilauroylphosphatidylcholine bilayers. *European Biophysics Journal* **2012,** *41* (2), 199-207.

16. Beck-Candanedo, S.; Roman, M.; Gray, D. G., Effect of reaction conditions on the properties and behavior of wood cellulose nanocrystal suspensions. *Biomacromolecules* **2005,** *6* (2), 1048-1054.

17. Lakowicz, J. R., *Principles of fluorescence spectroscopy*. Springer Science & Business Media: 2013.

18. Vogelsang, J.; Kasper, R.; Steinhauer, C.; Person, B.; Heilemann, M.; Sauer, M.; Tinnefeld, P., A reducing and oxidizing system minimizes photobleaching and blinking of fluorescent dyes. *Angewandte Chemie International Edition* **2008,** *47* (29), 5465-5469.

19. J.H. Ahrens, U. D., *Computer methods for sampling from gamma, beta, poisson and bionomial distributions* Springer: 1974; Vol. 12.

Chapter 4

Surface modified CNC and polymer composite films

4.1 Introduction

One of the most promising applications of CNCs is their use as an additive to improve the properties of polymer composites, particularly the mechanical strength. Due to their hydrophilic character, CNCs can be readily incorporated in hydrophilic polymers, such as polyethylene oxide (PEO)[1] and polyvinyl alcohol (PVA)[2]. In addition, CNC is easily surface modified to be incorporated into a wide range of hydrophobic polymer matrices such as polycaprolactone (PCL)[3], polystyrene (PS)[4], polyvinyl acetate (PVAc)[5], ethylene-vinyl acetate (EVA)[6], epoxides[7], polylactic acid (PLA)[8], polyethylene (PE)[9], and polypropylene (PP)[10].

For most CNC-polymer applications a uniform distribution of CNCs in the polymer matrix is required. This is important because aggregated CNCs may require a larger amount of CNCs to achieve the desired improvement in properties and since aggregates may function as defect sites in the matrix. Therefore, the strong tendency of CNCs to self-assemble into large aggregates in some environments is a limitation to their successful use in nanocomposites. There are two methods that are usually used to characterize the CNC distribution in composites, which are electron microscopy (EM)[11] and light field microscopy (LFM)[8]. However, both the methods have clear disadvantages. EM is a method which is costly, time-consuming and inconvenient to use. EM can only examine the top layer of the sample, unless the sample is sectioned into thin slices. EM also has contrast problems and requires a heavy metal stain for good imaging contrast for CNC which makes it very different to locate single CNCs in polymer composites. Although the LFM is simple and convenient, it has limited resolution and only allows examination of large μm scale aggregates in composites. However, for industrial applications, people demand an efficient, low cost, and real-time method for measuring particle distributions. Thus, alternate approaches to either EM or LFM would be very useful.

As a relatively low cost, easy to operate and higher resolution/sensitivity technology, fluorescence microscopy can offset the disadvantages of SEM and LFM. In recent years, CNCs have attracted significant attention as nanoscale fluorescent sensors, owing to the possibility of their surface conjugation with various known fluorophores[12]. Dyes such as FITC, DTAF and Alexa were already conjugated to CNCs for bio-imaging[12], CNC-dye conjugates were used to visualize PVA fibers[13] and dye-labeled cellulose nanofibrils have been imaged in polyethylene composites[14]. Thus, dye labeled CNCs should be useful for characterizing the distribution of CNCs in composites.

In this chapter rhodamine-labeled CNC was used to assess the distribution of CNCs in polymer films. In contrast to an earlier study which used a CNC-dye conjugate to visualize PVA fibers[13], the focus here is on examining a range of CNC loadings and on investigating the detailed organization of CNCs in the polymer films. The dye labeled CNC (CNC-RBITC-3) has been incorporated into polyvinyl alcohol (PVA) films and studied by fluorescence microscopy. PVA has been selected because it is a bio-based hydrophilic polymer. For comparison, nitrobenzene modified CNC has been incorporated into polystyrene (PS) films. All the polymer film samples were provided by our collaborator Rongbing Du from the National Institute for Nanotechnology (NINT). These experiments demonstrated that the level of CNC agglomeration varies significantly for different film preparation methods, indicating that fluorescence microscopy is a useful and easily accessible method for optimizing film preparation. The self-quenching of the dye in the film was also measured and discussed and is an important consideration for choice of the dye loading and CNC content in the films.

4.2 Experimental

4.2.1 Dye labeled CNC and Polyvinyl alcohol (PVA) composite film

For spin coated films, 3 g PVA was weighed and dissolved in 97 g Milli-Q water. The calculated amount of dye-modified CNC (CNC-RBITC-3) dispersion was mixed with 10 g 3 wt. % PVA solution and stirred for 30 minutes. Two or three drops of suspension were spin coated onto the cover slide surface using 2000 rpm or 4000 rpm. All cover slides were cleaned with Piranha solution for 30 minutes before use. The thicknesses of the spin coated films were measured by AFM.

For the drop cast films, suspensions were prepared by mixing a calculated volume of the CNC-RBITC-3 suspension with the required weight of polymer. The solutions were then sonicated for 5 minutes to re-disperse any agglomerates formed. The films were obtained by pouring 0.8 mL of the CNC/polymer solution onto a clean cover slide and air drying for 48 hours. All cover slides for this experiment were cleaned using Piranha solution for 30 minutes. To measure the thickness of drop cast films, the film was pulled from the cover slide and the thickness measured using a screw micrometer (Marathon, USA).

4.2.2 Surface modified CNC and Polystyrene (PS) composite films

The nitrobenzene modified CNC (NB-CNC, prepared using a diazonium salt reaction) suspension was freeze-dried for 3 days using a FreeZone 4.5 Plus apparatus from Labconco Corporation (Missouri, Kansas City). Modified CNC (0.05 g) and 9.95 g Polystyrene (PS) pellet (or other CNC/PS ratios, as required) were mixed together in a glass vial and 10 ml toluene was added. The mixture was stirred until the solid was fully dispersed in toluene. The suspension was

spin coated on the cover slide surface at 2000 rpm. All the samples were placed in individual protective sleeves and covered with aluminum film before shipping.

4.2.3 Epi-fluorescence microscopy

Epi-fluorescence images were measured using an Olympus 1X 81 inverted microscopes with a high resolution CCD camera (1392 ×1040 pixels, CoolSNAP ES, Photometrics, USA). The objective lenses used in this experiment were an Olympus 100x UPlanSApo objective (air immersion, N.A 1.4), and an Olympus 20x UPlanSApo objective (air immersion, N.A 0.75, 0.17 mm cover slide corrected). Since there is no cover slide correction in the 100x UPlanSApo lens and the film is coated on one side of the coverslide, all film samples were flipped upside down for imaging. The sample was measured in epi-fluorescence mode using a Cy3 filter and a Xenon light source (evolve, Photometrics, USA). The excitation wavelength was 514-555 nm and emission wavelength was 570-616 nm. Ten images from random areas were recorded for each film. All images were analyzed by ImageJ software, which measured the average and variance of intensity for the entire image and then the results for all ten images for each film were averaged. Intensity data were plotted with Origin software. All the images were corrected for background by subtracting the image for the 0.00 wt. % sample before analysis. All the images shown in this chapter are the original images before background correction.

4.2.4 Atomic force microscopy (AFM) to measure film thickness

A sharp tweezer was used to scratch the film surface. Then, the scratched area was imaged by AFM. Contact mode AFM imaging was used to measure the thickness of the composite film in air using the JPK NanoWizard® II AFM. A platinum coated tip was used for imaging. The tip used was the MikroMasch HQ: DEP-XCS-11 cantilever B which has a typical spring constant of

2.7 N/m. The image size was 100 × 100 μm^2 (256 × 256 pixels) and the data was analyzed by Gwyddion.

4.3 Results and Discussion

4.3.1 Polystyrene (PS) films

Polystyrene (PS) films containing nitrobenzene modified CNCs were prepared by the spin coating method. PS is a common hydrophobic polymer material, and nitrobenzene-modified CNC is also hydrophobic. Four samples with different CNC concentrations were prepared, as shown in Table 4-1. Visual inspection indicated that these four composite films were transparent and that there was no obvious difference between films prepared at the two spin rates (4000 rpm and 2000 rpm). However, the 1.0 wt. % films appeared to be more yellow than the 0.5 wt. % films. Pictures of the PS films doped with NB-CNC on top of a colored background are shown in Figure 4-1.

Table 4-1: Nitrobenzene modified CNC and PS composite films.

Sample name	CNC-NB-1	CNC-NB-2	CNC-NB-3	CNC-NB-4
CNC Conc. (wt. %)	0.5	0.5	1.0	1.0
Spin speed (rpm)	2000	4000	4000	2000
Thickness (μm)	11.2 ±1.2	8.2 ±0.8	8.1 ±0.6	10.3 ±1.5

Although the films look transparent by eye, examination by bright field microscopy using a 20x objective showed that the distribution of modified CNC was very heterogeneous (Figure 4-2) with a large number of aggregates. Although unmodified CNC is hydrophilic, the CNC after nitrobenzene modification is less hydrophilic, and PS is hydrophobic. The pictures of CNC-NB indicate that even though CNC-NB is expected to be less hydrophilic than CNC, it still does not

disperse very well in PS. By comparing the sample pictures at different spin speeds, it is observed that speed had no influence on the distribution of the CNC in the film (Figure 4-2). Furthermore, the pictures indicate that the aggregates are smaller in the films with 1 wt. % CNC compared to those with 0.5 wt. %.

The images collected using a Cy3 filter set are also shown in Figure 4-2 (right column). The reason that CNC aggregates are visible using the Cy3 filter may be due to either autofluorescence of CNC or the Raman scattering signal from the CNC surface. Autofluorescence has been reported by Kalita et al[15] and Sacui et al[16] for sulfated CNCs. Although the CNC is nitrobenzene modified, it may still auto fluoresce. Moreover, Raman scattering can be captured by a low magnification lens with a sensitive CCD detector. Because the PS in the film provides a low intensity background, the Cy3 images have better contrast than the bright field images.

Thicknesses of samples are listed in Table 4-1. From the table we can see that with the same spin rate, the sample films have the same thicknesses. The spin rate and the thickness have an inverse relationship while the CNC concentration does not affect the film thickness over the limited concentration range tested here.

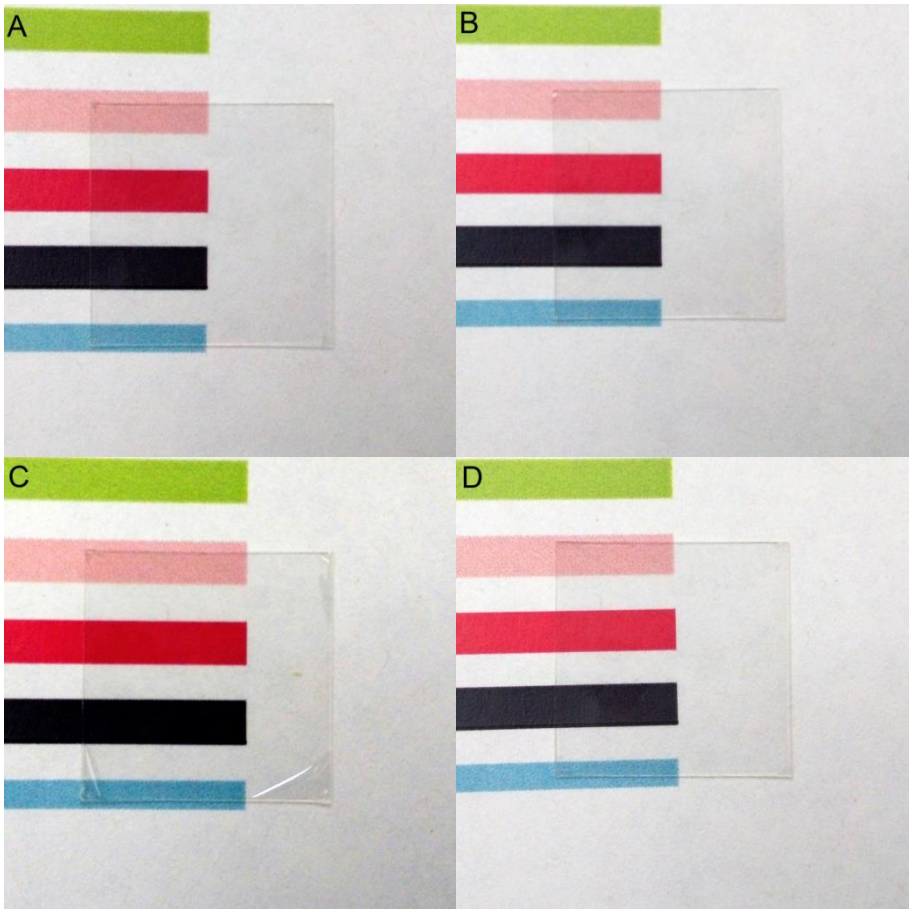

Figure 4-1: Typical pictures of nitrobenzene modified CNC and PS composite films mounted on glass slides with a pattern of colored lines: a) CNC-NB-1, b) CNC-NB-2, c) CNC- NB-3 and d) CNC- NB-4. The size of the glass slide is 20 × 20 mm^2.

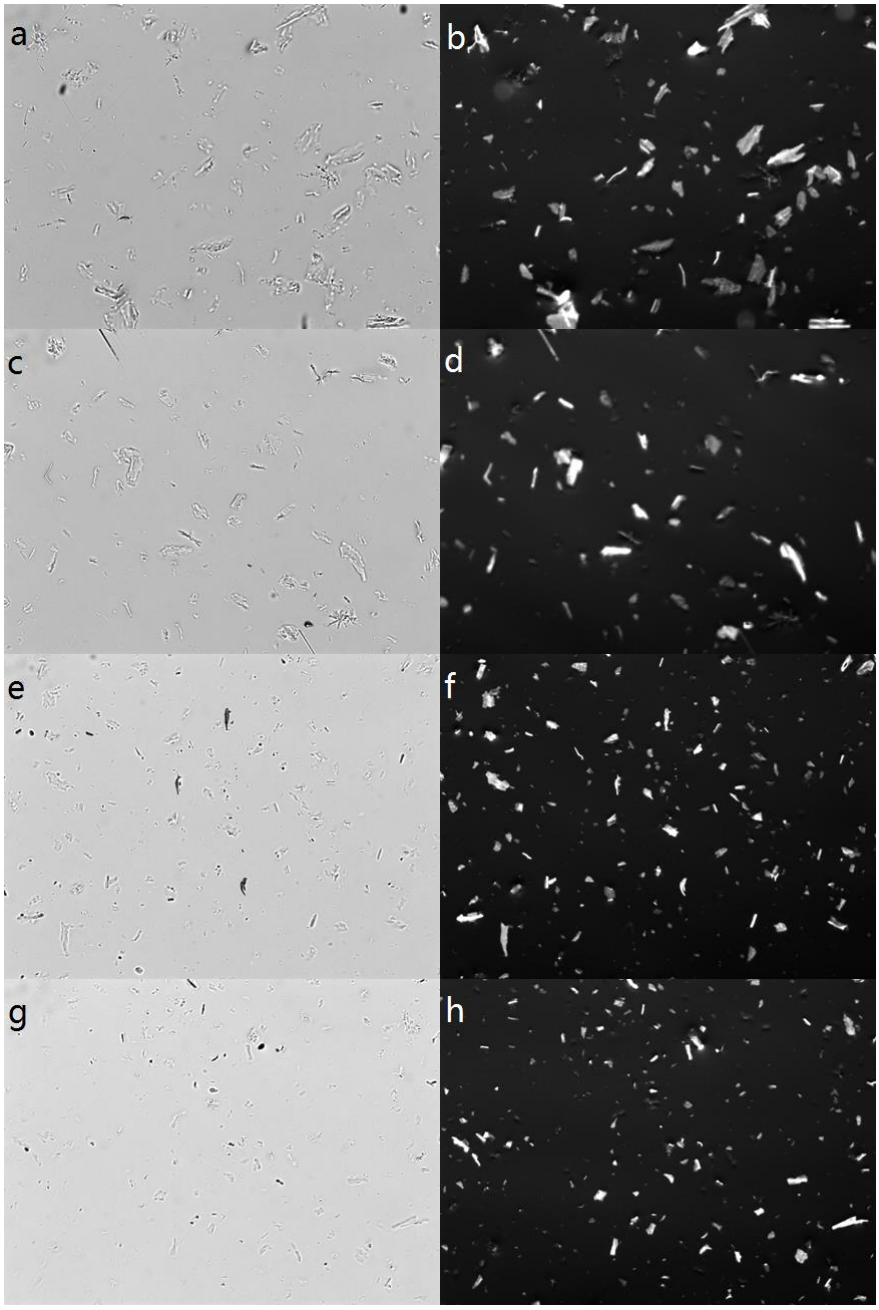

Figure 4-2: Images of PS films containing nitrobenzene modified CNCs (440 × 330 μm^2 area). The left column shows bright field images and the right column has Cy3 images measured from the same position of the film. (a), (b) CNC-NB-1, (c), (d) CNC-NB-2, (e), (f) CNC-NB-3, and (g), (h) CNC-NB-4.

4.3.2 Dye labeled CNC PVA films

Three sets of dye-labeled CNC PVA films were prepared. The first set was prepared by spin coating (4000 rpm) with concentrations from 0.00 wt. % to 0.99 wt. % (Table 4-2); the second set was prepared by spin coating (2000 and 4000 rpm) with concentrations from 0.00 wt. % to 7.37 wt. % (Table 4-3); the third set was prepared by the drop cast method with 0.00 wt. % to 9 wt. % CNC (Table 4-4).

Table 4-2: The concentration of CNC-RBITC-3 in film set 1.

Film set 1 (4000 rpm) sample number	**0**	**1**	**2**	**3**	**4**	**5**	**6**	**7**
CNC conc. (wt. %)	0.00	0.05	0.10	0.20	0.39	0.59	0.78	0.99

Table 4-3: The concentration of CNC-RBITC-3 in film set 2.

Film set 2 (2000 rpm) sample number	**0**	**1**	**2**	**3**	**4**	**5**	**6**	**7**	**8**
CNC conc. (wt. %)	0.00	0.01	0.23	0.60	0.97	1.89	3.74	5.50	7.37

Film set 2 (4000 rpm) sample number	**0**	**1**	**2**	**3**	**4**	**5**	**6**	**7**	**8**
CNC conc. (wt. %)	0.00	0.01	0.23	0.60	0.97	1.89	3.74	5.50	7.37

Table 4-4: The concentration of CNC-RBITC-3 in film set 3.

Film set 3 (drop cast) sample number	**0**	**1**	**2**	**3**	**4**	**5**	**6**	**7**
CNC conc. (wt. %)	0.000	0.007	0.037	0.072	0.410	0.760	4.500	9.000

The distribution of CNC in composite film set 1 was characterized by epifluorescence microscopy. Images with the same gray level are shown in Figure 4-3. The CNC was well distributed in the film and the aggregation is less than the PS film. Figure 4-4 shows a comparison of samples with the same 1 wt. % concentration for both PS and PVA films; the image for the PS composite has been cropped to the same size as the image for the PVA composite. The distribution of CNC in the PS film is very non-uniform with large aggregates (~20 micron) while no visible aggregation is seen in the PVA film at the same CNC concentration. This indicates that the modified CNC incorporates uniformly in the hydrophilic PVA films. The CNC has an average length of 95 nm and an average diameter of 4.1 nm (from chapter 2), which gives a large surface area. This suggests that the covalent attachment of RBITC at low concentrations (~ 1 dye/CNC) does not modify the hydrophilicity of the CNC. In the 0.00 wt. % film, some small fluorescence particles were observed and are probably due to either impurities or dust.

The relationship between the fluorescence intensity and CNC concentration is shown in Figure 4-5. Each point in this plot indicates an average intensity value and a variance obtained from analysis of ten fluorescence images by ImageJ. The ten images are from random areas of the same sample. From Figure 4-3, it is observed that there is uneven illumination in each image; this is similar for all images and was not corrected prior to intensity analysis. The relationship between concentration and florescence intensity was fitted by a linear function with R^2=0.9726.

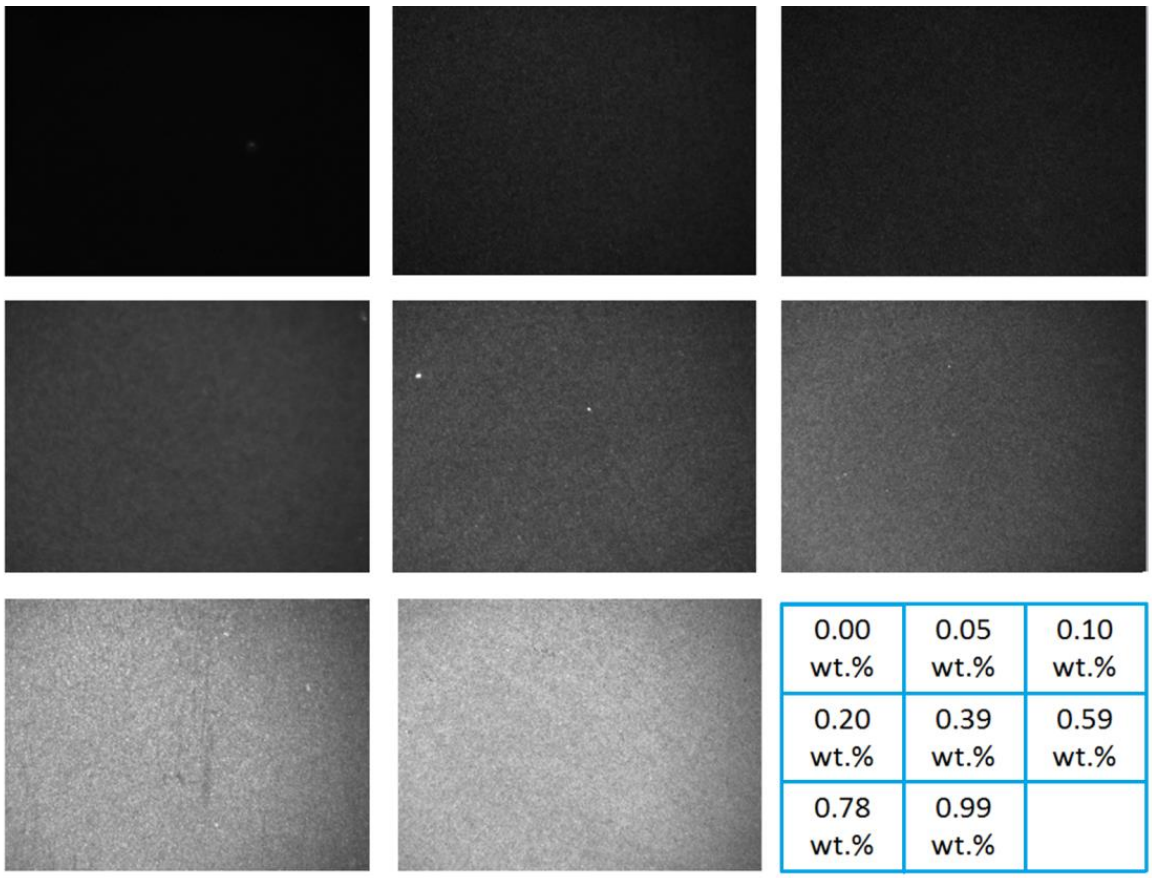

Figure 4-3: Fluorescence characterization of PVA-CNC film set 1. The 100 x fluorescence images are all on the same gray level (intensity) scale. The images show an 87.7 × 66 µm^2 area.

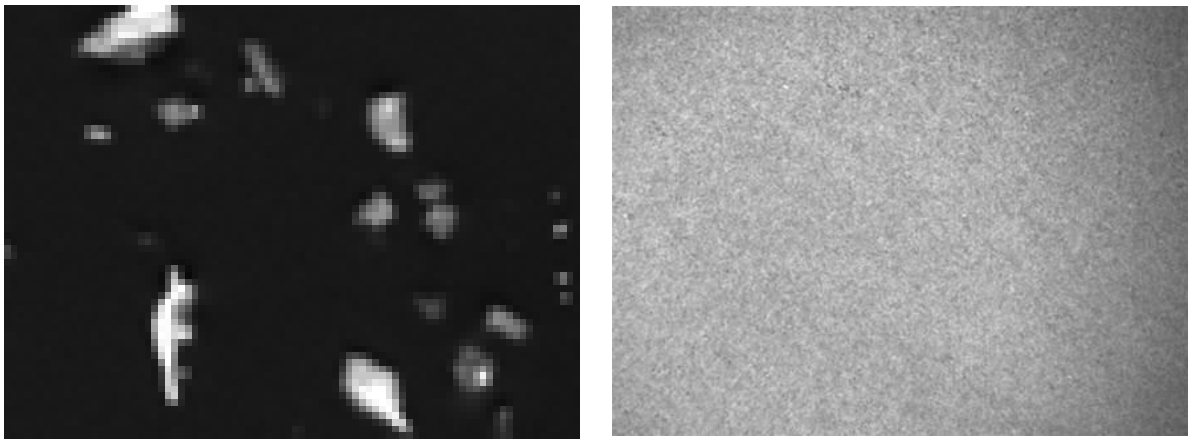

Figure 4-4: 1 wt. % films for both nitrobenzene modified CNC PS (left) and CNC-RBITC-3 PVA (right) are shown on the same scale. The image size is 87.7 × 66 µm^2.

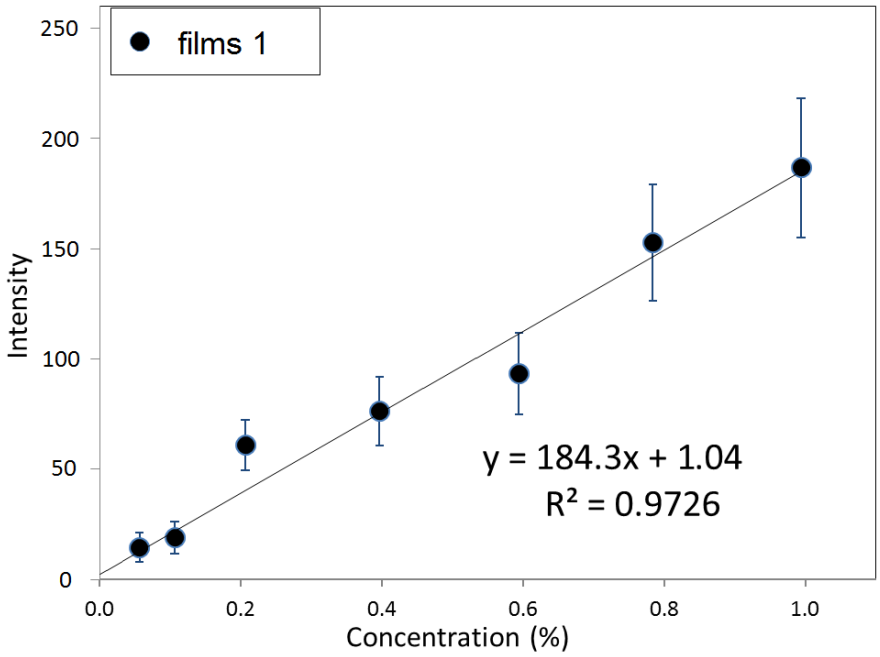

Figure 4-5: The fluorescence image intensity vs dye labeled CNC concentration for film set 1. The linear fitting formulas are shown in the graph.

Next films prepared with a wider range of CNC concentrations and two different spin coating speeds were examined. The images for film set 2 are shown in Figure 4-6 (spin coated at 2000 rpm) and Figure 4-7 (spin coated at 4000 rpm) on the same gray level. Visual inspection of the images does not show a difference in distribution between the two spin coating speeds for concentrations from 0.00 to 1.89 wt. %. When the CNC concentration is higher than 3.74 wt. %, some aggregates appear and the 2000 rpm films are more heterogeneous than the 4000 rpm films. The 5.50 wt. % sample prepared at 4000 rpm had the least uniform distribution in this sample set. This may be due to damage during shipping (this sample slid out of the protective sleeve during transport).

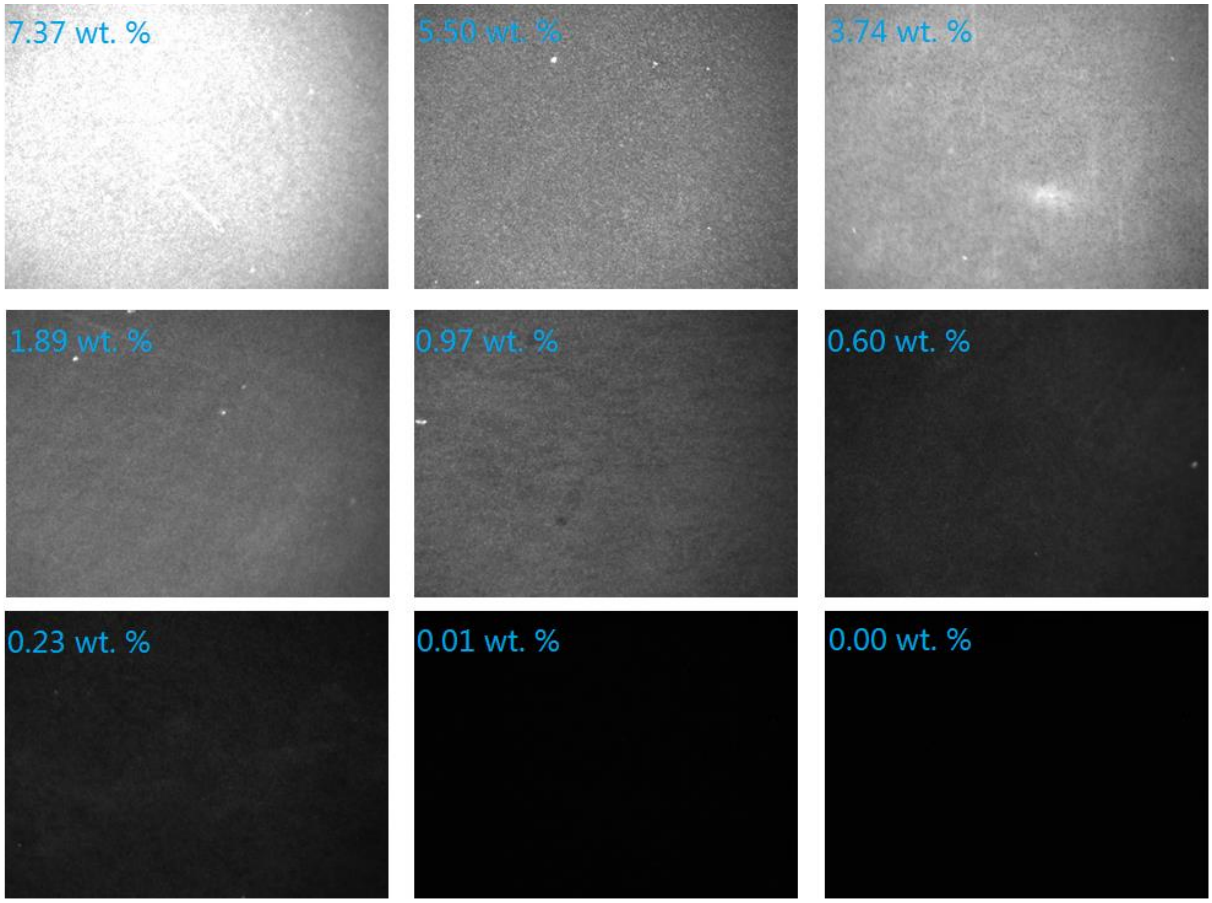

Figure 4-6: Fluorescence characterization of PVA/CNC film set 2 prepared with 2000 rpm spin rate. The 100 x fluorescence images are all on the same gray level (intensity) scale. The images show an 87.7 × 66 µm^2 area.

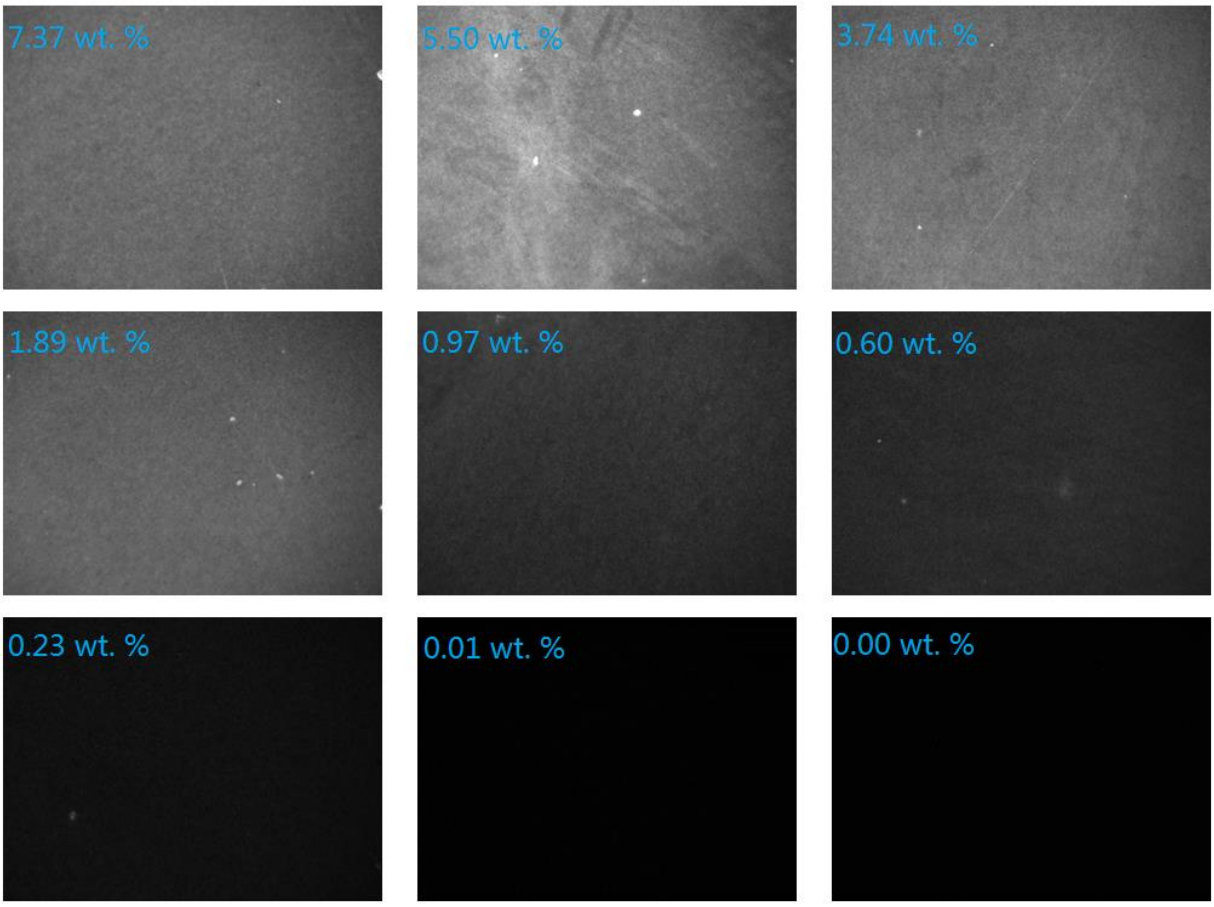

Figure 4-7: Fluorescence characterization of PVA/CNC film set 2 prepared with 4000 rpm spin rate. The 100 x fluorescence images are all on the same gray level (intensity) scale. The images show an 87.7 × 66 µm² area.

Figure 4-8 shows images for films set 2 with the intensity scale adjusted to a different value for each concentration; the same intensity scale is used for both spin rates at each CNC concentration. From the Figure, we can see that the distribution of CNC at each concentration is similar for the two spin rates and the samples are reasonably uniform and featureless. A few bright spots appear in some images and may be due to small aggregates of CNC or contaminants that may occur in the initial CNC suspension. The images at high concentrations of CNC are comparable to the ones at low concentration. Patterns that align in one direction are observed in

some pictures, such as the two pictures of 0.97 wt. %. This may occur by alignment of CNC in a specific direction during spin coating.

	Film set 2 (2000 rpm)	Film set 2 (4000 rpm)
7.37 wt. %	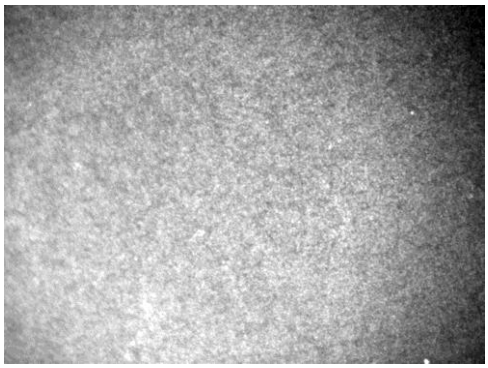	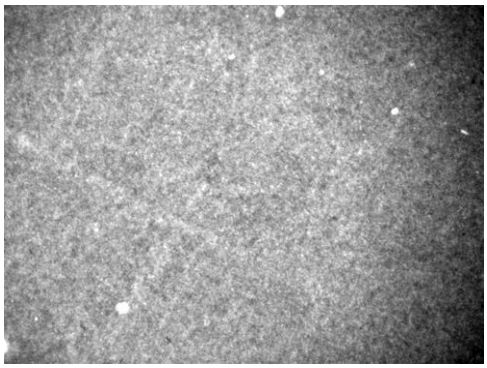
5.50 wt. %	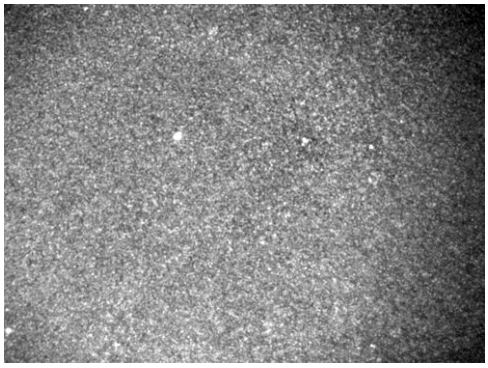	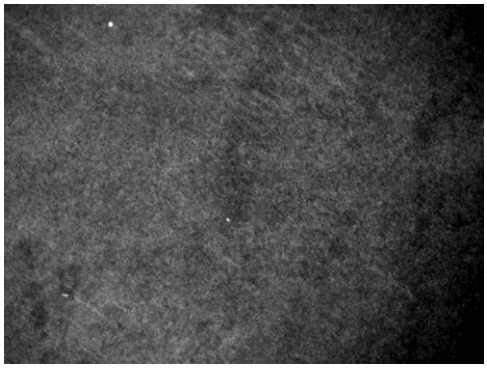
3.74 wt. %	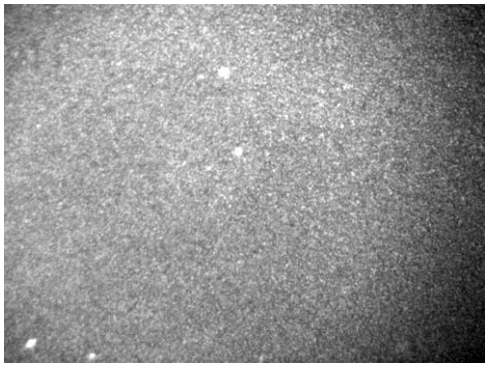	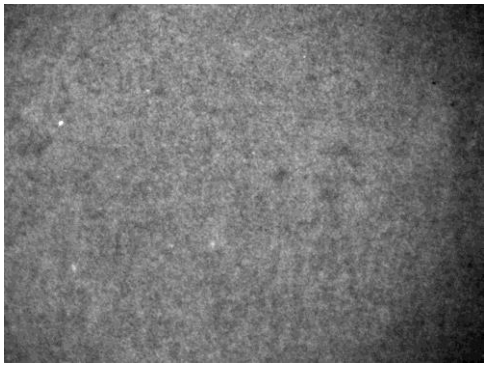

1.89 wt. %

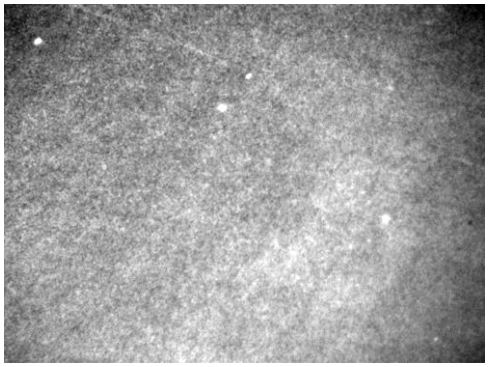

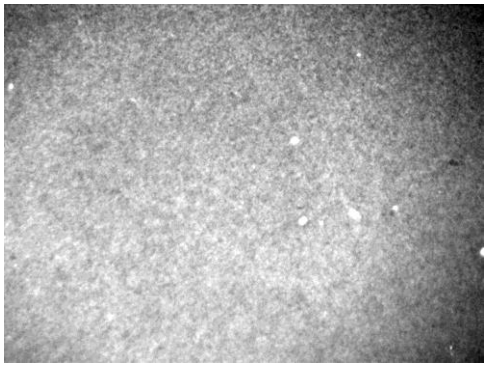

0.97 wt. %

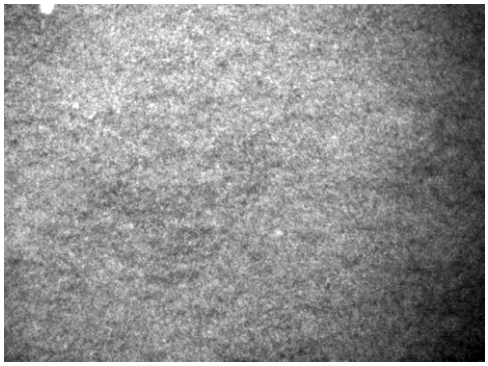

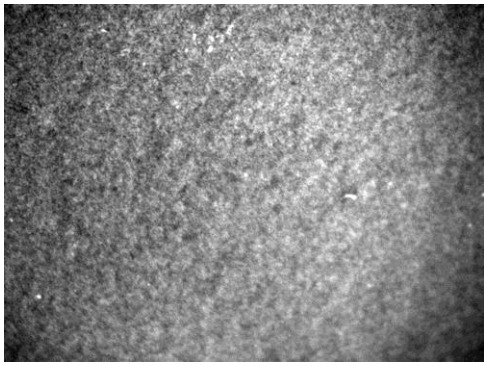

0.60 wt. %

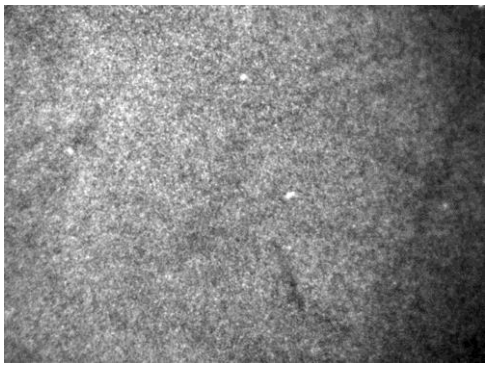

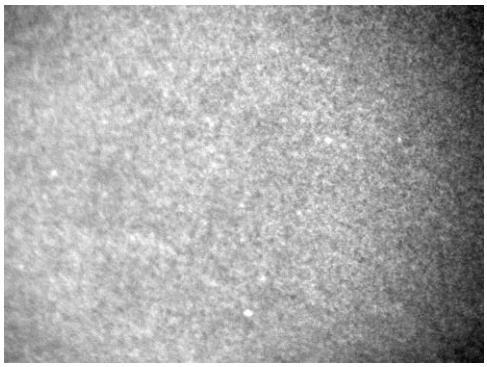

0.23 wt. %

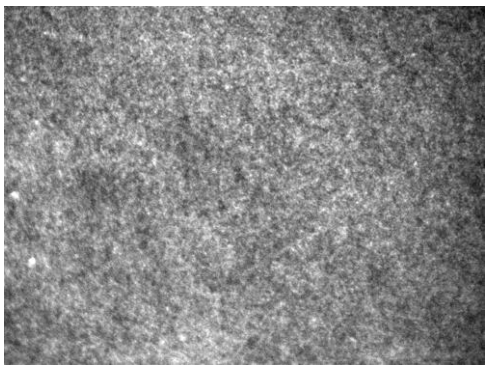

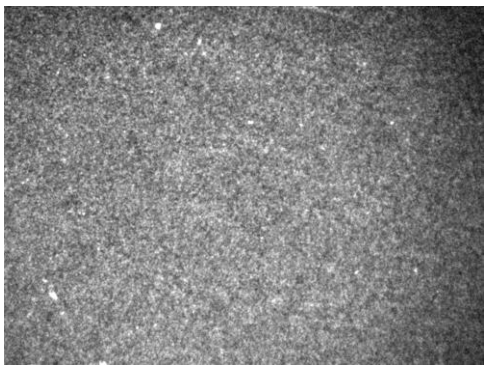

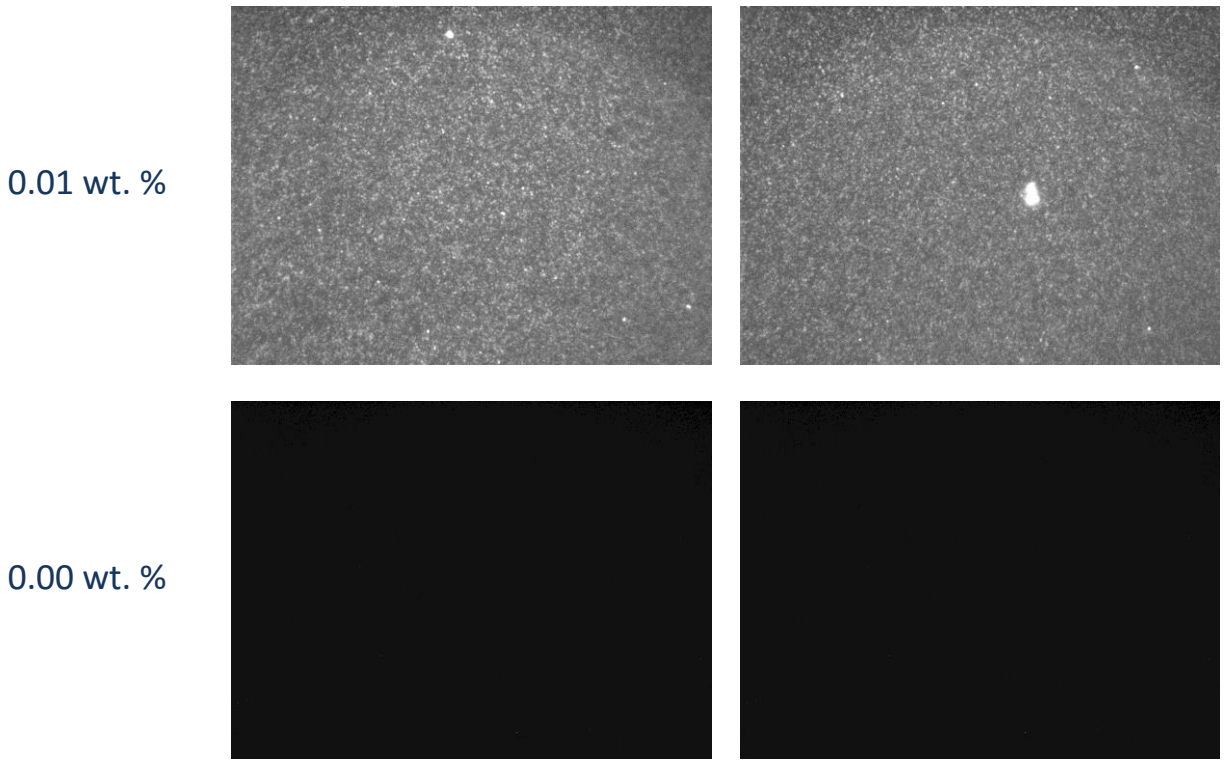

Figure 4-8: Comparisons of images for film set 2 at two spin rates. For each concentration, the two images are displayed on the same gray level. The images show an 87.7 × 66 μm² area.

The intensity vs. concentration relationship for film set 2 is plotted in Figure 4-9, and the data are fitted to an exponential curve. In this Figure, the film fluorescence intensity is still linear at low concentration, which is comparable to the results for film set 1. The difference in slope for the low concentration range may be due to the thickness of the films, which will be discussed in Section 4.3.3. At higher concentrations, the slope decreases and the curve levels off to a constant value. The most likely explanation for this decrease is self-quenching at high CNC concentration. The fits for these two groups have similar t value and similar A_0/A ratio, which means they have similar shape, but have different total amplitude (A_0).

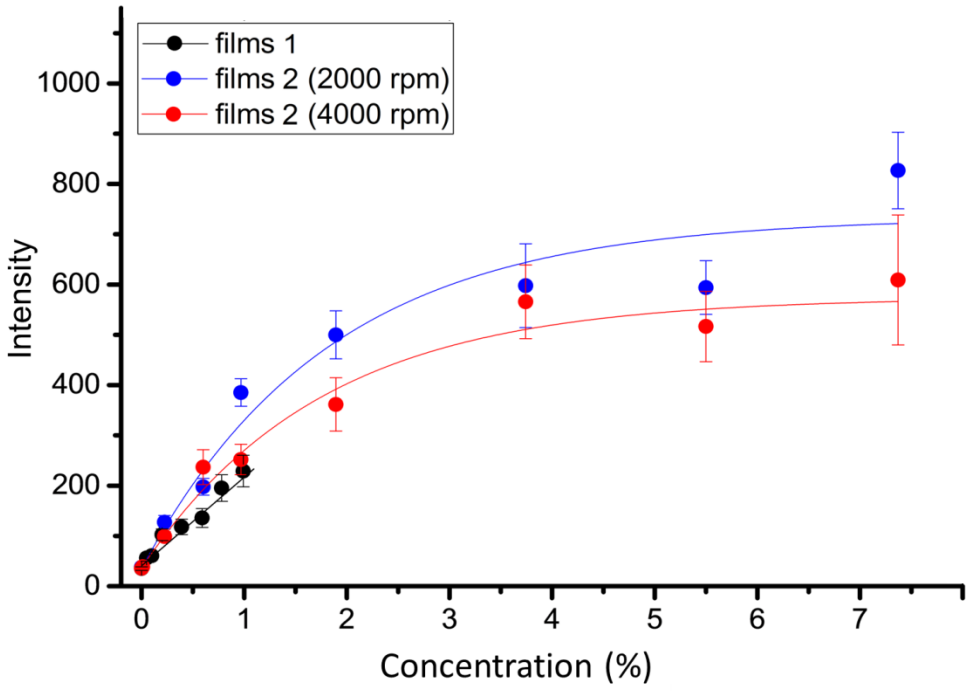

$$y = A*\exp(-x/t) + A_0$$

	A_0	A	A_0/A	t	R^2
Films 2 (2000 rpm)	687	-623	-1.10	1.82	0.9125
Films 2 (4000 rpm)	547	-505	-1.08	1.75	0.9564

Figure 4-9: Intensity vs. concentration plots for PVA-CNC films; Film set 2 was spin coated at 2000 rpm or 4000 rpm. The curve fitting formulas are shown under the graph.

Fluorescence images for the drop cast films (film set 3) are shown in Figure 4-10 with all images displayed using the same gray scale. In order to reduce aggregation in the drop cast film, the suspensions of dye labeled CNC and polymer were sonicated before producing the films. Since there is a wide range of intensities for this data set, it is difficult to draw any conclusions from visual inspection of images on a single intensity scale. The gray level adjusted images in Figure 4-11 provide a more useful means of assessing the CNC distribution. Visual inspection suggests

that the drop cast film is more heterogeneous than the spin coated film (comparing similar concentrations for film sets 1 and 2).

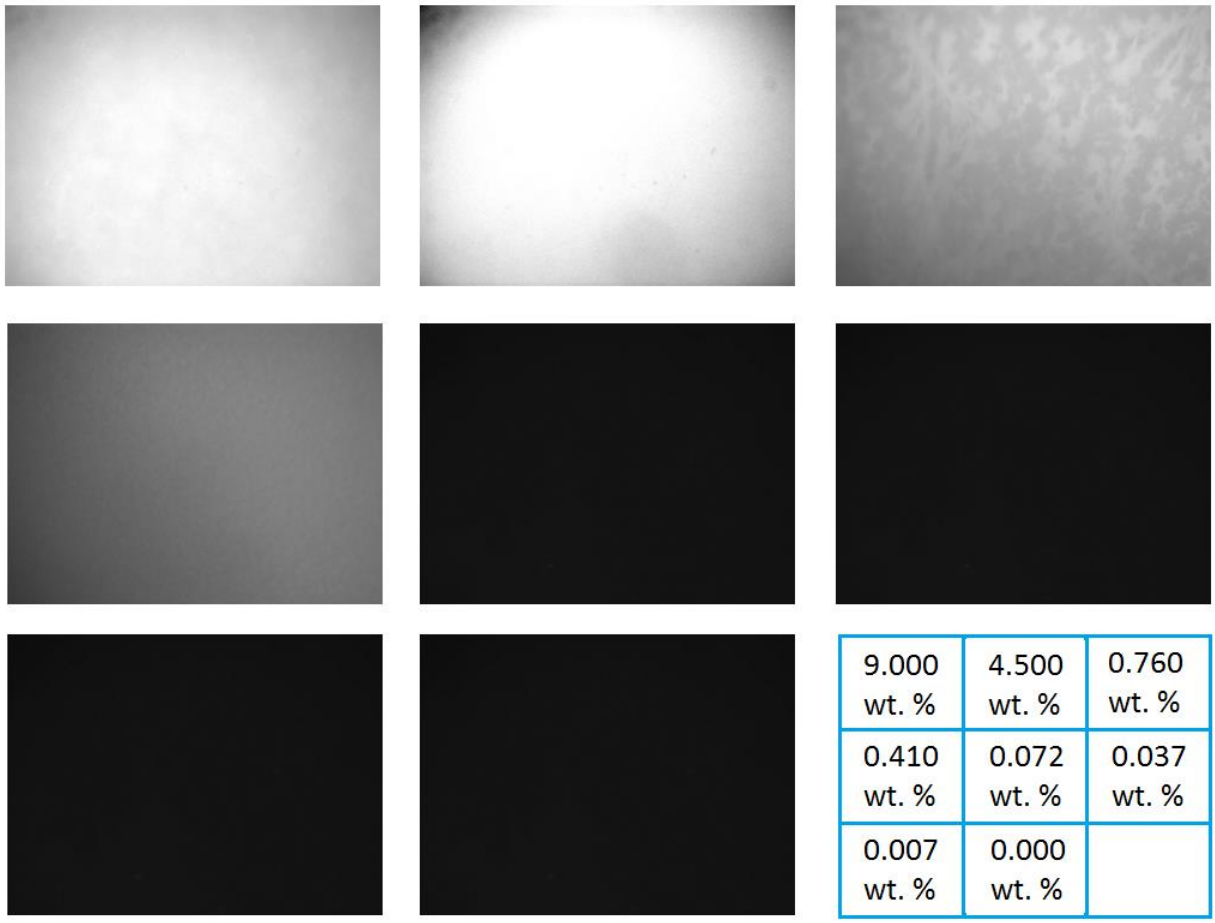

Figure 4-10: Fluorescence characterization of PVA-CNC films set 3 (drop cast). The 100 x fluorescence images are all on the same gray level (intensity) scale. The images show an 87.7 × 66 μm² area.

The images in Figure 4-11 indicate that the films become more heterogeneous with increasing CNC concentration up to 0.76% and then become more homogeneous again at higher concentrations (4.5 and 9 wt. %). This is particularly clear in the smaller scale images shown at the bottom of Figure 4-11. From the magnified images, patterns are dot-like at the low concentration of 0.072 wt. %; patterns are irregular and present the structure of porous-sponge at

the concentration of 0.41 wt. %; patterns show the shape of leaves vein at the concentration of 0.76 wt. % and no patterns are seen when the concentration reaches 4.5 wt. % and 9.0 wt. %.

In addition, there are two points that should be considered. One is that although the drop cast films show unevenly distributed CNC patterns, they do not have the few larger bright aggregates that are observed in film set 2. This may indicate that sonication of the sample removed large aggregates in the initial suspension used to make the films. The other point is that although no pattern is observed for the high concentration drop cast films. This may be due to the thicker film and higher CNC density. With the objective used, fluorescence is detected from an approximately 250 nm layer of the film so local heterogeneity may be averaged out for the higher concentration films.

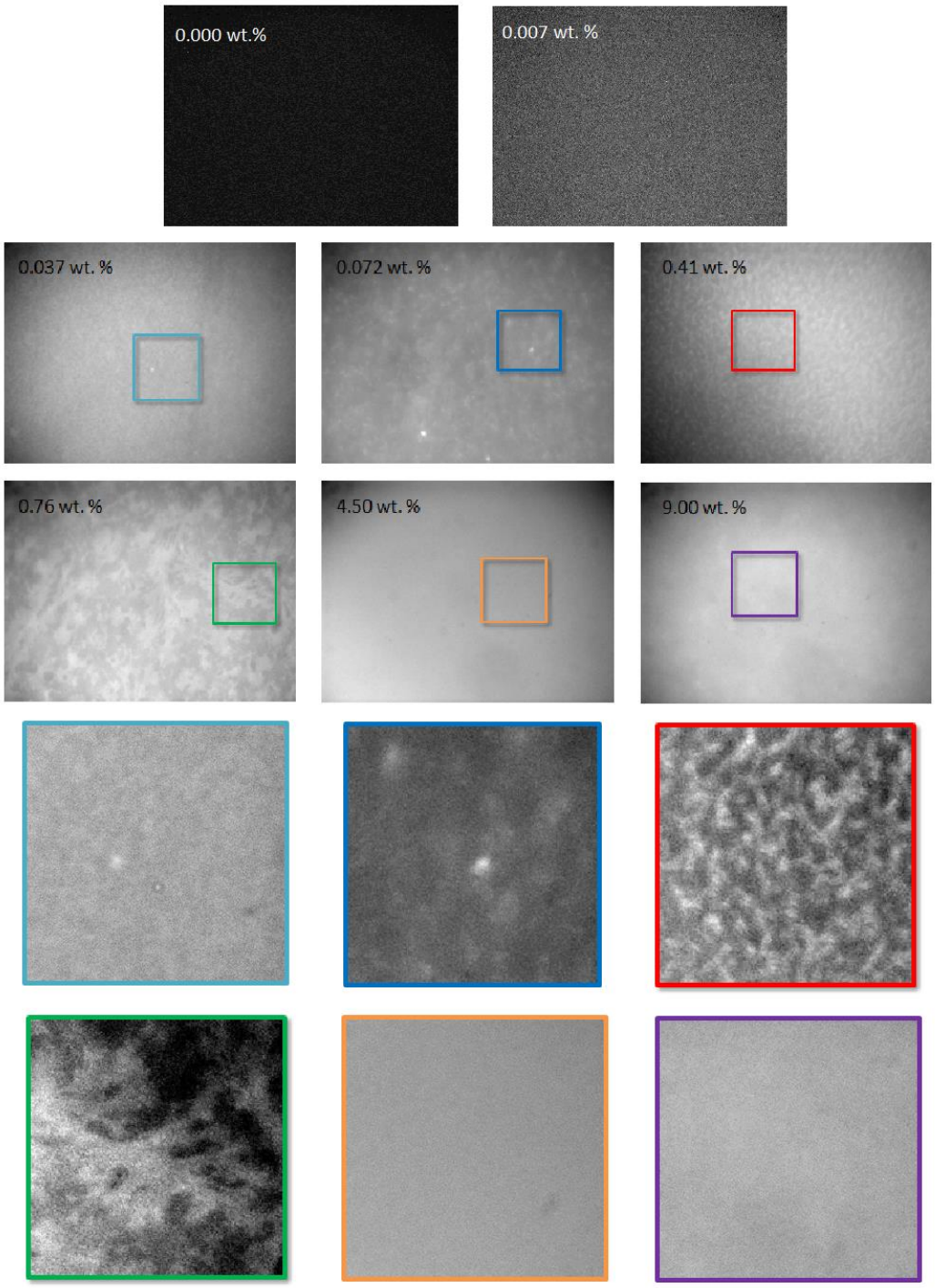

Figure 4-11: The gray value adjusted images of drop cast films (film set 3). The images in colored frames at the bottom are the cropped 20 ×20 μm² images from the same color box in the larger scale images.

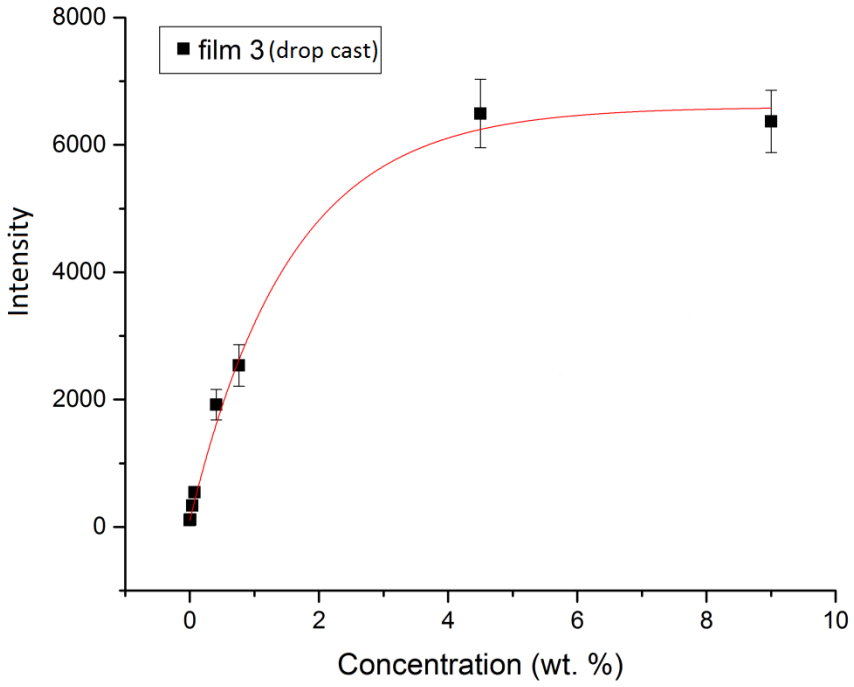

$$y = A*\exp(-x/t) + A_0$$

	A_0	A	A_0/A	t	R^2
Films 3 (drop cast)	6496	-6495	-1.02	1.55	0.9028

Figure 4-12: Intensity vs. concentration plots for PVA-CNC film set 3 prepared by the drop cast method and the single exponential fitting curve.

The intensity vs. concentration relationship for film set 3 is plotted in Figure 4-12, and the data are fitted to an exponential curve as for film set 2. In this Figure, the fitting curve has a similar shape as for the curves in film set 2, with a similar A_0/A ratio and t value. Thus, all the films show similar intensity vs concentration dependence.

Since there are clearly differences in the homogeneity of the various CNC films, we tested whether the differences could be quantified by examining the ratio of the standard deviation to the total image intensity. The dependence of this parameter on CNC concentration in the polymer film is shown in Figure 4-13. In this experiment, the 0.00 wt. % film image (as back ground) has been subtracted from all the images before measurement.

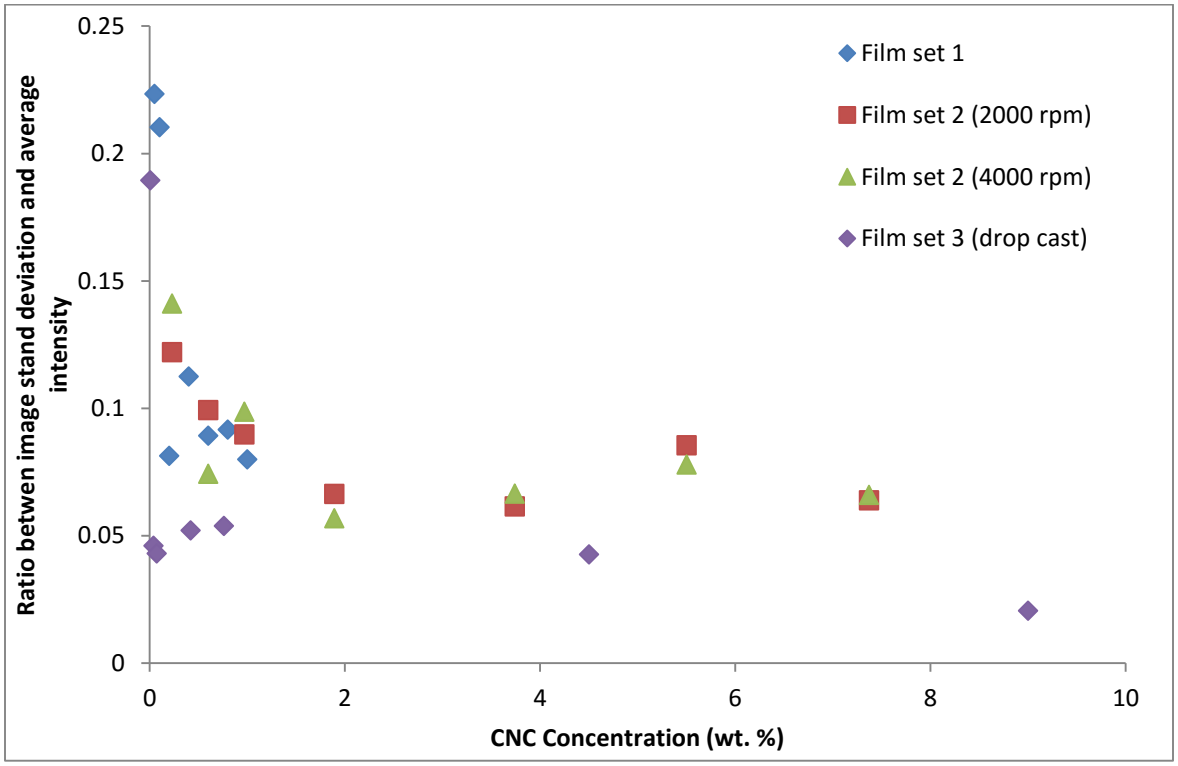

Figure 4-13: Ratio between intensity standard deviation and average intensity of four sets of PVA-CNC films.

Unfortunately, the graph of the standard deviation/average intensity ratio does not show the same trend which is observed by visual inspection of the images. For example, comparing the drop cast film (film set 3) and the spin coated film (film set 1, 2), a clear pattern appears in film set 3 0.76 wt. % (Figure 4-11) and the sample for film set 2 0.6 wt. % is more uniform (Figure 4-8). However, the ratio for film set 3 0.76 wt. % is much lower than that for film set 2 0.6 wt. %. A

possible explanation is that measuring the pixel to pixel variation does not capture the image heterogeneity, as shown in the schematic images in Figure 4-14. The distribution at the right is different from the one at the left, but both have the same average intensity and standard deviation.

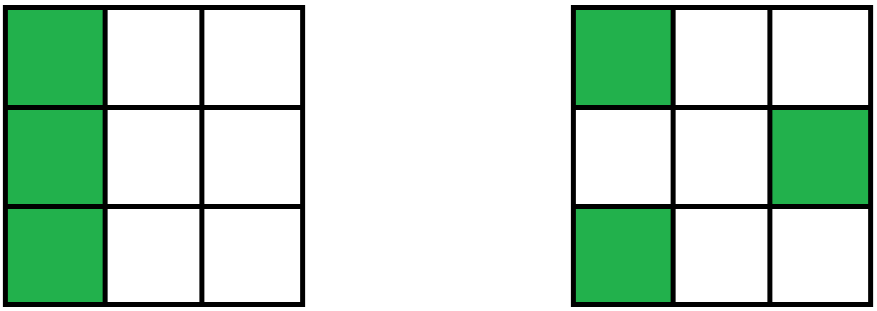

Figure 4-14: Schematic diagram of distribution, the green box is the dye labeled CNC and the white box is the polymer background. The distribution at right is different than at left, but both have the same average intensity and standard deviation.

Furthermore, the ratio at very low concentrations is quite high, which may be caused by the background subtraction. The background image is very uniform (almost no signal) and the intensity for the low concentration samples is low and similar to background. This means that subtraction of the two gives a large error. Future work should focus on developing a quantitative method for assessing the distribution of CNCs in composite films.

4.3.3 Thickness of films

The thickness of the film affects the florescence intensity. The thicker films will have more CNC and therefore give higher fluorescence intensity. Because the PVA film set 1 and 2 (spin coated) are too thin to pull off the slide, AFM was used to measure their thickness. A representative

AFM image is shown in Figure 4-15 left, the dark stripe is the scratch made with a sharp tweezer. A cross section is shown in Figure 4-15 right, which shows the surface of the film and the substrate. The peak at the edge of this cross section is due to the accumulated polymer that was removed by scratching.

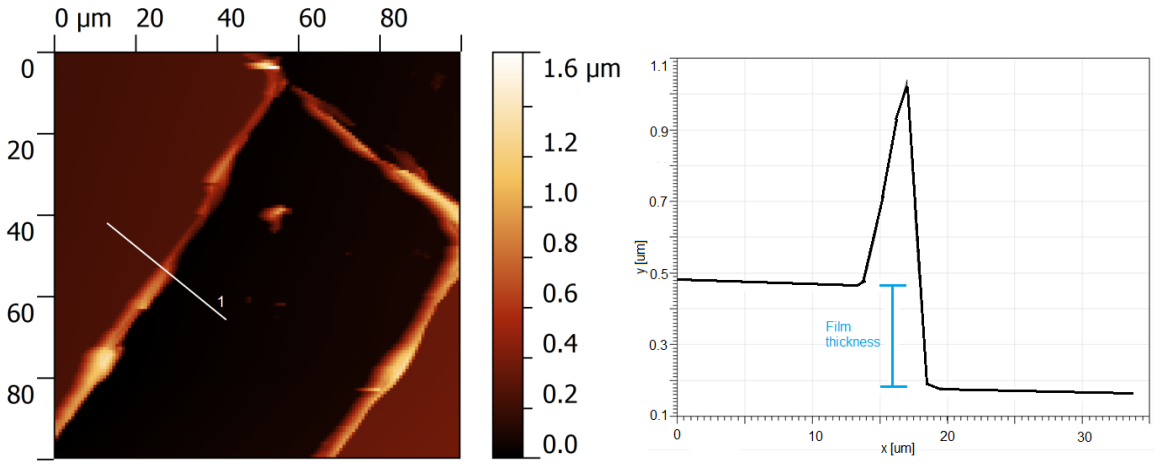

Figure 4-15: AFM image of a scratch in the film (left) and the cross section for line 1 (right). The thickness measurement is indicated on the cross section.

The thickness measurements are shown in Table 4-5. One sample was selected from each film set for AFM measurement of thickness, since the data from chapter 4.2.1 show that the CNC concentration does not affect the thickness for samples prepared with the same spin rate. For each sample, 10 images were measured at both the center and edge of the film by AFM. Then, the average and standard deviation have been calculated. For drop cast films, screw micrometer measurements were used to measure the films thickness with five locations measured for each film. When the film is removed from the slide, parts may have slight changes in shape, which may influence the thickness measurement. However, the thickness of drop cast films is 20-30 times higher than the spin coated films, which makes this error insignificant. For the spin coated films, the thickness of different sample sets prepared using the same spin rate was constant and

the thickness can be increased by decreasing the spin rate. The drop cast films have the highest thickness and roughest surface. Both methods produce films with edges that are thicker than the center.

Table 4-5: Thickness of CNC/PVA films.

Sample	Film set 1 (4000 rpm)	Film set 2 (4000 rpm)	Film set 2 (2000 rpm)	Film set 3 (drop cast)*
Center thickness (nm)	80±3	96±1	182±21	$2.98\pm0.40 \times 10^4$
Edge thickness (nm)	91±5	104±26	206±11	$3.22\pm0.13 \times 10^4$

(*) film set 3 is measured by screw micrometer after removing film from cover slide.

The thickness data can partly explain the difference in slope at low concentration between the sample sets and also the amplitude difference at high concentrations. The depth of field of the lens is approximately 250 nm[17], which is larger than the thickness for all the spin coated films and much smaller than the thickness of the drop cast films. For the thick films, fluorescence intensity was only measured from a thin section but the entire film was measured for the spin coated films. Therefore, there is no expectation that the measured intensity will show a linear relationship with film thickness for all 3 film sets. Although the film thickness can explain the increased intensity for the 4000 rpm film compared to the 2000 rpm film, the difference is much less than expected for twice the thickness. Thus, a more complex self-quenching may affect the total intensity.

4.3.4 CNC average distance calculation

In order to test whether the distance between individual CNCs is within a range that is consistent with self-quenching, the average CNC distance was estimated by the following model (Figure 4-16). The CNC particle is assumed to be a cylinder which is placed in the center of a polymer cuboid. The distances (d) between the CNC cylinder and each surface of the cuboid are equivalent. That also means the height and width of the polymer cuboid are equivalent (H'). The average distance between two CNC particles is 2d. The model assumes that CNC particles do not aggregate.

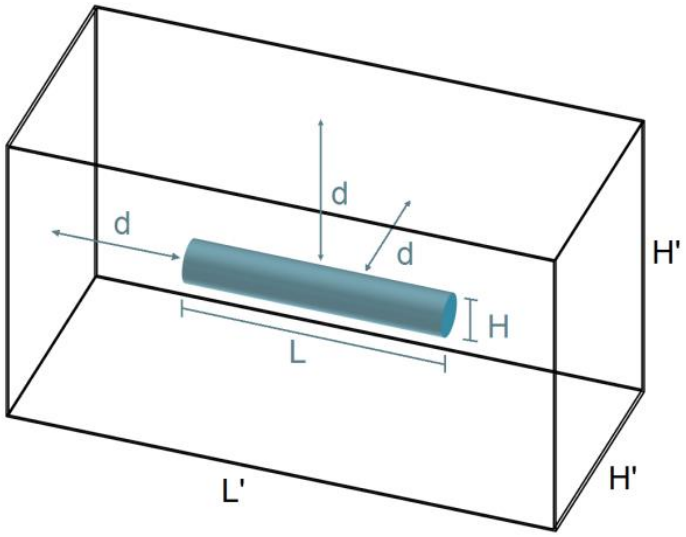

Figure 4-16: Schematic diagram of the model for estimating the average CNC distance. The blue cylinder is CNC and the cuboid is the polymer matrix. The CNC particle is in the center of the polymer and has the same distance (d) to each surface of the cuboid.

V_{total} which is the volume of both CNC and polymer can be written as:

$$V_{total} = \mathrm{L}'(H')^2 \qquad \text{(Equation 4-1)}$$

$$L' = 2d + L$$

$$H' = 2d + H$$

H and L are the average height (4.1 nm) and length (89.5 nm) of CNC-Maine which was measured in Chapter 2 by AFM. V_2 which is the volume of a single CNC can be written as:

$$V_2 = \pi(\frac{H}{2})^2 L \quad \text{(Equation 4-2)}$$

Then, the volume of polymer, V_1, can be written as:

$$V_1 = V_{total} - V_2 \quad \text{(Equation 4-3)}$$

Because the concentration is based on the weight, the concentration (c) can be written as:

$$c = \frac{1}{\frac{V_1\rho_1}{V_2\rho_2}+1} \quad \text{(Equation 4-4)}$$

where ρ_1 is the density of PVA and ρ_2 is the density of CNC. Putting Equation 4-1, Equation 4-2, and Equation 4-3 into Equation 4-4, a concentration formula which depends on particle distance can be written as:

$$c = \frac{\pi L(\frac{H}{2})^2\rho_2}{\pi L(\frac{H}{2})^2\rho_2+[(L+2d)(H+2d)^2-\pi L\left(\frac{H}{2}\right)^2]\rho_1} \quad \text{(Equation 4-5)}$$

Using a PVA density of 1.19g/cm^3 and a CNC density of 1.6 g/ cm^3, the plot of distance between particles, 2d, as a function of concentration c can be obtained as shown in Figure 4-17 (dotted line with right y axis). Because of the assumptions of the model, the average particle distance (2d) does not display the real particle distance and the actual situation may be more complex due to CNC aggregation. However, it does provide some information on the probability of interaction between CNCs.

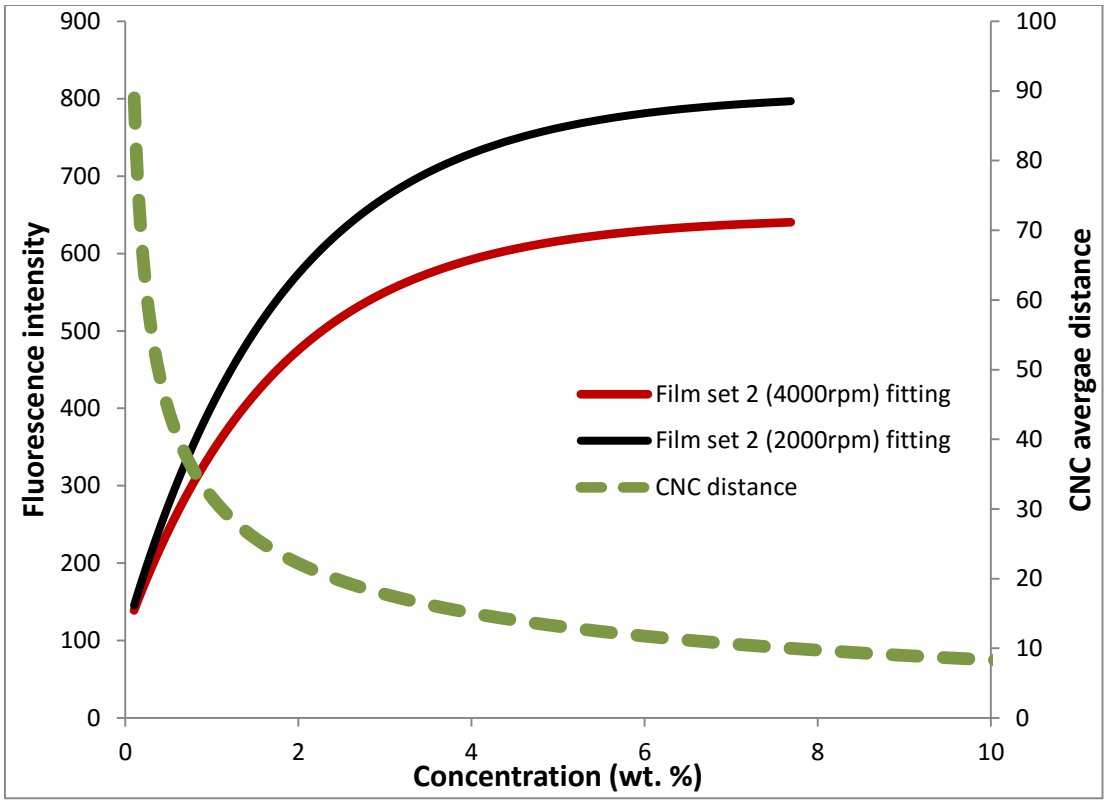

Figure 4-17: The calculated distance between two CNC particles vs. concentration plot (dotted green line) is shown with right y axis. The fluorescence intensity curves of film set 2 4000 rpm (solid red line) and 2000 rpm (solid black line) are shown with the left y axis.

In Figure 4-17, the fluorescence intensity vs concentration fitting curves of two film sets are plotted on the left y axis. As described in chapter 4.3.2, the fitting curve is a single exponential which is linear at low concentration and tends to a constant value at high concentration. This is because the self-quenching depends on the average distance between particles. When this distance is large, the interaction between labeled CNCs is less and the intensity increases linearly with concentration, as for film set 1. When the distance between particles is small, the interaction between dye labeled CNCs such as quenching, dimer formation, and self-absorption is more likely to occur. Thus, the total fluorescence intensity of CNC increases more slowly and tends to a constant value at high concentration. Thus, self-quenching increases with decreasing distance

between particles, limiting the region where there is a linear relationship between concentration and fluorescence intensity.

Self-quenching of florescence is a well-known phenomenon[18], and depends on the structure of the dye[19]. Alexa dyes have been recommended by Kell et al[19], based on their study of silica nanoparticles loaded with dyes which showed that Alexa dyes have less self-quenching than rhodamine B. This suggests that use of a dye that does not form dimers readily and that is less likely to undergo self-quenching would be more useful for labelling CNC.

4.4 Conclusion

In this chapter, composite films of nitrobenzene-modified CNC and PS have been tested for comparison with films containing dye-labeled CNCs. Although the films look transparent by eye, examination by bright field microscopy using a 20x objective showed that the distribution of modified CNC was very heterogeneous. This shows CNC after nitrobenzene modification is less hydrophilic than expected. In future, it is interesting to use the nitrobenzene-modified CNC and other hydrophobic polymer like epoxy resin, polyethylene (PE) and polylactic acid (PLA) to produce polymer composites, which are expected have a more uniform dispersion of CNC. Also, this experiment showed that, owing to CNC's autofluorescence or Raman scattering, use of a Cy3 filter with a low magnification lens can provide better contrast and distribution details than the light field microscope. This approach may be useful if dye-labeled CNCs are not available.

In this chapter, dye-labeled CNC has been incorporated successfully in a hydrophilic polymer (PVA) and epifluorescence microscopy was used to study the CNC distribution. The CNC distribution in PVA film is very uniform and much better than in PS films. However, studies of

the fluorescence intensity as a function of CNC concentration show that self-quenching starts to occur at ~2 wt. %. Such phenomenon is a limitation to studies of high concentrations of dye-labeled CNCs in composite materials. In the future, it would be feasible to use RBITC-labeled CNC to study high CNC concentration composite materials if a lower concentration of dye on the surface of CNC was used. Also, using mixtures of unmodified CNC and dye labeled CNC may be a useful approach to lower the self-quenching. Of course, another approach is to use other fluorophores to label the CNC. Alexa dyes, which have weaker self-quenching in other nanoparticles[19], should be more compatible with high CNC concentration samples.

The experiments so far have only used epifluorescence microscopy and did not test the CNC distribution at different depths in the films. In the future, the confocal microscope and total internal reflection fluorescence microscope may be used to sample different film depths. The super-resolution fluorescence microscope could be used to provide higher resolution.

Although RBITC labeled CNC is uniformly distributed in PVA, PVA, as a water-soluble polymer, doesn't play a major role in industrial production. For future research, choosing a combination of hydrophobic group modified CNC and hydrophobic polymers and then labeling the modified CNC will be a better test of fluorescence microscopy as a method for studying CNC distribution.

4.5 References

1. Park, W. I.; Kang, M.; Kim, H. S.; Jin, H. J. In *Electrospinning of poly (ethylene oxide) with bacterial cellulose whiskers*, Macromolecular symposia, Wiley Online Library: 2007; pp 289-294.
2. Medeiros, E. S.; Mattoso, L. H.; Ito, E. N.; Gregorski, K. S.; Robertson, G. H.; Offeman, R. D.; Wood, D. F.; Orts, W. J.; Imam, S. H., Electrospun nanofibers of poly (vinyl alcohol) reinforced with cellulose nanofibrils. *Journal of Biobased Materials and Bioenergy* **2008,** *2* (3), 231-242.
3. (a) Habibi, Y.; Goffin, A.-L.; Schiltz, N.; Duquesne, E.; Dubois, P.; Dufresne, A., Bionanocomposites based on poly (ε-caprolactone)-grafted cellulose nanocrystals by ring-opening polymerization. *Journal of Materials Chemistry* **2008,** *18* (41), 5002-5010; (b) Habibi, Y.; Dufresne, A., Highly filled bionanocomposites from functionalized polysaccharide nanocrystals. *Biomacromolecules* **2008,** *9* (7), 1974-1980.
4. Rojas, O. J.; Montero, G. A.; Habibi, Y., Electrospun nanocomposites from polystyrene loaded with cellulose nanowhiskers. *Journal of Applied Polymer Science* **2009,** *113* (2), 927-935.
5. De Rodriguez, N. L. G.; Thielemans, W.; Dufresne, A., Sisal cellulose whiskers reinforced polyvinyl acetate nanocomposites. *Cellulose* **2006,** *13* (3), 261-270.
6. Chauve, G.; Heux, L.; Arouini, R.; Mazeau, K., Cellulose poly (ethylene-co-vinyl acetate) nanocomposites studied by molecular modeling and mechanical spectroscopy. *Biomacromolecules* **2005,** *6* (4), 2025-2031.
7. Tang, L.; Weder, C., Cellulose whisker/epoxy resin nanocomposites. *ACS applied materials & interfaces* **2010,** *2* (4), 1073-1080.
8. Kamal, M. R.; Khoshkava, V., Effect of cellulose nanocrystals (CNC) on rheological and mechanical properties and crystallization behavior of PLA/CNC nanocomposites. *Carbohydrate polymers* **2015,** *123*, 105-114.
9. de Menezes, A. J.; Siqueira, G.; Curvelo, A. A.; Dufresne, A., Extrusion and characterization of functionalized cellulose whiskers reinforced polyethylene nanocomposites. *Polymer* **2009,** *50* (19), 4552-4563.
10. Habibi, Y.; Lucia, L. A.; Rojas, O. J., Cellulose nanocrystals: chemistry, self-assembly, and applications. *Chemical reviews* **2010,** *110* (6), 3479-3500.
11. (a) Leung, A. C.; Lam, E.; Chong, J.; Hrapovic, S.; Luong, J. H., Reinforced plastics and aerogels by nanocrystalline cellulose. *Journal of nanoparticle research* **2013,** *15* (5), 1-24; (b) Lukach, A.; Thérien-Aubin, H.; Querejeta-Fernández, A.; Pitch, N.; Chauve, G.; Méthot, M.; Bouchard, J.; Kumacheva, E., Coassembly of Gold Nanoparticles and Cellulose Nanocrystals in Composite Films. *Langmuir* **2015,** *31* (18), 5033-5041.
12. (a) Dong, S.; Roman, M., Fluorescently labeled cellulose nanocrystals for bioimaging applications. *Journal of the American Chemical Society* **2007,** *129* (45), 13810-13811; (b) Grate, J. W.; Mo, K.-F.; Shin, Y.; Vasdekis, A.; Warner, M. G.; Kelly, R. T.; Orr, G.; Hu, D.; Dehoff, K. J.; Brockman, F. J., Alexa Fluor-Labeled Fluorescent Cellulose Nanocrystals for Bioimaging Solid Cellulose in Spatially Structured Microenvironments. *Bioconjugate chemistry* **2015,** *26* (3), 593-601.
13. Abitbol, T.; Palermo, A.; Moran-Mirabal, J. M.; Cranston, E. D., Fluorescent labeling and characterization of cellulose nanocrystals with varying charge contents. *Biomacromolecules* **2013,** *14* (9), 3278-3284.

14. Gilman, J. W.; Zammarano, M.; Maupin, P. H.; Sung, L.-P.; McCarthy, E.; Kim, Y. S.; Fox, D.; Berro, A. J.; Sacui, I. In *Use of Förster Resonance Energy Transfer (FRET) as a New Characterization Method for the Interface in Sustainable Nanocomposites*, Meeting Abstracts, The Electrochemical Society: 2012; pp 244-244.

15. Kalita, E.; Nath, B.; Agan, F.; More, V.; Deb, P., Isolation and characterization of crystalline, autofluorescent, cellulose nanocrystals from saw dust wastes. *Industrial Crops and Products* **2014**.

16. Sacui, I. A.; Nieuwendaal, R. C.; Burnett, D. J.; Stranick, S. J.; Jorfi, M.; Weder, C.; Foster, E. J.; Olsson, R. T.; Gilman, J. W., Comparison of the properties of cellulose nanocrystals and cellulose nanofibrils isolated from bacteria, tunicate, and wood processed using acid, enzymatic, mechanical, and oxidative methods. *ACS applied materials & interfaces* **2014,** *6* (9), 6127-6138.

17. Kenneth R. Spring, H. E. K., Michael W. Davidson Microscope Objectives Introduction. http://www.olympusmicro.com/primer/anatomy/objectives.html (accessed Aug. 6th).

18. Lakowicz, J. R., *Principles of fluorescence spectroscopy*. Springer Science & Business Media: 2013.

19. Kell, A. J.; Barnes, M. L.; Jakubek, Z. J.; Simard, B., Toward Brighter Hybrid Magnetic-Luminescent Nanoparticles: Luminosity Dependence on the Excited State Properties of Embedded Dyes. *The Journal of Physical Chemistry C* **2011,** *115* (38), 18412-18421.

Chapter 5

Closing Remarks and Future Directions

5.1 Closing remarks

This thesis describes the characterization of the particle size distribution of cellulose nanocrystals (CNC), the synthesis and characterization of fluorescent CNCs, and the development of a fluorescence microscopy method to probe the distribution of fluorescent CNCs in polymer composites. In developing the CNC size characterization method, we have addressed some of issues related to comparing data from AFM, TEM and DLS. We showed that RBITC is not the best for labeling CNC because it forms dimers and has strong self-quenching in polymer films. Several methods have been developed for characterizing the dye loading and their advantages and disadvantages are discussed. Furthermore, with the dye labeled CNC/PVA composite film, we used the dye labeled CNC to measure the distribution of CNC in the composites. To explain the self-quenching problem, a simplified CNC distance model has been constructed, which is a useful tool for any CNC composite study.

The never dried CNC and re-dispersed CNC size characterization is presented in chapter 2. A series of CNC samples was prepared by ultrasonication and examined by AFM, TEM and DLS. The K-S test has been used to assess whether differences between distributions are significant. The effects of ultrasonication were studied for the never dried CNC, because the percentage of aggregates can affect the DLS measurements. The re-dispersion of dry CNC was examined in detail, especially the extent of sonication needed. Plots of Z-average against sample sonication show a clear two exponential fit, unlike the curves for never-dried suspensions. Tests of the effect of sonication indicated that the Z-average for never-dried samples decreased rapidly and then reached a plateau at approximately 5000 J/g. Thus, in the future, any quantitative measurement of CNC by DLS should re-disperse the sample with 5000 J/g sonication energy to obtain a reproducible and easily repeatable sample. The particle size distribution from TEM and

AFM were compared after correction for sample-tip convolution effect for the AFM dat. This comparison gave similar result. Thus, in the future, this tip convolution effect correction should be used. Furthermore, the personal bias from analyzer was discussed in this chapter, which may cause errors in TEM or AFM data analysis. Because this error is based on the choice of individual CNC for analysis, the most effective method to reduce this error is to reduce the CNC aggregation. Since the aggregates may be formed in the suspension or when CNCs adsorb on the substrate, both sonication and spin coating should be tried in future experiments.

In chapter 3, two dyes have been covalently attached to the CNC surface successfully. Moreover, the photophysical parameters have been studied in detail using four different absorption and fluorescence methods, which has not typically been done for other dye-labeled CNCs. Although, fluorescence lifetimes and anisotropy showed clear changes that were consistent with covalent attachment of the dye to the surface, DTAF dye labeled CNC was not examined in further detail because its pH sensitivity would be problematic for applications for polymer composites.

RBITC has been one of the most popular dyes used for labeling CNCs. Three RBITC labeled CNC with different dye loadings have been prepared and examined by absorption and fluorescence methods. The scattering method has been used to characterize the concentration of the CNC suspension because it requires less sample. Fluorescence lifetimes and anisotropy measurements were consistent with covalent attachment of the dye to the CNC surface. Three approaches, including ensemble methods such as UV-Vis absorption and scattering measurements, fluorescence spectroscopy and single molecule methods such as TIRFM, AFM and correlated TIRFM/AFM measurements were used to determine the dye loading. All of these methods have their advantages and disadvantages. After characterization, the most suitable dye labeled CNC sample was selected for development of a fluorescence microscopy method to

characterize CNC distribution in CNC/polymer composites. The fluorescence intensity of RBITC labeled CNC decreases with increased dye loading which probably reflects quenching by dimers or oligomers. These results indicate that adding more RB will not lead to a better dye-labeled CNC

In chapter 4, the distribution of CNC polymer composites which are nitrobenzene modified CNC in PS film and RBITC labeled CNC in PVA film has been tested. The nitrobenzene modified CNC has shown aggregates by bright field microscopy. Furthermore, the Cy3 filter could be used to image even unlabeled CNC because of auto-fluorescence or Raman scattering. The RBITC labeled CNC is used to determine the CNC distribution in hydrophilic polymers (PVA). The CNC distribution in PVA film is very uniform and much better than in PS films. However, self-quenching of the dye labeled CNC which depends on the particle average distance occurs at relatively low CNC concentrations. A different dye which has less self-quenching could be used to reduce this problem. A simplified model of CNC distance model has been constructed, which is a useful tool for any CNC composite study. We also tried to quantify the CNC distribution in the composite film. However, the method which calculates the ratio between standard deviation and average intensity after subtraction of the background is not suitable for this purpose.

5.2 Future Directions

5.2.1 Future work with CNC size characterization

As discussed in chapter 2 one of our initial objectives was to characterize the relationship between size characterization and CNC dispersion. We assessed that the dispersion has a large effect in DLS measurements but not the AFM measurement, which is due to the presence of

aggregates which contribute to the DLS results, but are not analyzed by AFM. In future, the never dried CNC should be compared with the same sample after drying and re-dispersion, to test for effects of different drying methods. As shown in chapter 2, even with a sample size of 300 CNC, personal judgment bias still has a significant effect on the final result. In this study, we used only the incubation method to prepare samples for microscopy, which might generate large amount of aggregates. Since longer CNC are more likely to form aggregates, and aggregated CNC must be discarded when assessing the size of individual CNC, it is possible that the incubation method may not give a representative sample. Other methods, such as spin-coating, should also be tried for preparation of AFM and TEM samples. The spin-coating method thoroughly distributes the sample by centrifugation, so aggregation, as well as its impact on assessment of CNC size, can be reduced. However, the sample loss is also an issue with spin-coating.

DLS is currently the fastest and cheapest method for CNC size characterization, and would be beneficial in future studies of CNC for large-scale industrial applications. Therefore, it would be of great significance to establish a reproducible DLS measurement method that can relate the DLS result to the real CNC size distribution. Such work would require comparative experiments between DLS and AFM, TEM, to study the effect of surface charge, functional group, dispersed pH etc. on particle size distribution.

5.2.2 Future work with fluorescent CNC

The dye labeled CNC work I have presented in chapter 3 raises some questions regarding the dye loading efficiency. Because of the dimer, the absorption method is not as accurate as other studies have assumed. Due to the dimer problem, RBITC is not a satisfactory dye for quantitative fluorescence intensity measurements. Its only advantage is the low price, which facilitates large-

scale use. Other dyes, such as Alexa, would satisfactorily solve this problem. So in future, RBITC is not recommended for labeling CNC, and other dyes should be tried.

In this study, the CNC size used for the dye loading estimate was based on the size of unmodified CNC as described in Chapter 2. This can contribute errors, since some smaller CNC would be lost during dialysis and centrifugation. In future studies, characterization of the size of dye-labeled CNC would be necessary.

The AFM/TIRFM correlation has the potential to give more accurate dye loading of CNC. However, as a high-end single molecule detection experiment, the correlation demands high operator skill and an expensive instrument, and is limited by AFM tip aging. It is unlikely to be a common testing method for dye loading. In the future, AFM/TIRFM correlation might be used to give dye loading with a large number of corrected particles.

5.2.3 Future work with dye labeled CNC composites

In chapter 4, it was proved feasible to assess the distribution of CNC in composites using dye-labeled CNC. In addition, different distribution patterns of CNC in composite films prepared by different methods are also compared in this chapter. However, the major problem here is self-quenching of the dye based on distance between CNC particles. The self-quenching of different dyes is well known and RBITC is quite susceptible to self-quenching. So, in future studies, dyes that are more resistant to self-quenching would be used to label CNC and tested in composites. Furthermore, a method to quantify the CNC distribution should be developed.

In chapter 4, our results showed that dye-labeled CNCs are well distributed in hydrophilic polymer materials, suggesting that dye-labeling didn’t affect the characteristics of CNC. In the future, we shall try to label CNC modified with hydrophobic groups, to test the distribution of

such hydrophobic CNC in hydrophobic polymer materials. Even if such modified CNC did not disperse well, as for nitrobenzene CNC/PS composites, use of dye-labeled CNC would be of significance, since it would enhance contrast for imaging, and reveal the distribution of CNC outside of aggregates.